UNIVERSITY OF BIRMINGHAM

FIRST-PRINCIPLES ELECTRONIC STRUCTURE AND THERMODYNAMIC INVESTIGATION ON THE α AND β PHASES IN TI-O, TI-NB AND TI-NB-O SYSTEMS

by

NING ZHANG

A thesis submitted to the University of Birmingham for the degree of

DOCTOR OF PHILOSOPHY

Supervisor: Prof. Alessandro Mottura

School of Metallurgy and Materials

College of Engineering and Physical Sciences

University of Birmingham

July 2024

Abstract

As one of the most crucial metals of the 21^{st} century, titanium (Ti) is extensively used in the chemical industry, medical apparatus manufacturing, and aerospace engineering due to its high melting point, low density, high strength, and other excellent properties. Oxygen and niobium (Nb), as two representative alloying elements of Ti, are widely employed to form high-temperature and corrosion-resistant Ti alloys, as well as Ti-based high-entropy alloys tailored for various performance requirements. In recent years, the study of the α and β phases in Ti-O and Ti-Nb alloys has attracted much attention. However, the investigations on the thermodynamic characteristics of these phases remain incomplete. In addition, it is still difficult to achieve a comprehensive understanding of the thermodynamic properties and the microscopic mechanisms underlying thermodynamics.

One challenge is that oxygen, compared to other non-metallic elements, has a much higher solubility in Ti, which leads to the formation of various oxides at lower temperatures. For the elements Ti and Nb, the substitutional addition of both to each other's parent lattice will cause different degrees of lattice distortion, thereby introducing mechanical instability. Furthermore, the available studies and reports on the thermodynamics of hcp (α) and bcc (β) Ti-Nb-O systems and the underlying microscopic mechanisms are very scarce.

In this thesis, we combined first-principles calculations with the cluster expansion method to investigate the ground-states characteristics for these hcp and bcc binary and ternary systems. The atomic bonding interactions in these systems were first revealed based on the calculated

electronic structures. Afterwards, Debye-Grüneisen model and Monte Carlo simulations were employed together to investigate the thermodynamic properties of ordered and disordered phases in these systems. For the hcp Ti-O system, a new unreported compound with stoichiometry $Ti_{12}O_5$ was first discovered, and the effect of vibrational entropy on the order-disorder transition temperatures of the phases in the system was first examined. For the hcp and bcc Ti-Nb systems, a good agreement with experimentally reported phase boundaries between α and β phase is obtained through handling the mechanical instabilities introduced by the highly-distorted structures. Furthermore, the cluster expansion information obtained from the binary system was used as a starting point to investigate the energetics and thermodynamics of the hcp and bcc Ti-Nb-O systems, and the behind interaction mechanisms between oxygen and metallic Ti and Nb were also investigated. We believe that the findings and research methodologies presented in this dissertation provide significant insights and references for the structural prediction and material design of multi-component Ti-based materials (e.g. novel high-entropy alloys) as well as other binary and multicomponent metallic alloys.

Acknowledgements

This thesis marks as the end of a long journey that I could never forget in my whole life. First of all, I would like to express gratitude to my supervisor, Prof. Alessandro Mottura, for his comprehensive support during my PhD study. It has been an absolute pleasure working with him, and under his supervision, I have significantly improved my academic skills. He has not only taught me how to think about a research question independently, but also provided invaluable advice on my career development and personal growth. I have benefited greatly from his broad knowledge and meticulous guidance, and his patience and enthusiasm have inspired me to continue to pursue improvement. Thanks to his guidance and support, which lays a solid foundation for my future academic path and career.

I would like to express my sincere appreciation to my supervisor's colleague Danielle Williams who helped me arrange regular meetings with my supervisor and with things other than my research. I also want to acknowledge Prof. Mohan S. Devgun who provides PhD students in the school with travel funds to attend conferences for academic communications. With this funding and the support of my supervisor Prof. Alessandro Mottura, I had the opportunity to attend the World Titanium Conference. Besides, I would like to thank the BlueBEAR high-performance computing service provided by the University of Birmingham, which provides me with the platform to perform most of my modeling calculations. And I also appreciate the staff from IT service of the university for their support in the installation and debugging of the applications I requested. I would also like to express my appreciation to the China Scholarship Council (CSC) and the School of Metallurgy and Materials, University of Birmingham, for their significant

contribution in funding my tuition and living fees.

In the end, thanks to my parents and grandparents who give me life and the opportunity to achieve happiness. I would like to express my heartfelt gratitude to my wife Xue Lian for her endless love, support and understanding during my PhD period. She has been by my side throughout this long and challenging journey. She is not only my life partner but also my best friend and soulmate in my life. This thesis is dedicated to our daughter, Leyi (Chloe) Zhang, and I hope my sweetheart grows up to be a happy, brave, and independent woman.

List of Publications

Journal articles

1. **Zhang N**, Mottura A. First-principles thermodynamic investigation on the α phases in TiO and TiNb binary system. *The Journal of Chemical Physics*, 2024, 160: 194709.

(Author contributions: **Ning Zhang**: formal analysis, investigation, methodology, validation, writing-original draft, writing-review & editing. **Alessandro Mottura**: project administration, supervision, writing-review & editing)

2. **Zhang N**, Mottura A. First-principles statistical mechanics study on the thermodynamics of the bcc and hcp Ti-Nb-O ternary system. (In draft)

(Author contributions: **Ning Zhang**: formal analysis, investigation, methodology, validation, writing-original draft, writing-review & editing. **Alessandro Mottura**: project administration, supervision, writing-review & editing)

Conferences

1. **Zhang N**, Mottura A. First-principles investigation of the effect of interstitial oxygen and substitutional niobium on the thermodynamics of titanium, *15^{th} World Conference on Titanium*, 2023. (Oral)

2. **Zhang N**, Mottura A. Ab inito electronic structure calculation on the compounds and disordered phases in the hcp and bcc Ti-Nb-O ternary system, *BEAR Conference*, 2024. (Poster)

Contents

List of Figures

List of Tables

Chapter 1

Introduction

Different metallic and non-metallic elements can be alloyed with titanium (Ti) to form a variety of Ti alloys which can be applied in different fields. These elements can affect the structure and properties of Ti in different ways, which can be detected and characterized by some experimental and modeling techniques. However, sometimes it is knotty to predict the effects and behaviour of the addition of alloying elements due to some reasons like the high solubility of alloying elements or the presence of the mechanical instabilities introduced by the alloying elements. Therefore, a specific experimental or modeling scheme that can be used to investigate the variation of properties caused by the addition of the alloying elements into the Ti is promising. In this context, a modeling scheme that combines first-principles, cluster expansion method and statistical mechanics simulations was proposed in this chapter.

1.1 Ti and Ti alloys

1.1.1 Properties and Applications

As one of the well known refractory materials, Ti has many excellent properties like high strength, low density, low thermal conductivity and good corrosion resistance such that it has been widely used in various fields such as architecture, chemical processing, biomaterials and especially aerospace by alloying with several other elements like Al, Nb, Mo, Cr, and V [1–6]. Compared with other metals, the certain performance advantages of Ti can be seen from Table 1.1 [7–10].

Table 1.1: Some physical performance of Ti, Al, Fe and Ni [7–10].

Physical properties	Ti	Al	Fe	Ni
Density (g/cm^3)	4.5	2.7	7.9	8.9
Melting point (K)	1943	933	1811	1728
Thermal conductivity (W/mK)	15-22	221-247	68-80	72-92
Elastic modulus (GPa)	115	72	215	200
Reactivity with oxygen	high+	high	low	low
Corrosion resistance	high+	high	low	medium
Metal price	high+	medium	low	high

1.1.2 Alloy classifications

Pure Ti has two allotropes: hexagonal close packed (hcp, also called α-Ti) crystal structure at lower temperature, and it will transform to body-centered cubic (bcc, also called β-Ti) structure when the temperature is higher than 1155 K [11]. Typically, the mechanical properties of

Ti alloys can be improved while adding several elements into the alloys by controlling the temperature of the $\alpha \rightarrow \beta$ transition, this is an alloying process. This means the properties of an alloy can be tailored to the running environment by adding other elements. For instance, Zr and Sn are present in Ti alloys for use in compressor disc [12]. Alloying additions are divided into two groups: neutral, α and β stabilizers, which situate in either interstitial or substitutional sites in Ti crystal lattice, as shown in Table 1.2 [8, 13, 14]. The α and β stabilizers can increase and lower the $\alpha \rightarrow \beta$ temperature, respectively. However, neutral additions show very slight effect on this transformation temperature. On the other side, β stabilizers exactly have two classifications β-isomorphous and β-eutectoid. The former strengthens the stability of β phase along the whole composition while the latter leads to eutectoid decomposition of β phase. The effect of the above additions and the general classification of Ti alloys are shown in Figure 1.1 [8]. According to the above classification, Table 1.3 [7, 8, 14] shows some examples of Ti alloys for clear understanding.

Table 1.2: Some alloying elements in Ti and their occupation sites in crystal [8, 13, 14].

	α-stabilizer				β-etuectoid		β-isomorphous				Neutral	
	Al	O	N	C	Mo	V	Nb	Cr	Mn	H	Sn	Zr
Substitutional	✓				✓	✓	✓	✓	✓		✓	✓
Interstitial		✓	✓	✓						✓		

1) α and near-β alloys

Alloys that contain α stabilizers such as aluminum and oxygen which can stabilize α phase are called α alloys, such as pure Ti with a little oxygen impurity, Ti-5Al-2Sn-ELI, Ti-8Al-1Mo-1V. These alloys normally have high corrosion resistance and high-temperature properties, resulting in their wide applications in heat exchangers and the chemical processing industry where these properties are of prime concern [15].

Near-α alloys typically refer to the Ti alloys containing mainly α phase and less than 10 at.%

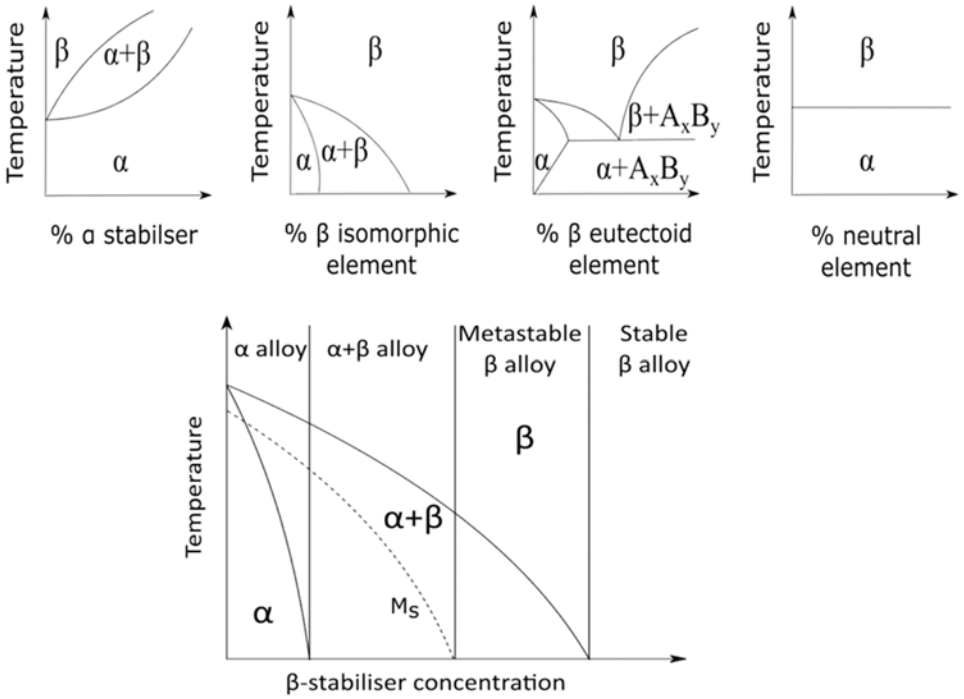

Figure 1.1: The effect of the addition of alloying elements on the α and β phases of Ti alloys [8].

α phase with adding 1~2 at.% β stabilizers into the alloys. The presence of β phase can improve the strength and machinability of the alloys, which makes these alloys own superior high-temperature mechanical properties, but the density is much lower than that of steels. From this reason, these near-α alloys can be used in the applications of aero-engine components suffering from high-pressure and high-temperature environments [16].

2) α + β alloys

α+β alloys contains both α and β phases by adding 4~16% β stabilizers, which can be heat treated. Depending on the environment in which they operate, α+β alloys are generally split into high-temperature and high-strength Ti alloys whose properties can be controlled through heat processing and the concentration of stabilizers. High-temperature α+β alloys, such as TIMETAL 834 and Ti-6Al-2Sn-4Zr-6Mo, are usually used in an aeroengine compressor disc accounting for their high creep strength and strength-to-weight ratio. For high-strength α+β alloys, they are widely applied in fan blades and aeroengine compressor running at low temperatures attributing to the combination of their high strength with excellent fatigue properties [17]. For example,

Table 1.3: Categories of Ti alloys and some examples [7, 8, 14].

Category	Selected materials			
CP-Ti	CP-Ti	CP-Ti	CP-Ti	CP-Ti
	(0.2Fe, 0.18O)	(0.3Fe, 0.25O)	(0.3Fe, 0.35O)	(0.5Fe, 0.40O)
α alloy	Ti-5Al-2.5Sn	Ti-3Al-2.5V	Ti-2Cu	Ti-0.3Mo-0.8Ni
near-α alloy	Ti-5Al-6Sn-2Zr-1Mo-0.2Si	Ti-2Al-2Sn-4Zr-2Mo	Ti-8Al-1Mo-1V	-
α+β alloy	Ti-6Al-4V	Ti-6Al-4V ELI	Ti-6Al-4V-2Sn	Ti-6Al-2Sn-4Zr-6Mo
β alloy	Ti-13V-11Cr-3Al	Ti-11.5Mo-6Zr-4.5Sn	Ti-13V-11Cr-3Al	-
near-β alloy	Ti-6Al-2Sn-4Zr-6Mo	Ti-8Mo-8V-2Fe-3Al	Ti-10V-2Fe-3Al	Ti-8Mn
Ti-Aluminides	Ti-24Al-10Nb	Ti-25Al-17Nb-1Mo	Ti-22Al-27Nb	-

Ti-6Al-4V (Ti-64) which accounts for over 50% of all Ti alloys in use nowadays has a high yield strength, good ductility and excellent corrosion resistance [18].

3) β and near-β alloys

Except for adding a specific number of β stabilizers, β and near-β alloys (also called metastable β-alloys) contain with and without small amount of α stabilizers, respectively. Some examples are Ti-10V-2Fe-3Al, Ti-15V-3Cr-3Al-3Sn and Ti-4.5Al-3V-2Mo-2Fe. The alloys in this category shows high toughness, good weldability and forgeability, and especially highest strength (>1400 MPa) among all classes of Ti alloys due to the effect of solid solution strengthening and age hardening. Thus, these Ti alloys are customarily spread in landing gear, aircraft fasteners and

sporting equipment [19, 20].

1.2 Problem statement

1.2.1 Oxygen ingress and oxidation resistance

Oxygen is a crucial impurity and/or alloying addition that severely affects the microstructure and properties of Ti and Ti alloys. Oxygen is the most common α stabilizer in Ti and Ti alloys, which can stabilize the α phase and rise the β-transus temperature, as shown in Figure 1.2 [21]. The oxygen in Ti and its alloys essentially comes from the gaseous medium in which they are located. Oxygen ingress generally occurs during the manufacture, forming and service of the Ti and its alloys.

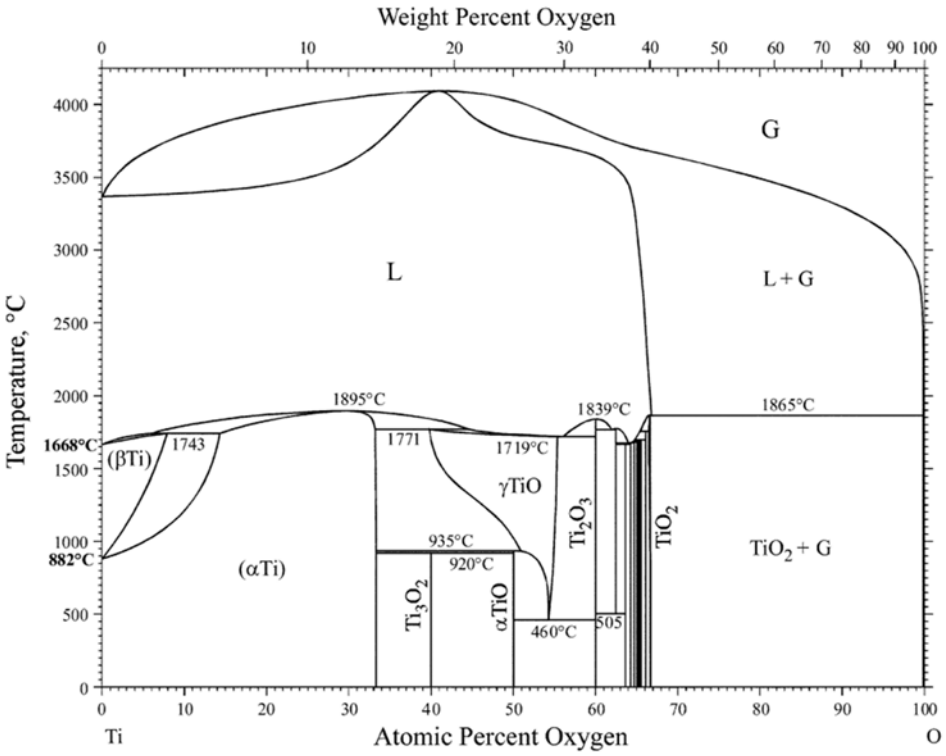

Figure 1.2: The effect of the addition of oxygen on the phase stability of Ti [21].

In the manufacture and forming processes of Ti (normally called “Kroll” process), Ti ores are normally used to extract Ti by reacting with coke and chlorine, then the reaction product is

reduced to pure Ti by reducing agent Mg. After that, in order to obtain high grade pure Ti, vacuum distilling is widely used to purify the reduced Ti, which highly increases the production costs. Forming, forging and heat treatment are eventually used to produce Ti products of various grades. A certain number of residual impurities including oxygen can seriously affect the properties of the fabricated product, though inert atmosphere or vacuum environment are commonly used in all aspects of production to hold these impurities at lower levels [22].

For another, the oxygen ingress can also occur in the service of Ti and Ti alloys, which is like some other metals like iron and aluminum. To be specific, firstly the exposure of metal to air results in the formation of an oxide layer on the surface of the alloy which exactly acts as a barrier layer by separating the metal surface from the environment. Then, oxygen from the environment diffuses through the passivating surface oxide layer forming a subsurface layer known as oxygen-rich layer or α case at temperatures below or above 753 K, respectively. At last, the oxygen in the brittle subsurface layer dissolves readily into the metal bulk and diffuses rapidly in it. The oxidation process of Ti is shown in Figure 1.3 [23]. For instance, as shown in Table 1.4, the maximum solubility of oxygen in α Ti can achieve 33 at.% which is 10 at.% higher than that of interstitial nitrogen [21, 24–26]. The diffusion rate of oxygen in pure Ti is approximately two orders of magnitude larger than that of nitrogen [27].

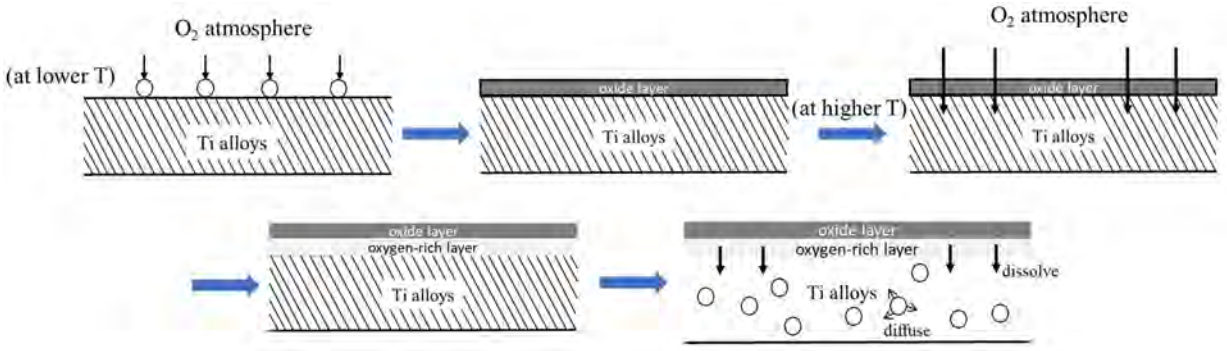

Figure 1.3: Schematic diagram of the oxidation process of Ti alloys [23].

The high affinity, solubility and diffusivity of oxygen in α Ti can have a significant effect on the mechanical properties of Ti alloys. Although most interstitial elements including oxygen can improve the hardness of Ti alloys by solid solution strengthening, this benefit is outweighed by

Table 1.4: Solubility limit of common interstitial elements in hcp-Ti [21, 24–26].

	H	B	C	N	O
Maximum solubility in hcp-Ti (in at. %)	7%	1%	2%	23%	33%

their heavily deleterious impact on toughness, ductility and fatigue resistance etc. For example, Shenoy *et al*. [28] reported that 80 % reduction in tensile elongation caused by the oxygen ingress occurred in Ti-6262 alloy. Leyens *et al*. [29] found that some cracks were observed in oxygen-penetrated area in Ti-1100 alloy, resulting in a great loss of ductility. The above examples are mainly caused by the fact that oxygen dissolves and diffuses in Ti alloy matrix mainly promoting the formation of oxygen-rich layer or α case under the oxide layer at various temperatures. Liu *et al*. [30] studied the effect of oxygen on the mechanical properties of Ti-6Al-2V and Ti-2Al-16V. Their results showed that the ingress of oxygen made these two alloys brittle to a certain extent, and both the oxygen impurity content and the embrittlement degree of alloys increased with the heat treatment.

In order to reduce the deterioration of Ti and its alloys introduced by oxygen ingress, many methods therefore were developed. There are generally three measures to achieve this, namely pre-oxidation, coatings and addition of alloying elements. Due to the occurrence of breakaway oxidation, cracking, peeling and degradation of the surface protection layer (shown in Figure 1.4), conventional processes of coatings and pre-oxidation can not provide a stable defense against oxygen ingress into the metal bulk [31, 32]. In contrary, alloying Ti with other elements to form binary or multicomponent Ti alloys is considered to be a more practical and effective way to render Ti with high oxygen-resistant competence inborn. Common elements used for alloying with Ti are Al, Nb, Sn, Si, etc. which are usually added to Ti in combination but with precise control of content to achieve balance between the needed alloy properties and oxygen-resistant competence.

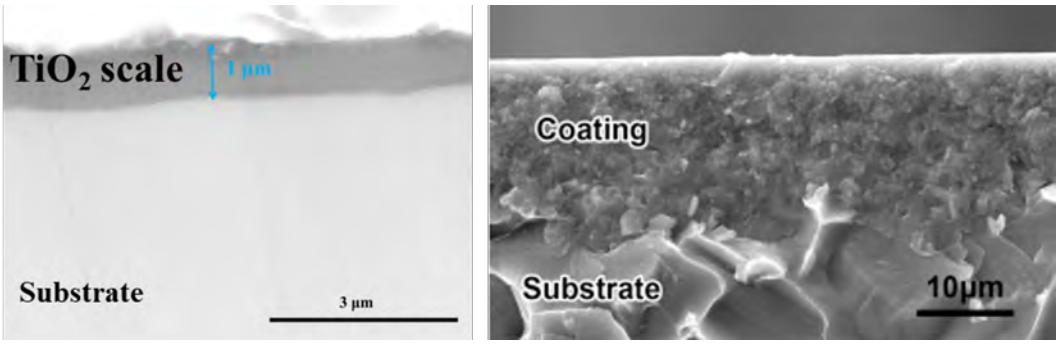

Figure 1.4: Surface protection layer of Ti alloys [31, 32].

1.2.2 Substitutional Nb in Ti

Niobium (Nb) is one of the important and common β stabilizers of Ti, and has body-centered cubic crystal (bcc) structure. It only can occupy the substitutional sites in Ti when alloying with Ti. Different compositional TiNb alloys exhibit a lot of excellent properties like good working plasticity, lower temperature superconductivity, low thermal expansion and good biocompatibility, which makes them broadly used in aerospace and superconducting industries [33]. In addition, like aluminum, Nb is often treated as the second alloying element of Ti, often working together with other nonmetallic and metallic elements to obtain multi-component Ti alloys such as Ti-Nb-Si and Ti-Nb-Ta-Zr [34, 35].

The variation of the content of Nb in Ti can cause large differences in the structures and properties of the formed TiNb alloys due to the different parent lattices of Ti and Nb. For instance, the lattice constants of TiNb alloys are very crucial parameters when developing the superelastic TiNb alloys. The α and β can coexist in the whole composition range of Ti and Nb, as shown in the phase diagram (Figure 1.5), and the α and β phases also differ in some characteristics [36]. The α phase can enhance the corrosion resistance of the body of TiNb alloy and normally does not react to heat processing, In another aspect, the β phase can be aged and solution treated to obtain an obvious enhancement in the yield and ultimate strength, and there is no occurrence of martensite transformation if fast cooling alloy from the β phase region. Besides, the β phase has a low value of elastic modulus, which, with the combination of nontoxicity of TiNb alloy, makes it possible for TiNb based alloys to be used in orthopedic implants. On the other hand,

the metastable stable α'' precipitates which have the orthorhombic crystal structure and appear from a martensitic transformation by quenching the TiNb alloy from single β phase at high temperatures also have been proven to contribute a lot to the low elastic modulus performance and good shape memory of TiNb alloy.

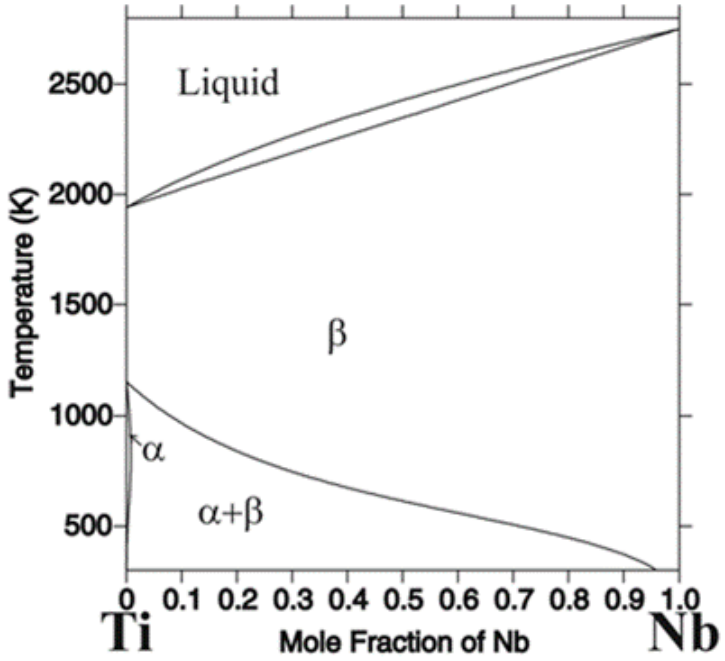

Figure 1.5: Phase diagram of TiNb alloy [36].

In view of the above, the α phase retains some of the characteristics of Ti itself, such as corrosion resistance and good heat workability, while the β and α'' phases play an important role in obtaining some specific properties of TiNb alloy. Therefore, it is fundamental and necessary to study the phase equilibria that occurs in TiNb alloys at different temperatures, especially the $\beta/(\alpha+\beta)$ phase boundary which determines conditions of the appearance of the β and α'' phase when cooling samples. Although there are many experimental and modeling investigations on the phase diagram of TiNb alloy, the reports on the in-depth understanding of the mechanisms underlying the mechanical and thermodynamic properties of TiNb alloys at the atomic scale are still lacking.

1.2.3 Oxygen addition into TiNb alloy

Many efforts have been made to improve the high-temperature oxygen-resistant competence of Ti, among all the beneficial elements, silicon and niobium are regarded as the most effective alloying elements. Silicon works by forming a SiO_2 protective layer to inhibit the oxygen ingress into the metal bulk [37]. The working mechanism behind the improvement of the oxidation resistance provided by the addition of Nb is not fully established, although the most likely explanation is that the stable Nb^{5+} ions lead to the compensation of Ti^{3+}, which can inhibit the proceeding of the oxidation [38]. Though some studies that refer to the oxidation of TiNb alloy can be found, no literature and thermodynamic data, to best of our knowledge, is open or published to describe the thermodynamics of hcp and bcc phases in the Ti-Nb-O system. Furthermore, no evidence can be found to investigate the mechanisms behind the properties and characteristics of the ternary Ti-Nb-O system.

1.3 Motivations of the thesis

1.3.1 Motivation for the study on the Ti-O, Ti-Nb and Ti-Nb-O systems

As mentioned above, oxygen has a very high affinity with α Ti and has the highest solubility in it, which makes oxygen in the environment gain much attention when Ti-based alloys are in service. As early as the 1970s, few modeling studies reported that the oxygen atoms in the sublattice of interstitial sites can form Ti_6O ordering in the disordered Ti α phase. Although a few simulation results in the past two decades also reported the existence of the other two ordering phases Ti_3O and Ti_2O in the Ti α phase and their phase region. However, in these studies, the reported order-disorder transition temperatures of these orderings differ a lot from each other especially for the Ti_2O ordering and have discrepancies with the early experimental data. Until very recently, as the first experimental evidence, Régis Poulain *et al*. [39] successfully observed the arrangement

of ordered precipitate Ti_6O in the Transmission Electron Microscopy (TEM) images of Ti-0.8O alloy, shown in Figure 1.6, after quenching the melted samples. It is a pity that they did not capture the precipitates with stoichiometry Ti_3O and Ti_2O. Moreover, to our knowledge, no literature reports and analyzes the formation mechanism from a microscopic perspective.

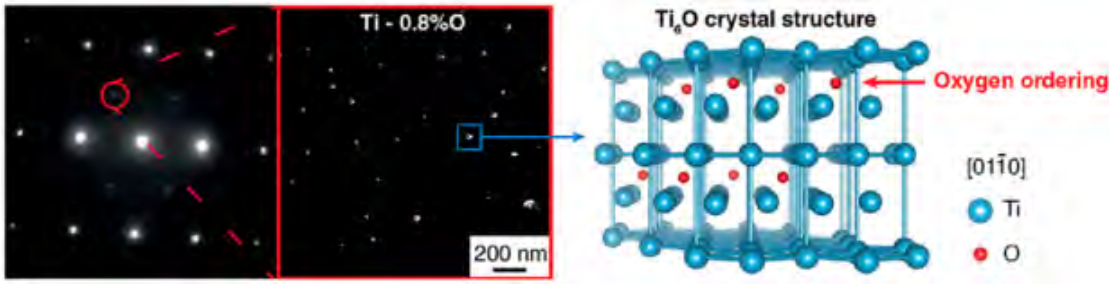

Figure 1.6: TEM images Ti-0.80 alloy and the crystal structure of the precipitate Ti_6O [39].

The development of the Ti alloys applied to the biomedical field has been a hotspot topic in recent years. The invention and manufacturing of implants with high biocompatibility even more has received widespread attention. As a typical β stabilizer of Ti, Ti-Nb alloys are promising materials for these applications which is attributed to the combined effect of the α, β and α'' phase. At low temperatures, the alloying between Nb and Ti can lead to the partial substitution of Nb in hcp Ti and Ti in bcc Nb, resulting in the coexistence of α and β phases. The metastable α'' precipitates come out when cooling Ti-Nb alloy from single β phase regions at higher temperatures [40]. Hence, the study on the phase boundaries especially on the $\beta/(\alpha+\beta)$ is essential for the control of the content of these three phases and the design of different compositional Ti-Nb alloys. Many studies have reported the phase diagram of Ti-Nb alloy [36, 41–43], whereas the insights into the formations of the α and β phases in different compositional Ti-Nb alloys from a view of atomic scale are lacking. In addition, some findings may have misunderstandings on the changes in alloy stability caused by the addition of Nb to Ti. For instance, Ravi Chinnappan *et al.* [44] found a few bcc structures with high relaxation and distortion and thus concluded that the bcc phase introduces more mechanical instabilities into Ti-Nb alloy, which is not rigorous and unconvincing.

Though a few studies are related to the addition of oxygen to Ti-Nb alloys, they either focus on

the formation mechanism of Nb_2O_5 [45] or the transformation mechanism of β to α'' [46]. The evidence on how the addition of oxygen forms bonds with Ti and Nb atoms and how the presence of oxygen affects the bonding between Ti and Nb atoms is very limited. The investigation on the properties of possible stable compounds in hcp and bcc phases in the Ti-Nb-O system and the thermodynamic properties of the ternary phases is also very scarce.

In view of above, there are still some questions that we are very concerned about. Firstly, for the Ti-O system, how does the oxygen atom interact with the Ti atom in the ordered α phases? How to obtain the accurate phase transition temperatures between the compounds and the disordered α phase? Secondly, for the Ti-Nb system, how does the solute interact with the solvent at different composition points? How do the interactions between Ti and Nb atoms affect the phase stabilities over a wide composition and temperature range? When Ti and Nb act as solutes to each other, which one is likely to introduce more mechanical instabilities into the solvent? Finally, when oxygen is introduced into the Ti-Nb system, how does it interact with Ti and Nb, and how does it affect the original Ti-Nb bonds? Are there any stable ternary compounds appearing in the α and β phases? How do the introduced oxygen atoms influence the properties and the thermodynamics of the α and β phases?

Hence, the design and development of experimental or modeling schemes that can provide comprehensive insights into addressing the above issues is potentially promising and remarkable.

1.3.2 Motivation for ab initio quantum mechanics method

Many experimental characterization techniques have been widely used to observe the microstructure of the alloy phases, investigate the thermodynamic properties, and detect the phase transitions, such as X-ray Diffraction (XRD), Scanning Electron Microscope (SEM), Thermoanalysis Technology (TG-DTA-DSC), etc.. Nevertheless, when scrutinizing the interactions and bonding mechanisms among different phase elements within alloys at the atomic level, some modern material computational techniques offer distinct advantages. These methods not only can pre-

cisely compute material phase transitions and thermodynamic characteristics, but also excel in revealing the structural arrangement of phases, the mechanisms of atomic interactions and even in mass transfer dynamics. Moreover, to achieve the experimental expectations, throughout the experimental procedure, quantifying and predicting the financial and temporal investments necessary for material preparation, processing, and characterization can prove challenging and indeterminate.

The phase transformation occurred in the alloy is essentially attributed to the significant and beneficial connection between the change of atomic spacing and interatomic-rearrangement and the electronic structure of metallic alloys. The gathering, arrangement and combination of diverse atoms result in a redistribution of electronic charges, forming bonds that predominantly govern the physical and chemical properties of all crystals.

As a quantum physics method without using empirical parameters and quantities derived from experiment, ab initio methods which are grounded in density functional theory (DFT) endeavor to investigate the structure and properties of materials through the resolution of intricate quantum mechanical equations, such as the many-body Schrödinger equation. This approach accurately computes the total energy and electronic structure of microscopic systems, rendering it applicable across various domains, as elucidated in the forthcoming chapter. The outcomes pertaining to the electronic structure and properties of materials facilitate further analysis of phase composition, atomic interactions and bonding mechanism in the ground-state. This enhances comprehension of phase formation and macroscopic physical and chemical properties in alloys from a microscopic standpoint. Furthermore, the ab initio method furnishes crucial initial parameters for investigating material properties at elevated temperatures by computing electronic energy information for various phase structures in the ground-state. Integrating the ab initio method with other material calculation techniques, such as common lattice vibration free energy calculation models and statistical mechanics methods, proves instrumental in exploring thermodynamic equilibrium and material properties across different temperature regimes. Leveraging these theoretical methodologies and technologies offers feasibility in delving into

this project.

Chapter 2

Literature Review and Research Background

This chapter firstly elucidates the application of first-principles methodologies in computing the electronic structure of phases within alloy systems, providing a robust practical underpinning for our study. Furthermore, an approach to accurately express the energy characteristics of alloys using the electronic structure information derived from first principles calculations, known as cluster extension formalism, is introduced. The application of this method in alloy materials is also summarized. Subsequently, a statistical mechanics approach capable of utilizing the Hamiltonian provided by cluster expansion is introduced for the computation of properties across various condensed matter systems, alongside its application in determining properties of interest in alloys. Meanwhile, the important interrelation between first-principles calculations, cluster expansion formalism, and statistical mechanics approaches is elaborated. In conclusion, the research content and significance of the thesis are detailed, accompanied by a succinct summary of the contents of each chapter.

2.1 First-principles applications and developments on materials

The ab initio method, also referred to as first-principles calculation or DFT calculation, typically relies solely on physical constants as input. This quantum computational technology has found extensive application across diverse fields including chemistry, physics, catalysis, environmental engineering, and materials science [47]. In particular, in the field of materials, it can accurately calculate the electronic structure and energy of materials without necessitating experimental or semi-empirical parameters, thereby enabling the prediction of the physical and chemical properties of materials and yielding results very close to experimental data [48, 49]. For instance, many properties such as dielectric properties, optical properties, ferroelectric pyroelectric properties, elastic constants, and charge density can be optimized and designed through first-principles calculations [50].

The applications of first-principles calculations in alloy systems hold significant importance and extend extensively. For instance, the development of high-performance magnesium alloys remains a prominent research focus, yet comprehensive experimental data on the thermodynamics, kinetics, and phase stability of multicomponent magnesium alloys is lacking. To supplement the missing experimental information, employing first-principles calculations presents an effective approach, offering numerous opportunities to expedite the development of forthcoming magnesium alloys [51]. On the other hand, as a research hotspot in the field of materials in recent years, novel energy materials and multicomponent complex alloy materials, especially battery materials and high entropy alloys, have garnered widespread interests. First-principles calculations likewise provide powerful support for the theoretical fundamentals and the in-depth understanding of the microscopic mechanism in analyzing the structures and properties of these materials. As an example, employing first-principles calculations, some key properties of magnesium ion batteries like electrochemical performance and underlying reaction mechanism have been successfully anticipated and investigated by simulating the interactions between Mg^{2+} and

electrode, which aids in advancing the innovation of novel energy materials [52]. Another example, under diverse environmental conditions, the occurrence of phase decomposition in high entropy alloys is an important factor affecting their mechanical properties. Predicting this decomposition necessitates the establishment of phase diagrams specific to high entropy alloys. Yet, the direct calculation of the phase diagrams from both experimental measurements and theoretical computations is greatly hindered, primarily stemming from the complex multi-dimensional composition space involved. Recently, Chen Shuming *et al*. [53] used first-principles calculations to successfully predict and analyze the effect of phase decomposition in HfNbTaTiZr high entropy alloys on alloy strength by treating the HfNbTaTiZ high entropy alloy as multiple pseudo-binary alloy systems.

Additionally, the first-principles method has similarly contributed to the advancement of novel Ti alloys and enhanced our understanding of atomic interactions inside alloys. As an illustration, Zhou Wenchong *et al*. [54] investigated the mechanical stability and elastic properties of Ti-Mo, Ti-Al, Ti-Sn, and Ti-Zr alloys with hcp and bcc structures, across various compositions, employing first-principles calculations. They assessed the phase stability of these alloys by computing the formation energy of the constructed disordered supercells and correlated the calculated electronic density of states (DOS) with the stability of the hcp and bcc phases. Jun Hui *et al*. [55] studied the twin energies of 14 metallic elements, including Ni, Cu, V, Nb and Al, in Ti via first-principles calculations and unearthed the strengthening or embrittling effects at the twin boundaries. It was further revealed that the essence of this strengthening and embrittlement effect is attributed to the electronic interactions by analyzing the charge density and density of states of these alloying elements. These findings hold potential significance for the advancement of novel hcp alloys, as the control of twin boundary characteristics via alloying with solute atoms presents a viable strategy for regulating metal microstructures and enhancing the mechanical properties, such as strength and ductility, across various Ti alloys.

The thermodynamic and dynamic behavior of interstitial nonmetallic elements in metal and alloys, as well as the effects of their addition on the structure and properties, are also focal points

of concern for many researchers, and first-principles calculations have made many breakthroughs and progress in these topics. For instance, meeting the demand for cost-effective production of pure H entails the development of ultra-thin, high-permeability palladium-based membranes capable of withstanding elevated temperatures and pressures over prolonged operational time, as commonly encountered in petrochemical sectors. Upon alloying Pd with Au or Ag to fabricate a membrane, enhanced anti-embrittlement performance can be obtained compared to the membrane composed of pure Pd. Chandrashekhar G. Sonwane *et al*. [56] used first-principles methods to compute the lattice expansion and binding energy of PdAu and PdAg alloys with various compositions, and then calculated the solubility of H in these alloys using Sievert's law equation. The expansion effect caused by the dissolution of H in these alloys and the identification of competent PdAg or PdAu alloys at diverse temperatures and pressures were further illustrated. However, this simulation thought cannot be applied to predict the solubility of O in Ti alloys, as the solubility of O in many Ti alloys is very high (33 at.% in pure hcp Ti), and Sievert's law is no longer applicable in these cases. Jin Wang *et al*. [57] analyzed the dissolution behavior of oxygen in Nb-Cr alloy by calculating the enthalpy change of oxygen using first-principles calculations. They further concluded that the dominant driving force for oxygen dissolution is chemical effects when the Cr concentration is 4 at.% or lower, whereas the combination of elastic and chemical interactions reversely play a main role in hindering the dissolution of oxygen in Nb-Cr alloys with Cr concentration higher than 4 at.%. These findings can assist people in better understanding the dissolution behavior of interstitial elements especially oxygen in alloys. The studies on solubility and diffusion kinetics of oxygen in Ti alloys are also documented in a few papers. Enrica Epifano *et al*. [58] computed the barrier energies for the boron and oxygen migration between different stable interstitial sites in γ TiAl alloys using the Nudged Elastic Bond method performed by the ab initio calculations, then the minimum energy path for the migration of interstitial oxygen and boron was confirmed. The diffusion coefficient of these elements in the γ TiAl alloys were further determined by the multi-state diffusion method. These research findings possess the potential to unveil latent anisotropic behaviors unobserved in experimental data, whilst concurrently addressing deficiencies in kinetic

databases pertaining to the same. Moreover, the interaction energies between the metallic solutes and the oxygen occupying different interstitial sites in hcp Ti were computed by Henry H. Wu *et al*. [59], which revealed the mechanism of attraction or repulsion between solutes and oxygen. The effects of solutes on oxygen diffusion barriers in hcp Ti were quantified using an activation barrier approximation. Subsequently, a numerical diffusion scheme was established to assess the alterations in oxygen diffusivity across a range of solute concentrations. This developed diffusion model facilitates the exploration of the influence of different solute distributions on oxygen diffusion dynamics.

The electronic structure method based on density functional theory, also referred to as first-principles simulation technology, has transcended its initial theoretical domain confined solely to condensed matter physics and quantum chemistry. First-principles calculation has been extensively applied by researchers in the study of a wide range of materials, encompassing electronic structure analysis, energy characteristics calculation, phase transition detection, dynamic behavior exploration, and identification of the microscopic origin of macroscopic properties. This computation technique has driven a new paradigm of research approach in understanding, predicting, and designing the accuracy and efficiency of material properties. Furthermore, in recent years, the integration of first-principles calculations with machine learning technology has emerged as a highly promising approach for material design and development, offering the potential to significantly narrow the disparity between material computation and experimentation. Given the above, leveraging first-principles calculations to investigate the physicochemical behavior of oxygen and niobium in Ti presents a notably viable avenue of exploration.

2.2 Application of cluster expansion methods in alloy systems

In numerous disciplines, it is commonplace to conduct parameterization of either physical or empirical models using a collection of meticulously accurate yet costly calculations or measurements, thereby yielding less precise albeit more economical predictions. Within the realm

of computational materials science and solid-state physics, the cluster expansion (CE) method offers a direct estimation of the lattice's free energy, or any other thermodynamic parameter, through a discrete cluster function [60, 61]. The CE method establishes a mathematical model enabling the representation of various scalar quantities of a crystal, such as formation energy, enthalpy, and elastic strain energy, through multisite correlation functions. This method stands as one of the foremost utilized approaches in the prediction and design of materials. Achieving optimal alloy design demands a deep understanding of how defects affect deformation behaviors and origin of strengthening of the precipitates and solid solutions. The intrinsic capability of the CE formalism depicting various degrees of configurational order (or disorder) renders it a very useful methodology for discovering the interactions of alloying elements, phase composition, and structural imperfections.

It needs to be pointed out that Axel van de Walle *et al*. [62] found that CE can directly express the energy of the whole alloy using the energetics of some configurations with various compositions calculated by DFT, thereby enabling the prediction of the energies of any compositional structure. In simple terms, CE method possesses the capability to derive the energetics of the whole system from the energetic information of a small number of structures. The alloy systems people focus on generally consist of several or even multiple phases under different service conditions, and whether ordered or disordered, there are normally the presence of antiphase boundaries (APBs) at the interfaces between two contacting domains. CE can easily capture these APBs using energetic information from these sampled structures and derived ground states, thereby enabling the predictions of phase transitions. For instance, Ruoshi Sun *et al*. [63] applied CE method to straightforward calculate the energy of Ni_3Al in the presence of an APB and investigate how Ti and Hf additions affect the APB energies. In addition, the CE method was employed by Mohammad S. Dodaran *et al*. [64] to investigate the change of APB energies of the ordered γ' precipitates in Ni-based high-temperature alloys.

For another, not only the energetics of the pseudo defects like APB that maintain the original symmetry of the crystal lattice can be computed by CE, but also some other planar defects

capable of breaking the ideal lattice symmetry are able to be examined. In other words, CE method is also a powerful tool that can be employed to study common surface problems such as surface segregation, gas absorption, and precipitations. In terms of the studies on surface segregation, it can be easily achieved by the construction of another CE for the surface except for the alloy bulk CE construction, whereas more clusters need to be included in the surface CE construction to achieve an approximate accuracy as studying the alloy bulk. As an illustration, Drautz *et al*. [65] employed a CE method to explore the contest between the inclination for Al segregation and ordering in the Ni–Al alloy, wherein ordering arises from the breaking of lattice symmetry at the surface. In their study, 24 clusters were selected in the CE to examine the Ni-Al alloy bulk, whereas the other CE used for surface investigation involved 400 clusters, despite some clusters having insignificant interaction values. In another study, a coupled CE method was established by Han *et al*. [66] to investigate segregation and surface ordering behavior attributed to the oxygen absorption on the surface of Pt with a small amount addition of Ru. Similarly, a study about the absorption of a diverse number of H atoms on the Ir surface using an extended CE method was proposed by Lerch *et al*. [67]. Employing the CE approach to explore the thermodynamic and kinetic characteristics of precipitations in structural alloys can enhance our comprehension of the precipitation hardening process and its mechanisms. For example, the mixed-space CE method was used in a few studies to investigate the energetics and temporal changes in the distribution of precipitate shapes and sizes in Al-Zn alloy [68]. Therein, a pair in reciprocal space and a many-body cluster like triplet in real space were combined to form the mixed-space CE.

More importantly, performing CE for an alloy system allows for the identification of pivotal clusters, such as pairs, triplets, and quadruplets, which are instrumental in expressing the energy of the alloy at the ground-state. Additionally, the interactions among these sites, known as effective cluster interactions, can also be derived for each cluster. These important clusters and effective cluster interactions contain valuable energetics information of the alloy, which not only indirectly reflects sites with stronger interactions between elements in the alloy system but also provides front-end inputs (Hamiltonian) for statistical mechanics techniques like Monte Carlo

simulations. Through further performing statistical mechanics simulations, the thermodynamic properties of various phases in the alloy at finite temperatures can be readily computed. It is worth mentioning that, as a pioneer, Axel van de Walle *et al*. [69] first obtained the energetics of the Ti-Al system by constructing the CE, then they successfully calculated the potential surface and Gibbs free energy data for the Ti-Al system by conducting Monte Carlo simulations imported with the CE results.

To summarize, cluster extension formalism stands out as a crucial methodology capable of approximating the energetics of structures using DFT data. This approach has found extensive application in exploring the energy of alloys and the thermodynamic behaviors of various phases. Moreover, its perfect integration with statistical mechanics methods has broadened its applicability. The advancements made in cluster expansion methods in these research fields offer valuable insights and theoretical fundamentals for our investigations on Ti-O, Ti-Nb, and Ti-Nb-O systems.

2.3 Overview of Monte Carlo simulations in statistical mechanics and its applications

Statistical mechanics is a branch of theoretical physics that aims to understand and predict the behavior of macroscopic systems by examining the statistical properties and dynamics of their microscopic constituents. It provides a framework for describing how the properties of matter arise from the behavior of its individual particles, such as atoms and molecules, under the influence of thermal energy [70–72]. Statistical mechanics utilizes principles from probability theory and statistical methods to analyze the distribution of particles in various states and their interactions, ultimately yielding predictions about the thermodynamic properties and behavior of condensed matter systems at the macroscopic scale. However, some basic goals about the calculations of the expectation values of some quantities in a system in statistical

mechanics cannot be solved in the practical application. For example, one possible method to solve the multivariable integral such as partition function is to exhaustively list all conceivable configurations of the system and compute the averages arbitrarily [73, 74]. This can be achieved in fully solvable systems as well as in simulations of simple systems with a small number of particles, whereas, in realistic condensed matter systems, a full and accurate enumeration of the systems theoretically should be very hard and impossible to perform due to that these systems are composed of very many parts and different types of atom or molecule.

To solve these issues in these real complex systems, Monte Carlo numerical method, as a computational technique, can be employed to model complex systems by generating random samples from a probability distribution to approximate the behavior of the system [75, 76]. In Monte Carlo simulations, random numbers are used to sample the possible configurations of a system according to a specified probability distribution, and statistical averages are computed from these samples to estimate the properties of the system. This technique was initially invented by scientists Nicholas Constantine Metropolis *et al*. [77] to address complex problems in nuclear physics reactions that were difficult to solve. Nowadays, Monte Carlo simulation has been widely applied in many disciplines such as physics, chemistry, finance, economics, and biology.

The underlying mechanism of Monte Carlo simulation is to conceptualize the system as a vast and random system, leverage the principle of random sampling to explore the potential system outcomes, and offer probabilistic estimations of system behavior. Through repeated simulations with numerous random samples, Monte Carlo simulation extracts insights into system stability, structural characteristics, and responsive tendencies across diverse conditions. Monte Carlo simulation mainly includes the following steps: problem formulation, random sampling, model construction, simulation execution, statistical analysis, convergence testing and results interpretation [78, 79]. The most important step among them is the random sampling phase. Random sampling is essential because it allows the simulation to explore a wide range of possible scenarios and outcomes, capturing the uncertainty inherent in the parameters of the system. The quality and adequacy of the random sampling directly influence the accuracy and

reliability of the simulation results. Therefore, careful consideration and implementation of random sampling techniques are critical to the success of a Monte Carlo simulation. In addition, Monte Carlo simulation offers several advantages compared to other numerical computation methods in statistical mechanics:

(1) Generality: Monte Carlo simulations are highly versatile and applicable to a wide range of systems, from simple models to complex, interacting particle systems. They can be used to study equilibrium and non-equilibrium phenomena, phase transitions, and critical behavior across various disciplines [80].

(2) Statistical accuracy: Monte Carlo simulations provide statistically accurate estimates of system properties by averaging over a large number of random samples. This statistical approach allows researchers to obtain precise results even in the presence of significant fluctuations or uncertainties.

(3) Sampling efficiency: Monte Carlo simulations efficiently explore the configuration space of a system by sampling from probability distributions, focusing computational resources on regions of interest. This makes Monte Carlo methods particularly suitable for studying high-dimensional systems with complex energy landscapes [81].

(4) Scalability: Monte Carlo simulations can be easily scaled to handle systems of varying sizes and complexities. By adjusting the number of simulation steps or the number of samples, researchers can optimize computational efficiency and achieve results for systems of practical interest [82].

(5) Flexibility: Monte Carlo simulations can incorporate various sampling techniques, such as Metropolis-Hastings, Gibbs sampling, or importance sampling, to tailor the simulation approach to the specific problem at hand. This flexibility allows researchers to adapt Monte Carlo methods to different system configurations and study objectives [83].

In materials science, Monte Carlo simulations find extensive application for studying the struc-

ture, properties, and behavior of materials at the atomic and molecular levels, some key applications include:

(1) Phase diagram calculations: Monte Carlo simulations are used to predict phase diagrams of materials by simulating the behavior of atoms or molecules at different temperatures and pressures. These simulations provide insights into phase transitions, such as melting, solidification, and phase coexistence, aiding in the design and optimization of materials processing techniques. An example is a Monte Carlo simulation of the phase diagram calculations of the fcc binary alloy [84].

(2) Defect formation and diffusion: Monte Carlo simulations are employed to investigate the formation, migration, and annihilation of defects (e.g., vacancies, interstitials, dislocations) in materials. By modeling defect kinetics and thermodynamics, Monte Carlo simulations help understand defect-induced phenomena such as diffusion, grain growth, and mechanical properties. For example, Howard L. Heinisch *et al*. successfully found the mixed one-dimensional and three-dimensional defect migration of some interstitial atoms in metals [85].

(3) Atomic scale modeling: Monte Carlo simulations are used to model the atomic structure and dynamics of materials, including crystalline, amorphous, and nanostructured systems. These simulations provide insights into atomic arrangements, bonding mechanisms, and surface/interface properties, contributing to the development of new materials with tailored properties. As an illustration, Lucia Scotti *et al*. revealed the diffusion mechanism of the O, N, and C in hcp Ti by performing kinetic Monte Carlo simulations [86].

(4) Thermodynamic properties: Monte Carlo simulations are employed to calculate thermodynamic properties of materials, such as enthalpy, entropy, and free energy, under different conditions. These simulations aid in predicting material stability, phase transformations, and reaction kinetics, guiding the design of materials for specific applications. S. J. Wierzchowski *et al*. presented an approach to compute free energies and chemical potentials in molecular models of gas hydrate systems via Monte Carlo simulations [87].

Overall, Monte Carlo simulations play a crucial role in advancing our understanding of materials science phenomena, providing predictive capabilities for the design, characterization, and optimization of materials across various applications. Hence, employing Monte Carlo simulation to study the phase equilibrium and thermodynamic properties of the various phases in Ti-O, Ti-Nb, and Ti-Nb-O at finite temperatures is highly feasible.

2.4 Scope and Outline of the thesis

In the previous sections, we outlined first-principles calculations, cluster extension methods, and Monte Carlo simulation, and summarized their applications across various fields, especially in materials science. These methodologies offer a crucial avenue for investigating the physical and chemical properties of materials in varied states, and the underlying interactions between the constituent atoms or molecules. At first, energetics information of a specific number of structures in the interested system at ground-state is computed using first-principles calculations. Subsequently, these structures are linked via cluster expansion methods to predict the energetics information of the system across various chemical compositions. At last, the cluster data obtained from cluster expansion serves as a Hamiltonian for Monte Carlo simulation, thereby extrapolating the ground-state energetics of the existing phases to that in different temperature and pressure conditions.

In this dissertation, based on the integration of the above three methodologies, a framework is developed for comprehensive insights into the interatomic interaction and thermodynamic behavior of the additional interstitial oxygen and/or substitutional Nb in Ti. We believe that the novel scheme provided here would be valuable for investigating the electronic structure, energy characteristics, and thermodynamic properties of other metal alloys. Chapter 3 illustrates the workflow of this study and the details about how to integrate these three methods into an interrelated framework. Moreover, the algorithm and computation parameters of each method are also described in detail. Chapter 4 presents the crystal structures of the ground states discovered in

the hcp Ti-O system, and analyzes the electronic structures of these structures in order to reveal the underlying mechanisms of interatomic interactions between oxygen and Ti atoms. On the other hand, the crucial clusters including pairs, triplets, and quadruplets are examined and their interactions are quantified by the cluster expansion formalism. Furthermore, some thermodynamic properties such as vibrational free energies, heat capacities, and transition temperatures are calculated by a transformed Debye model and Monte Carlo simulations. Chapter 5 provides the properties of the ground states found in the hcp and bcc Ti-Nb systems and then presents the thermodynamics of these two systems at finite temperatures, and establishes the phase diagrams for the bcc and hcp phases. Chapter 6 extends the ground-state energetics obtained in Ti-O and Ti-Nb binary systems to help establish the cluster expansion for the Ti-Nb-O ternary systems. For those novel ground states found in the CE, the electronic structures and interatomic interactions between Ti, Nb and O are studied. Moreover, the thermodynamics of the appeared phases were computed for the first time. Chapter 7 discusses the results of Chapters 4, 5 and 6, and reveals the inherent connections between the previous three chapters from the view of the atomic scale. Chapter 8 summarizes all results and discusses future directions for additional research.

Chapter 3

Theoretical and Computational Methods

Based on quantum physics and density functional theory, first-principles calculations can extensively predict a wide variety of physical and chemical properties of any kind of atomic system without relying on experimental data. It can determine the electronic structures of materials to reveal the interactions between atoms and electrons at a microscopic level, thereby explaining the physical phenomena of materials. As a powerful backend for DFT calculations, the CE method and MC simulation based on quantum mechanics and statistical mechanics can capture the DFT energetics information and extend it to different environmental conditions, such as high temperature and high pressure, to meet the conditions under which materials are in service in practice. This enables the determination of the physical and chemical properties of materials under different temperature and pressure conditions.

In this dissertation, the finite temperature thermodynamics of the Ti-O, Ti-Nb, and Ti-Nb-O systems were determined using a combination of DFT calculation, CE, and statistical mechanics MC methods. Additionally, DFT calculations were employed to discuss the underlying mechanism behind the computed properties. This chapter outlines the theories and methodologies used to study the Ti-O, Ti-Nb, and Ti-Nb-O systems. Section 3.1 provides a flow chart to shape the calculation framework by connecting the DFT calculation, CE method, and MC simulations.

Subsequent sections delve deeper into the theoretical foundations of each part of the workflow. Section 3.2 gives a detailed introduction to the theoretical foundations behind DFT calculation, as well as its implementation in computation software. Section 3.3 introduces the theory behind the CE method, its predictive ability, and how CE connects with DFT calculation, the thermodynamic Debye model, and MC simulation. Section 3.4 Section 3.6 elaborates on the concepts of the MC simulations, the algorithms behind the MC simulation, and how to interpret the data from MC to Gibbs free energy.

3.1 Workflow

Before delving into the methodology, a brief analysis of the positional occupation of O, Ti, and Nb in crystals is necessary. For all the metallic systems, oxygen can only occupy the interstitial sites in Ti [11, 88]. For hcp crystal lattice, the interstitial sites include octahedral, tetrahedral, crowdion, basal octahedral, hexahedral and basal crowdion sites [86], as shown in Figure 3.1. The stabilities of these interstitial sites for oxygen occupation were examined by performing DFT calculations for a set of supercells with 32 Ti and 1 oxygen atoms which were placed in substitutional and corresponding interstitial sites respectively. The total energies of these supercells and the positions of these oxygen atoms before and after relaxation are shown in Table 3.1. Among all the interstitial sites, only three of them are stable for oxygen occupation, namely the octahedral site, hexahedral site, and crowdion site. The most stable site for oxygen occupation in Ti is the octahedral site where the supercell has the lowest total energy of -258.86 eV. For bcc crystal structure, similarly, the most stable interstitial sites occupied by oxygen are also octahedral sites. Therefore, in this study, in all systems containing oxygen, the oxygen atoms are placed at the positions of octahedral sites to obtain configurations with lower energies. On the other hand, Nb and Ti can only occupy the substitutional sites in the hcp and bcc crystal lattice, respectively [89–91].

The entire computational process commences with the construction of a parent lattice, based on

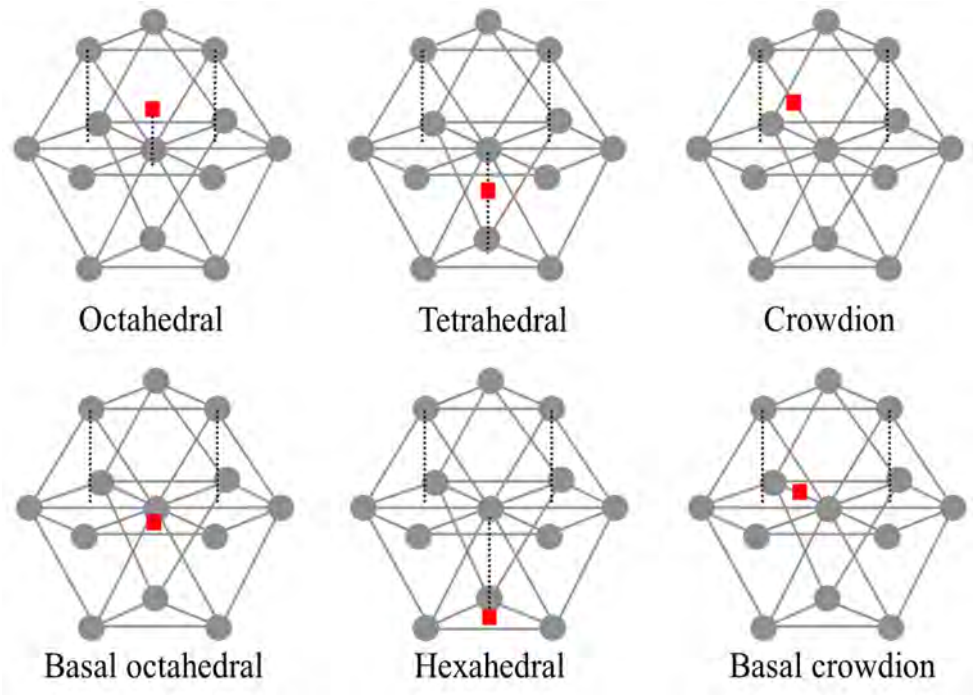

Figure 3.1: Interstitial sites in the hcp crystal lattice [86].

Table 3.1: Stability of the supercell $Ti_{32}O$ when oxygen sited in different interstitial sites.

Interstitial sites for oxygen occupation	Position after full relaxation	Total energy (eV)
Octahedral site	Same octahedral site	-258.86
Tetrahedral site	Neighboring octahedral site	-258.86
Hexahedral site	Same hexahedral site	-257.57
Crowdion site	Same crowdion site	-257.35
Basal crowdion site	Neighboring hexahedral site	-258.54
Basal octahedral site	Basal octahedral site	-255.81

the crystal structure of the system under examination, along with the degrees of freedom across the different sublattices existing in the crystal. As an illustration, in the Ti-O system, the parent crystal is the hcp crystal lattice, and Ti and oxygen atoms distribute to two different sublattices. In

other words, Ti occupies the metal sublattice of hcp crystal, namely the substitutional sites with the close packed triangular lattice planes. Since the formation energies of the structures with vacancies on this sublattice are above zero, there are no degrees of freedom on this sublattice, and all sites on this sublattice are occupied by Ti atoms. For the octahedral interstitial sublattice, not all sites are occupied by oxygen atoms, thereby oxygen and vacancies are randomly arranged on this sublattice. For the hcp Ti-Nb system, there is no sublattice, only the metal lattice has degrees of freedom, and both Ti and Nb atoms are allowed to randomly occupy substitutional sites. After constructing the parent lattice, the factor group that represents the symmetry of the primitive configurations will be computed. Subsequently, different atomic arrangements are enumerated on the sublattice having degrees of freedom to obtain configurations of varying sizes with different compositions and/or atomic arrangements. Meanwhile, the symmetry operations performed in the factor group ensure that all the enumerated configurations are unique in terms of symmetry. The next step is to relax all configurations through DFT calculations and compute the minimum energy when these configurations achieve equilibrium. Thereby, by counting the number of atoms in each configuration and taking the energies of configurations composed of two endpoint components as a reference, the formation energy of each configuration can be calculated. Then, by putting the formation energies of all configurations together, with composition and formation energy as the x and y axes respectively (with formation energy as the vertical z-axis in ternary systems), we can obtain the convex hull of the formation energies across varying compositions. The stable ground-state orderings with different compositions can be identified from the convex hull. The CE can determine the crucial clusters associated with each system based on all the configurational energies. The corresponding effective cluster interactions (ECIs) which refer to the interactions between atoms in the clusters can be computed by CE. In addition to configuration energy, temperature-dependent vibrational free energy and thermal expansion can also be calculated. The first step is that the length-dependent force constants are computed for each configuration, and next vibrational free energy and thermal expansion of each configuration are evaluated using harmonic or quasi-harmonic approximation. Similarly, these vibrational free energies can be used to construct another CE to obtain vibrational ECIs. The

temperature-dependent total ECIs (tECIs) can be obtained by summing up the configurational ECIs and vibrational ECIs. Eventually, the initial parent lattice, the configurations of the stable ground states, the clusters, and the tECIs are used as input to perform MC simulations to compute the thermodynamics at finite temperatures. The electronic free energy is attributed to the distribution of electrons across different energy levels, and the electronic states near the Fermi level are mostly filled. It is not included in all the systems as it is several orders of magnitude smaller compared to the configurational free energy and vibrational free energy, thus having minimal impact on the thermodynamic properties. The magnetic free energy is not considered as well since no literature reported that magnetism exists in any Ti-O and Ti-Nb compounds. Figure 3.2 shows the overall workflow that was adopted in this study. The following sections of the chapter introduce the computation details and the theory behind each computation methodology.

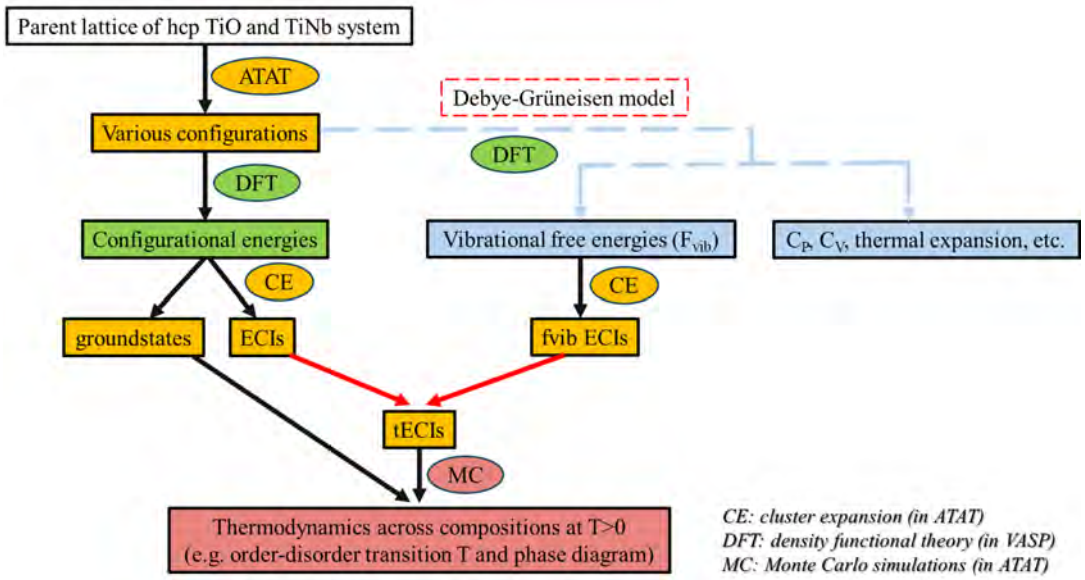

Figure 3.2: Workflow of this study.

3.2 First-principles calculations

With the establishment of the quantum mechanics theory in the early 20^{th} century and the advent of powerful computers and numerical techniques in the late 20^{th} century, first-principles

calculations began to be practically implemented in the field of material calculations [92]. First-principles calculations aim to solve many-particle problem without relying on any empirical parameters and experimental data, thereby achieving the prediction of the electronic structure and energy characteristics of materials.

3.2.1 Many-particle problem

In the realm of first-principles calculations, one of the central challenges lies in accurately describing the interactions among multiple electrons and nuclei within a given system. This complex interaction, often referred to as the many-particle problem, arises due to the quantum mechanical nature of electrons, which necessitates a comprehensive understanding of their behavior within a material or molecule [93]. At the heart of this endeavor lies the formulation and solution of the many-electron Hamiltonian, a cornerstone in quantum mechanics that encapsulates the dynamics of a system composed of multiple interacting particles. The ground-state of a many-electron system can be described using the many-particle Schrödinger equation [94] with linear operator:

$$H\Psi = E_{DFT}\Psi \tag{3.1}$$

where Ψ is the many-particle wave function that denotes the current state of the system, eigenvalue E which represents the solution of the equation is the energy of the system, and H is the Hamiltonian operator of the system. Both Ψ and H depend on the positions of the electrons (r_1, r_2, ...r_N), and nuclei (R_1, R_2, ...R_M). H can be obtained by simply summing up kinetic (T) and potential contributions (V) by [94]:

$$H(\overrightarrow{r}, \overrightarrow{R}) = T_e(r_i) + T_n(r_i) + V_{ee}(r_i, r_j) + V_{en}(r_i, R_j) + V_{nn}(R_i, R_j) \tag{3.2}$$

$T_e(r_i)$ and $T_n(r_i)$ indicate kinetic factor of electrons and nuclei, respectively. V_{ee}, V_{en}, and V_{nn} represent the Coulomb potential interaction between electron-electron, electrons-nuclei, and

nucleus-nucleus, respectively. Each term can be expanded as:

$$\begin{aligned} T_e &= \frac{1}{2m}\sum_{i=1}^{N_e} p_i^2 \\ T_n &= \frac{1}{2}\sum_{k=1}^{N_n}\frac{1}{M_k}P_k^2 \\ V_{ee} &= \frac{e^2}{2}\sum_{i,j}{}' \frac{1}{|r_i - r_j|} \\ V_{en} &= -e^2\sum_{i,k}\frac{Z_k}{|r_i - R_k|} \\ V_{nn} &= \frac{e^2}{2}\sum_{k\neq l}\frac{Z_k Z_l}{|R_k - R_l|} \end{aligned} \tag{3.3}$$

where m and e denote the mass and charge of the electron, p_i and P_k represent the torque operators for electron i and nucleus k, respectively. N_e and N_n refer to all the electrons and nuclei in the system. T_n can be assumed to be zero as calculated at 0 K when analyzing a system of stationary ions as the nuclei are considered to be static state. M_k and Z_k are the mass and nuclear charge of the ion k, respectively. Then, the equation (3.2) can be expressed by:

$$H(\overrightarrow{r},\overrightarrow{R}) = \sum_i \frac{-\hbar^2}{2m}\nabla_i^2 - \frac{1}{2}\sum_{i=j}\frac{e^2}{|r_i - r_j|} + \frac{e^2}{2}\sum_{k\neq l}\frac{Z_k Z_l}{|R_k - R_l|} - e^2\sum_{i,k}\frac{Z_k}{|r_i - R_k|} \tag{3.4}$$

where $\hbar$ is the Planck constant. Despite its seemingly straightforward formulation, the many-electron Hamiltonian poses formidable challenges in practical calculations due to the intricate interplay of electronic correlations, exchange effects, and quantum confinement. In particular, the electron-electron interaction term presents a formidable obstacle, as it leads to the emergence of complex many-body phenomena such as correlation effects, screening, and collective excitations.

Addressing the many-particle problem in first-principles calculations requires the development of sophisticated theoretical frameworks and computational methodologies capable of accurately capturing the electronic structure and dynamics of materials. While exact solutions for simple

Hamiltonians like the particle in a box or single electron systems are achievable, devising a generalized method to solve an N-electron Hamiltonian and derive an anti-symmetric wave function Ψ proves challenging. In the early stage, the Hartree approximation [95], which is a fundamental approach in quantum mechanics, was used to solve the N-electron Hamiltonian for atoms and molecules by simplifying the complex problem of electron-electron interactions by treating each electron as moving independently within an average potential generated by the other electrons. In this method, the wave function Ψ of the entire system is approximated as a product of single-electron wave functions, with each electron moving in a mean field generated by the other electrons and the atomic nuclei, and Ψ can be represented by:

$$\Psi(r_1, r_2, ..., r_N) = \psi_1(r_1) \times \psi_2(r_2) \times ... \times \psi_N(r_N) \tag{3.5}$$

where ψ_i represents the wave function of the i-th electron. Despite its simplicity, the Hartree approximation has several limitations and disadvantages. First, it neglects electron correlation effects, which are crucial for accurately describing the behavior of electrons in atoms and molecules. Secondly, the iterative process for determining the mean field potential generated by the electrons can be computationally intensive and may converge slowly, particularly for systems with strong electron-electron interactions. Next, this method violates the Pauli exclusion principle, which states that no two electrons in an atom can occupy the same quantum state simultaneously. In this method, each electron moves in an independent mean field potential, leading to incorrect predictions for electron-electron interactions. Moreover, this approximation method does not adequately account for exchange effects which lead to the stabilization of electronic states and play a crucial role in determining the structure and properties of atoms and molecules. This is due to the quantum mechanical indistinguishability of electrons. The Hartree approximation provides a useful starting point for solving the N-electron Hamiltonian and offers important assumptions and conjectures. The Hartree-Fock approximation [96], on the other hand, improves upon the Hartree approximation by incorporating the antisymmetry principle of quantum mechanics. It constructs a single Slater determinant wave function for the

N-electron system, known as the Hartree-Fock wave function, by:

$$\Psi(r_1, r_2, ..., r_N) = \begin{Vmatrix} \psi_1(r_1) & \psi_1(r_2) & \dots & \psi_1(r_N) \\ \psi_2(r_1) & \psi_2(r_2) & \dots & \psi_2(r_N) \\ \vdots & \vdots & \ddots & \vdots \\ \psi_N(r_1) & \psi_N(r_2) & \dots & \psi_N(r_N) \end{Vmatrix} \tag{3.6}$$

which is antisymmetrized with respect to the electron coordinates. This allows the Hartree-Fock method to better account for electron correlation effects and provides a more accurate description for many-electron systems especially small molecules compared to the Hartree approximation. However, this method treats electrons as independent particles and neglects significant electron correlations such as Coulomb interaction in metal and solid systems, leading to inaccuracies in determining the stable state and total energy of these strongly correlated systems. In addition, some other methods such as configuration interaction (CI) [97] and coupled cluster (CC) theory [98] were explored to account for the electron correlation effects in solving the many-particle systems, whereas each method has its disadvantages and limitations.

3.2.2 Density functional theory

To simplify the problem, the Born-Oppenheimer approximation [99] was proposed to describe the electronic structure of many-electron systems while keeping the positions of atomic nuclei fixed. This approximation is based on the fact that the mass of the nuclei is much larger than that of the electrons, leading to a separation of timescales between electronic and nuclear motion. Consequently, the electronic configuration can be treated as instantaneous compared to the much slower motion of the nuclei. This approximation considers the contribution of nuclei to the total energy of the system to be constant, while the electrons in the external field affect the interactions between ions and electrons, thereby determining the total energy of the system. Based on this approximation, density functional theory (DFT) was proposed by Hohenberg, Kohn and Sham [100, 101] to solve the many-electron problem by replacing it with one-electron Schrödinger

equations. The density in DFT indicates the electron density $\rho(r)$ which can represent the wave function Ψ by:

$$\rho(r) = \int |\Psi(r_1, r_2, ..., r_N)|^2 \, dr_1 dr_2 ... dr_N \tag{3.7}$$

In order to obtain the ground-state energy of a many electron system, The Rayleigh-Ritz variational principle [102] states that for any trial wave function belonging to a certain Hilbert space, the expectation value of the Hamiltonian is always greater than or equal to the ground-state energy of the system E_0:

$$E_0 \leq E[\rho] = \frac{\langle \Psi | H | \Psi \rangle}{\langle \Psi \mid \Psi \rangle} \tag{3.8}$$

Therefore, the ground-state energy of the system E_0 can be approached by minimizing the expectation value of the Hamiltonian. In the (3.8), the energy functional of the electron density $E[\rho]$ comprises of the contributions from electrons ($F[\rho]$) and external potentials, which can be expressed as:

$$E[\rho] = F[\rho] + \int \rho(r) V_{ext} dr \tag{3.9}$$

The external potentials V_{ext} include all the external factors except for electron-electron interactions, namely nuclei-electron interaction and other potential factors that affect the electron density. The functional of electron potentials $F[\rho]$ can be separated into three terms as:

$$F[\rho] = T_S[\rho] + E_H[\rho] + E_{XC}[\rho] \tag{3.10}$$

where $T_S[\rho]$ represents the kinetic energy contribution, T and S denote the operator and entropy of the electron density ρ. $E_H[\rho]$ is the Hartree energy contribution arising from the Coulomb repulsion between electrons. $E_{XC}[\rho]$ is exchange-correlation energy contribution which accounts for the effects of electron-electron correlation and exchange. The exchange term describes the antisymmetry of the wave function when two electrons are exchanged, while the correlation term accounts for the interactions beyond the mean-field approximation. By reworking the original many body Hamiltonian, the Kohn-Sham equation maps the many-body problem onto a set of

non-interacting single-particle equations, which is given by:

$$\left(\frac{-\hbar^2}{2m}\nabla^2 + V_{eff}(r)\right)\phi_i(r) = \varepsilon_i\phi_i(r) \tag{3.11}$$

where $\phi_i(r)$ are the Kohn-Sham orbitals which can be represented by $\rho(r) = \sum_i^N |\phi_i(r)|^2$, ε_i are the corresponding eigenvalues (orbital energies), $V_{eff}(r)$ is the effective potential that can be decomposed into:

$$V_{eff}(r) = V_{ext}(r) + V_H(r) + V_{XC}(r) \tag{3.12}$$

where $V_{ext}(r)$ is the external potential, $V_H(r)$ is the Hartree potential arising from electron-electron repulsion and can be written as:

$$V_H(r) = \int \frac{e^2 n(\vec{r}\,')}{|\vec{r} - \vec{r}\,'|} d^3r' \tag{3.13}$$

The exchange correlation potential $V_{XC}(r)$ is derived from the exchange correlation energy $E_{XC}[n(r)]$ which is a functional of the electron density $n(r)$, it can be expressed by:

$$V_{XC}[n(r)] = \frac{\delta E_{XC}[n(r)]}{\delta n(r)} \tag{3.14}$$

This functional approximates the unknown exchange correlation energy, which accounts for the effects of electron correlation beyond the classical Coulomb repulsion. The complexity of these interactions makes it challenging to describe them analytically, necessitating the use of approximation methods. Nevertheless, several approximations [103] are available to evaluate the exchange correlation energy for specific systems, each with its own approach and level of sophistication. A common approach is local density approximation (LDA) [104] which is the earliest and simplest method. It assumes that the exchange correlation energy per particle at a given point in space depends only on the local electron density at that point. It can be described by:

$$E_{XC}^{LDA}[n(r)] = \int \varepsilon_{XC}(n) n(r) d^3r \tag{3.15}$$

where $\varepsilon_{XC}[n(r)]$ is the exchange correlation energy density and is typically obtained from the known exchange-correlation energy of the homogeneous electron gas. Another method, the generalized gradient approximation (GGA) [105–107] extends LDA by incorporating information about the gradient of the electron density. This method assumes that the exchange correlation energy depends not only on the local electron density but also on its gradient:

$$E_{XC}^{GGA}[n(r)] = \int \varepsilon_{XC}[n(r), \nabla n] n(r) d^3r \tag{3.16}$$

the $\varepsilon_{XC}[n(r), \nabla n]$ is expressed as a functional of the electron density and its gradient. For this method, some parameterizations were developed to increase the accuracy of the approximation (e.g. PBE [108]). The latest method hybrid functionals (HF) [109] combine the advantages of both Hartree-Fock theory and DFT by mixing exact exchange with DFT exchange correlation functionals, which can be expressed as:

$$E_{XC}^{hybrid}[n(r)] = aE_X^{exact}[n(r)] + (1-a)E_X^{DFT}[n(r)] + E_C^{DFT}[n(r)] \tag{3.17}$$

This functional includes a fraction a of exact exchange energy E_X^{exact}, mixed with DFT exchange E_X^{DFT} and correlation E_C^{DFT} energies. While this method can offer improved accuracy by including a fraction of exact exchange energy, this enhancement comes at the expense of higher computational resources and longer calculation times. Additionally, the choice of the mixing parameter a can be somewhat arbitrary, and the performance of the functional may vary depending on its value.

In reality, the computational cost of explicitly treating core electrons in electronic structure calculations can be prohibitively high, especially for systems with many atoms or electrons. It is well-known that core electrons are tightly bound to the atomic nucleus and have little effect on chemical bonding or electronic properties beyond a certain distance from the nucleus as bonding and cohesion in the system predominantly arise from the overlap of valence electrons between atoms [110, 111]. Therefore, to further simplify the electron-electron interactions, it is

necessary to develop a model or method to coarse graining the contributions from core electrons. In the context of the above, the pseudopotential method [112] was developed to replace the core electrons with an effective potential that approximates the interaction between valence electrons and the atomic nucleus, as well as the screening effects of the core electrons. This effective potential is constructed to reproduce the combined influence of the core electrons and nuclei, making it possible to describe valence electrons using a pseudo-wave function with fewer nodes. That means the wave function can be written with fewer Fourier series terms, which makes the calculation of the plane wave basis set practical. The diagram that pseudopotential represents the true potential is shown in Figure 3.3. When $r > r_c$, the pseudopotential, true potential, and pseudo-wave function largely overlap, sharing the same shape and amplitude. However, when $r < r_c$, the pseudopotential and true potential exhibit more noticeable discrepancy, while the deviation between the pseudopotential wave function and the true wave function is relatively small. The sharply changing true wave function is transformed into a slowly changing pseudo-wave function, thereby achieving the pseudopotential conservation [113].

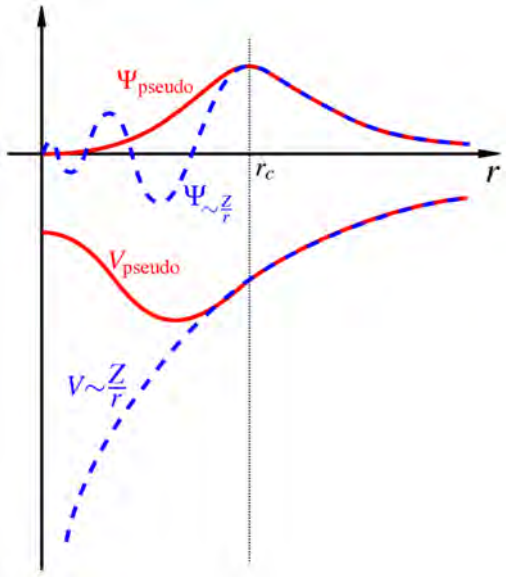

Figure 3.3: Pseudopotential wave function (red lines) and all electron wave function (blue dashed lines) [113].

There are several types of pseudopotentials, including norm-conserving pseudopotentials [114], ultrasoft pseudopotentials [115], and projector-augmented wave (PAW) pseudopotentials [116], each with its own characteristics and applications. In this dissertation, the PAW method was

employed to approximate the plane wave function, which combines the simplicity of a first-principles pseudopotential method and the accuracy of all-electron methods. This method starts by constructing localized projector functions centered around each atomic nucleus [116, 117]. These projector functions are designed to capture the behavior of the core electrons within a specified cutoff radius. Pseudo-wave functions are then constructed by combining the projector functions with pseudo-wave functions, which represent the valence electrons. The pseudo-wave functions are chosen to be smooth and well-behaved functions that accurately describe the valence electron behavior. Once the projector τ and these smooth pseudo-wave functions $\tilde{\phi}$ are constructed, a linear transformation is performed to express the all-electron pseudo-wave functions in terms of the basis of projector functions by:

$$\phi_k = \tau\tilde{\phi} \tag{3.18}$$

This transformation effectively projects the pseudo-wave functions onto the space spanned by the projector functions. The linear transformation yields expansion coefficients that represent the contribution of each projector function to the pseudo-wave function. These expansion coefficients determine how much each projector function contributes to the representation of the valence electron behavior, and then are used to construct the one-electron Kohn-Sham equation. The potentials constructed using the PAW-PBE method in the Vienna Ab initio Simulation Package (VASP) [115, 118–121] were used to carry out all the DFT calculations in this work. An important parameter in the potentials in VASP is energy cutoff (E_{cut}) which determines the size of the plane-wave basis set in the DFT calculations. All the electron density is represented as a summation of planar waves:

$$\rho(r) = \sum_G \rho_G e^{iGr} \tag{3.19}$$

Plane waves (G) with energies below the cutoff energy are used in the DFT calculations. A higher E_{cut} can lead to more precise total energy while increasing the time and computation expense. Another crucial setting is the discretization of the Brillouin zone, known as k-points, which is a mathematical construct representing the electron momentum space in a crystalline

solid. The choice of k-points determines the resolution with which electronic states are sampled in reciprocal space. More k-points provide a finer sampling, leading to more accurate results, but increasing the computation time. In this study, to ensure calculation accuracy without increasing unnecessary computation time, all parameters subjected to convergence testing were verified for convergence according to different systems. The other DFT settings are also described at the beginning of each chapter.

3.3 Cluster expansion Formalism

The computation of the thermodynamic quantities of an alloy from DFT calculations generally involves three steps. First, the partition function of the system undergoes a coarse-graining transformation to that of a lattice model, which effectively captures the potential configurational disorder of the alloy [69]. Second, the resultant coarse-grained partition function encompasses a summation over all feasible arrangements of atoms on a given parent lattice. Finally, the system undergoes thermal equilibration, and free energies over compositions and temperatures are derived through Monte Carlo simulations [122]. In the second step, due to the immense number of terms in this summation, computing the energy of each configuration from first principles is unfeasible. Therefore, it is crucial to find a method that can evaluate the energy of any configuration of the system based on a portion of the known configuration energies.

The cluster expansion formalism, a generalized Ising model, can parametrize the energy's dependence on alloy configuration. This technique offers a concise representation of the configurational energy dependence, with the accuracy being progressively enhanced by incorporating a sufficient number of terms in the expansion. In this method, the energy of a configuration is linked to the interactions among atoms within small clusters. The ground states at 0 K in the system can be determined by the construction of cluster expansion of the 0 K DFT energies and then can be used with the crucial clusters and cluster interactions as a Hamiltonian to perform Monte Carlo simulations to get their free energy over compositions and temperatures. In this

study, the alloy theoretic automated toolkit (ATAT) [62, 123, 124] was used to enumerate the structures, construct the cluster expansion, and fit it to data obtained from DFT calculations.

3.3.1 Clusters and basic functions

Any configuration within the system can be delineated by employing occupation variables associated with the lattice sites [60, 125]. For instance, in the hcp Ti-O system, the sites in the metal sublattice can only allow Ti atoms to occupy, such that there is no degree of freedom on this sublattice. However, in the sublattice with octahedral sites, oxygen atoms and vacancies are both allowed to occupy these sites. Then, the occupational variable (σ_i) for a site i in the octahedral sublattice can be assigned 0 if it is occupied by a vacancy and 1 if an oxygen atom is present at this site, as shown in Figure 3.4. There is no need to assign occupational variables to the Ti sublattice due to no degree of freedom. Any arrangement of compositional Ti_xO_y in the Ti-O system thereby can be expressed by the occupation variable vector $\vec{\sigma} = [\sigma_1, \sigma_2, \ldots, \sigma_n]$ which collects the occupation variables of all the sites n in the oxygen-vacancy sublattice in Ti_xO_y.

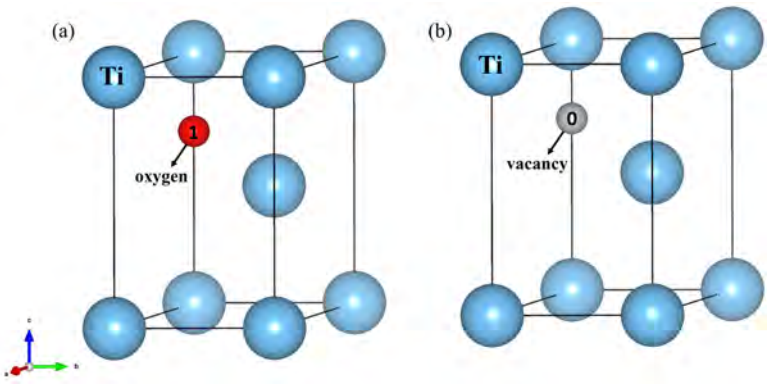

Figure 3.4: The representation of the occupational variables in the hcp Ti-O system.

While the local arrangement of the atoms at the sublattice can be represented by the occupation variable vector, the energy of a specific configuration is affected by the repulsive and attractive interactions between these atoms. For this purpose, the basis function representing site clusters can be employed. This basis function typically takes the form of polynomials of the occupation

variables in the cluster. Cluster refers to the grouping of certain sites within these sites with occupation variables [126, 127]. For example, two sites can group as a pair, three sites can form a triplet, and four sites can generate a quadruplet. Figure 3.5 illustrates the examples of the cluster formation of the pairs, triplets, and quadruplets on the x-y plane in the hcp Ti-O system. We can then get the basis function ϕ_α of a cluster α by the multiplication of all the occupation variables σ_i:

$$\phi_\alpha = \prod_{i \in \alpha} \sigma_i \tag{3.20}$$

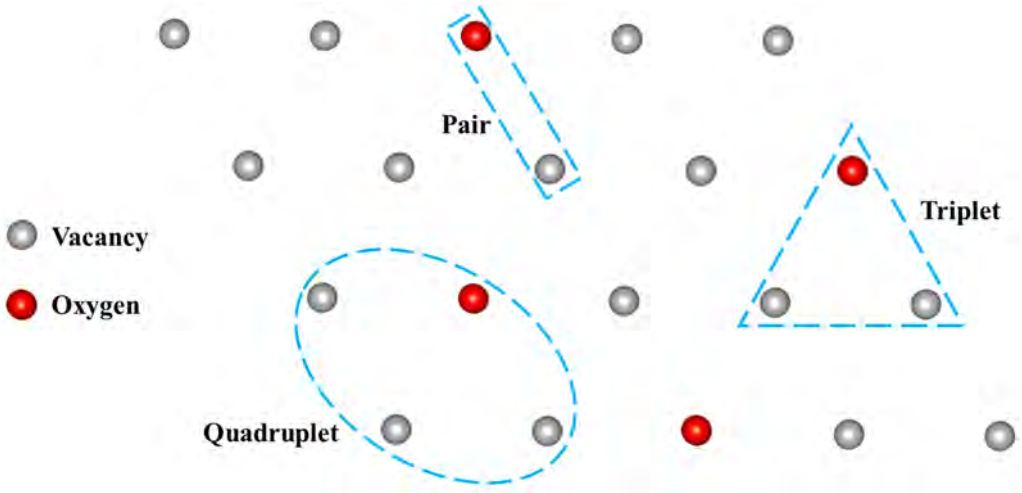

Figure 3.5: Examples of the clusters in the hcp Ti-O system: pair, triplet, and quadruplet.

If all the clusters are taken into account, the basis functions can constitute a comprehensive orthogonal basis set across the whole configuration space. Then, cluster expansion can express the energy of any configuration in the system by considering the interactions of all the clusters and their associated basis functions as [62, 128, 129]:

$$E(\vec{\sigma}) = \sum_{\alpha} \phi_\alpha J_\alpha(\vec{\sigma}) \tag{3.21}$$

where J_α represents the effective cluster interactions (ECI) of cluster α which is a crucial parameter in the cluster expansion method. It can be treated as a coefficient that embodies the contribution of the interactions between the species in a cluster to the energy of the configuration.

In theory, as the number of enumerated configurations increases, the number of clusters grows

exponentially, making it impractical to capture all clusters. This implies that it is necessary to truncate the clusters reasonably while ensuring cluster accuracy [130]. When capturing clusters, limiting the cluster radius or the number of clusters can be considered feasible as it has been observed from DFT calculations that the correlations between species within clusters become very weak, gradually approaching zero, when the distance between species in the cluster is beyond a certain value [122, 131]. Therefore, this truncation method essentially limits the interaction distance between species within the clusters. In practice, it is found that the interaction between clusters generally converges rapidly. With 30-50 configuration energies obtained from DFT, about 10-20 clusters can accurately fit these DFT energies and well predict the energy of any configuration in a simple system. It should be noted that, in the process of structure enumeration, ATAT calculates the factor group which represents the symmetry of the primitive structure of the input crystal structure, then the symmetry operations in the factor group are applied to the primitive structures to enumerate symmetrically unique configurations [132]. These symmetry operations do not change the crystal structure and the energy of the system, thereby clusters mapped to each other through these factor groups have the same ECI. This makes it necessary to classify clusters with the same site positions and radius. All symmetric equivalent clusters can be regarded as a set Ω_α, here α denotes all the clusters that are equivalent to the cluster α through symmetry. Then, the cluster basis function (3.20) can be normalized as:

$$\langle \phi_\alpha(\vec{\sigma}) \rangle = \frac{\sum_{\beta \in \Omega_\alpha} \phi_\beta(\vec{\sigma})}{m_\alpha N_p} \tag{3.22}$$

where m_α represents the quantity of the clusters that are equivalent to the cluster α and N_p is the number of the primitive cells in the enumerated configuration. Therefore, the energy of the configuration can be described by reworking the equation (3.21) as follows:

$$E(\vec{\sigma}) = \sum_\alpha m_\alpha J_\alpha \langle \phi_\alpha(\vec{\sigma}) \rangle \tag{3.23}$$

3.3.2 Determination of effective cluster interactions (ECIs)

In the equation (3.23), an important parameter J_α (ECI), which reflects the strength of the interactions between the internal sites and embodies the information regarding the energetics of the system, needs to be determined. There are typically two ways to evaluate the ECIs. The first is by considering ordered structures as perturbations to the disordered structure. In this method, the disordered alloy is computed either using the Virtual Crystal Approximation (VCA) [133, 134] or the Coherent Potential Approximation (CPA) [135]. The second method, also known as Structure Inversion Method (SIM) or the Collony-Williams method [136], is by fitting ECIs to the energy of a relatively small number of configurations obtained through DFT computations. Both of these two methods were applied to numerous systems, however, the first method, as a perturbative approach, is tested to fail when applied to systems where there is a significant energy difference between the disordered and ordered phases. Additionally, due to the lack of information on atomic force, the CPA fails to capture the geometric relaxation of configurations. In contrast, the second method can be straightforward to evaluate the ECIs by performing DFT calculations on a number of known configurations. The *maps* and *mmaps* codes in ATAT [69] can help us sequentially enumerate configurations from small to large sizes and provide information about the crucial clusters and their correlations with these configurations. To obtain the values of ECIs by fitting clusters to the DFT energies of the enumerated configurations, we need to work on the following linear operation of matrices:

$$\mathbf{E}_{DFT} = \boldsymbol{\phi}\mathbf{J} \tag{3.24}$$

where $\mathbf{E}_{DFT}$ is the $m \times 1$ matrix consisting of the energies of all the m configurations, $\boldsymbol{\phi}$ is the $m \times n$ matrix consisting of the correlations between each configuration and the clusters, and $\mathbf{J}$ is the $n \times 1$ matrix consisting of ECIs of all the n clusters. While the values of ECIs can be obtained via equation (3.24), the selection of clusters can greatly affect the values of ECIs and the predictive power of the cluster expansion. The constructed cluster expansion model is not just used to predict DFT energies, but also employed to predict the energies of thousands of large-

size configurations in the subsequent Monte Carlo simulations. Performing DFT calculations on these large-size supercells is not feasible, thus finding a cluster model with good predictive power is crucial. In order to obtain a high-precision cluster expansion model with accurate and representative ECIs, the following three points need to be considered. First, it is essential to enumerate a diverse set of configurations that adequately span the entire compositional space of the system such that clusters can collect all the important interactions between species. Second, the choice of basis functions (i.e. clusters) should accurately capture the energetics of the system and account for important atomic arrangements in the configurations. The last is to validate the predictive power of the cluster expansion model by testing its performance on independent datasets not used in the fitting process. Regarding the first point, ATAT can initially enumerate representative configurations over wide compositions, then based on the calculated DFT energies of these configurations, continually enumerate important configurations until all ground states are found, and no new ground states can be predicted. For the second point, we can set an upper limit on the distance between the nearest neighbors in the clusters, such that ATAT only searches for important clusters within the given limit. We can also limit the number of selections for each type of cluster so that ATAT only searches the specified number of clusters for each type. However, for the final point, it is necessary to calculate the difference between the DFT energy and the CE predicted energy for each configuration, in order to calculate the cross-validation score and thereby evaluate the quality of cluster expansion. This step requires more manual intervention to minimize the score.

3.3.3 Cross-validation score

As mentioned above, to achieve a perfect cluster expansion model, theoretically an infinite number of clusters and configurations are required. However, to obtain a satisfactory high-precision cluster expansion model, it is sufficient to truncate both at an appropriate position, meaning that a number of clusters are fitted to a certain number of configuration energies. The challenge lies in determining how many configurations and clusters are needed for a given

system. On one hand, too few configurations may fail to adequately represent the entire system, while an excessive number of configurations increases computational costs and introduces more noise into the cluster expansion. On the other hand, for a selected set of configurations, too few clusters may result in the cluster expansion model being unable to accurately predict DFT energies, as the truncated clusters may fail to account for all sources of energy fluctuations. Conversely, if too many clusters are kept, the more subtle problem of overfitting manifests itself. This can lead to a situation where the fitting mean square error may appear seemingly small, whereas the true predictive capability of the cluster expansion for the energies not included in the fit is actually much lower. The essence of this problem is that the energy variations caused by the ECIs (J_β) of cluster set β, which are not included in the fit, may be incorrectly attributed to the ECIs (J_α) of another cluster set α that is included in the fit. Therefore, for a given set of DFT energies, it is needed to find the compromise between these two detrimental effects in order to obtain the most predictive cluster ensemble for ECIs. A reliable solution to this problem is the "Leave-one-out cross-validation" (LOOCV) method [137] which leaves one data point out during each iteration to simulate a scenario where the model is trained on a subset of the data and tested on the remaining data, allowing for an assessment of how well the model generalizes to unseen data. Applying LOOCV here, each energy point in the DFT dataset is left out once, and the cluster expansion model is trained on the remaining energy points. Then, the prediction of the model is evaluated based on the omitted energy point. This process is repeated for each energy point in the DFT dataset. LOOCV provides a robust estimate of the performance of the constructed cluster expansion model as it evaluates the model on all energy points in the DFT dataset. In addition, it not only does not require the random splitting of the DFT dataset, which can lead to variability in the evaluation results, but also maximizes the use of available energy dataset for both training and testing, especially in DFT datasets with a small number of energy points.

Based on the LOOCV method, the goodness of the fit of the cluster expansion can be clearly

quantified through the cross-validation (CV) score [122] (also presented in [131]):

$$CV = \sqrt{\frac{1}{n}\sum_{i=1}^{n}(E_i - E_{i(CE)})^2} \tag{3.25}$$

where n is the number of all the configurations used to fit the cluster expansion. E_i and $E_{i(CE)}$ indicate the DFT calculated energy of structure i and CE predicted energy obtained from a least-squares fit to the $n-1$ other calculated energies, respectively. Similar to the root-mean-square error, the CV score, which is sensitive to outliers, averages deviations between DFT energies and CE predicted energies on all configurations. A smaller CV score in most cases indicates a highly accurate and predictive CE, which is different from the well-known mean square error. As shown in Figure 3.6, the CV score first decreases as more degrees of freedom (more clusters) are available to account for the variations in energy. After the CV score reaches its minimum, overfitting occurs, where an increase in noise in the ECIs happens, which in turn causes the CV score to gradually increase. Hence, the selection of the clusters corresponding to the minimum CV score provides the optimal and most predictive ECIs. Assessing the accuracy of a constructed cluster expansion model entails predicting another validation set. It is noteworthy that a key feature of the CV equation is its simplicity to operate by removing one point at a time from the dataset, without necessitating multiple splits. Additionally, while certain points are excluded from the fit when operating the CV equation, the resulting CV score can also reflect the predictive capability of the cluster expansion model with the inclusion of all points.

3.4 Noise identification and removal in the cluster expansion

For a given energy dataset, we can always find the optimal solution by optimizing the radius or number of clusters, obtaining the minimum CV score. However, for some systems, especially those containing elements with different crystal structures, the optimal solution of the CV score may be unsatisfactory. This results in the constructed cluster expansion model being unable to accurately predict energies in the dataset. The underlying reason for this phenomenon is

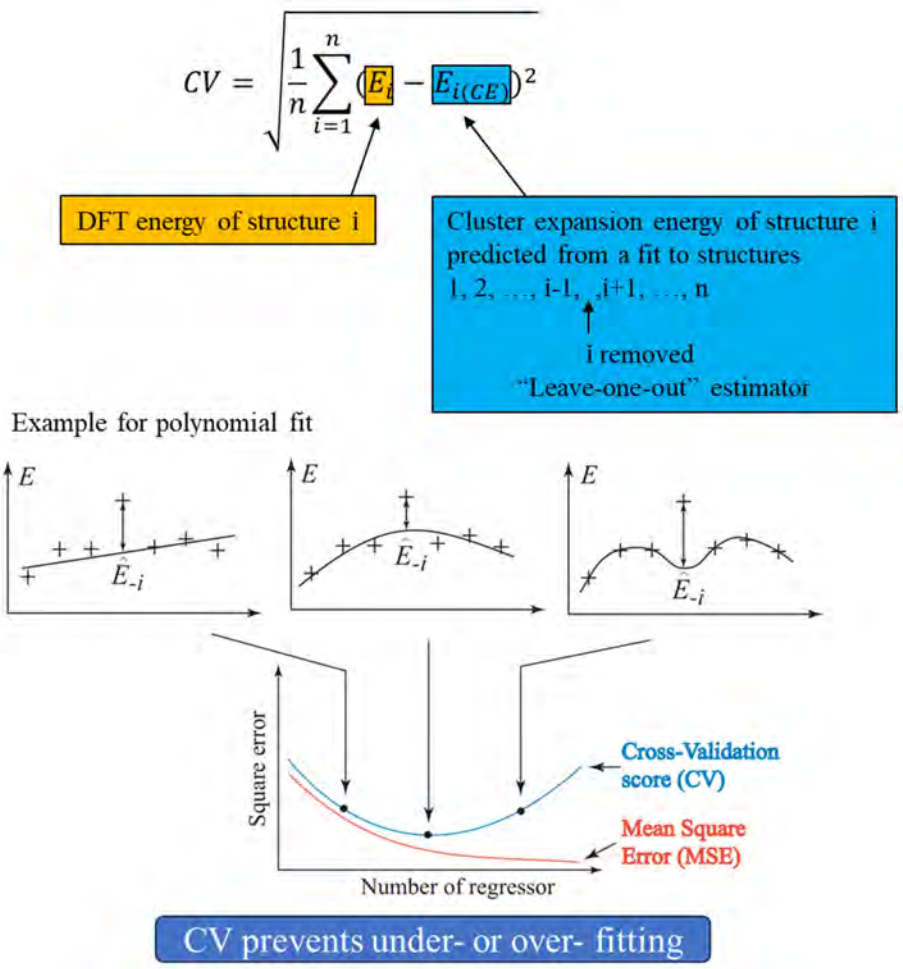

Figure 3.6: Working mechanism of the CV score.

not the inadequacy of the cluster expansion fit but rather the presence of noise in the energy dataset, which cannot be eliminated by optimizing the cluster expansion model. The source of this noise is certain configurations in the configuration set that become highly distorted after fully relaxation through DFT calculations, with some configurations even relaxing to other geometries. Therefore, these highly distorted configurations should not be included in the cluster expansion fit of the system. They should be accurately identified and removed from the configuration set. Only in this way can the blocked CV score be better optimized, resulting in a predictive cluster expansion model.

An important method to analyze the crystal geometry of a configuration is common neighbor analysis (CNA) [138]. The mechanism of CNA involves examining the coordination environ-

ments of individual atoms in a crystal lattice by analyzing their neighboring atoms and the types of bonds formed between them. This analysis is based on the idea that atoms in a crystal lattice tend to arrange themselves in regular and repeating patterns, with certain coordination numbers and bond angles characteristic of specific crystal structures. The CNA algorithm employed in this work involves three steps. The first is to identify the nearest neighbors of each atom in each configuration based on a specified cutoff radius. Then, CNA determines the types of bonds formed between each atom and its nearest neighbors, and it analyzes bond lengths, bond angles, and the coordination number of each atom. Last, the local atomic environments of each atom based on the types of bonds formed with its nearest neighbors are classified. This classification method includes distinguishing between different crystal structures and identifying defects or interfaces within the configuration. Figure 3.7 shows the coordination number and the specific arrangement of atoms in the local environment of fcc, hcp, icosahedral, and bcc crystal structures [139]. Sometimes an appropriate cutoff cannot be found using conventional CNA, in this case, we use the more advanced interval CNA (i-CNA) method [140] to investigate all possible threshold choices for each atom, which provides a better recognition rate.

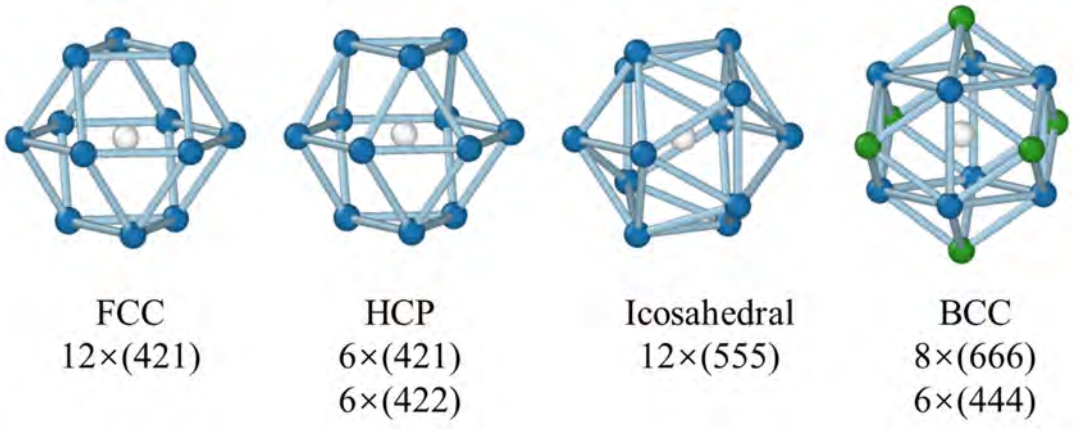

Figure 3.7: Coordination number of fcc, hcp, icosahedral, and bcc crystal structure [139].

While the CNA method can identify all configurations that do not keep the parent lattice of the system, there may still be some highly distorted configurations in the system that have not relaxed to other crystal structures. For such configurations, CNA is ineffective since they still maintain the crystal structure type of the parent lattice of the system. Therefore, it is necessary to compute the relaxation amount (RA) for each configuration after relaxation. In this study,

the *checkrelax* command in ATAT [123] (also presented in [131]) was employed to calculate the distortion for each configuration, representing the RA. The distortion of a configuration is measured by:

$$RA = \left\| \frac{\mathbf{D}+\mathbf{D}^T}{2} - \mathbf{I} \right\|_F \tag{3.26}$$

where $\mathbf{I}$ and F denote the identity matrix and the Frobenius norm, respectively. $\mathbf{D}$ refers to the matrix that represents the distortion between the original and relaxed configuration, and it can be derived from:

$$\mathbf{D} = \left(\frac{\mathbf{A}}{(det\mathbf{A})^{1/3}} \right)^{-1} \times \frac{\mathbf{B}}{(det\mathbf{B})^{1/3}} \tag{3.27}$$

here $\mathbf{A}$ and $\mathbf{B}$ are the matrix composed of lattice vectors of the configurations before and after relaxation, respectively. In general, for a simple binary system, RA>0.1 is considered too much for distortion, and those offending configurations should be disabled to construct cluster expansion [141].

By applying CNA method and RA calculation to all the enumerated configurations, all the noises can be identified and removed from the cluster expansion, thereby lowering the blocked CV score reasonably by selecting appropriate clusters.

3.5 Vibrational free energy and other thermodynamic properties

(The work presented in this section is adapted from [131])

To accurately extend the thermodynamic properties of different configurations and phases at 0 K to finite temperatures, besides the 0 K configuration energy, magnetic free energy, electronic free energy, and vibrational free energy caused by lattice thermal expansion also should be considered. Magnetic properties and electronic free energy are not discussed in this dissertation since, for metallic systems, the electronic energy is generally several orders of magnitude smaller than the configuration energy, and no previous literature reported that magnetism exists in any

Ti-O and Ti-Nb compounds. Unlike the effect of magnetism and electrons, vibrational free energy (F_{vib}) exists in any system as thermal expansion happens in crystal lattices even at lower temperatures. Furthermore, as the temperature increases, F_{vib} contribution to the total free energy may be significant because, as the primary contribution to the F_{vib}, vibrational entropy (S_{vib}) is positively correlated with temperature. Therefore, computing and discussing the vibrational free energy of configurations are crucial for correctly understanding the stability of various phases at different temperatures.

Many thermodynamic models have been developed to account for the vibrational degrees of freedom in solids with different precision. Here, the widely-applied Debye-Grüneisen model [142, 143], implemented in the Gibbs2 package [144, 145], was employed to estimate the F_{vib} for those relaxed structures close to convex hull over the whole composition region. These data then was used to fit another CE for F_{vib} to obtain vibrational ECIs. In the Debye-Grüneisen model, the lattice vibrational properties are described using the Debye model, which assumes that the vibrational modes of the crystal can be treated as sound waves propagating through an elastic medium. These modes are characterized by a maximum frequency known as the Debye frequency. The Grüneisen parameter accounts for deviations from the harmonic behavior assumed by the Debye model, capturing the effects of anharmonicity and thermal expansion on the lattice vibrations. Within this framework, the volume- and temperature-dependent F_{vib} of a configuration can be calculated by:

$$F_{vib} = \frac{9}{8} n k_B \Theta_D + 3 n k_B T \ln(1 - e^{-\Theta_D/T}) - n k_B T D(\Theta_D/T) \tag{3.28}$$

where n is the number of atoms in primitive cell, k_B the Boltzmann's constant and D the Debye function given by:

$$D(x) = \frac{3}{x^3} \int_0^x \frac{y^3 e^{-y}}{1 - e^{-y}} dy \tag{3.29}$$

and Θ_D denotes the Debye temperature calculated at the static equilibrium volume V_0 by [142]:

$$\Theta_D(V) = \Theta_D(V_0) \cdot \left(\frac{V_0}{V}\right)^{\gamma} \tag{3.30}$$

where γ is the Grüneisen parameter, which can be obtained by [146]:

$$\gamma = a + b\frac{dB_{sta}}{dp} = a - b\frac{d\ln B_{sta}}{d\ln V} \tag{3.31}$$

where B_{sta} is the static bulk modulus, factor a and b can be approximated using the expression by Slater ($a = -1/6, b = 1/2$) [147], Dugdale-McDonald ($a = -1/2, b = 1/2$) [148], Vaschenko-Zubarev ($a = -5/6, b = 1/2$) [149] and the mean free volume gamma ($a = -0.95, b = 1/2$) [150]. There is little difference when testing each of the above expressions in this study, we adapt in the value of $a = -5/6$, $b = 1/2$. The $\Theta_D(V_0)$ can be expressed by:

$$\Theta_D(V_0) = \frac{1}{k_B}(6\pi^2 V_0^{1/2} n)^{1/3} f(\sigma)\sqrt{\frac{B_{sta}}{M}} \tag{3.32}$$

where M is the molecular mass of the primitive cell and σ the Poisson ratio at equilibrium state. The function $f(\sigma)$ can be represented by:

$$f(\sigma) = \left\{3\left[2\left(\frac{2(1+\sigma)}{3(1-2\sigma)}\right)^{3/2} + \left(\frac{(1+\sigma)}{3(1-\sigma)}\right)^{3/2}\right]^{-1}\right\}^{1/3} \tag{3.33}$$

Other thermodynamic properties of a configuration can be derived directly from the Helmholtz free energy, obtained from the configurational and vibrational free energies, according to the following equation:

$$F(V; p, T) = F_{config}(V) + pV + F_{vib}(V; T) \tag{3.34}$$

In order to calculate the free energy of phases as a function of composition and temperature with the inclusion of vibrational entropy, the temperature-dependent ECIs obtained by summing up ECIs calculated from CE of configurational and vibrational free energies respectively were used as input (Hamiltonian) in Monte Carlo simulations.

3.6 Thermodynamic averaging of the investigated systems

Through constructing the CE model for a system, we obtained valuable ECIs that capture all types of interactions in the system and thereby represent the energetics of the system. These ECIs derived from the CE model can be used to extract the thermodynamic properties of various phases over the composition space and temperatures by thermodynamic averaging methods such as statistical sampling. The implementation of this is based on the physical fact that, when the system is in equilibrium, the macroscopic properties of the system can be described by ensemble averages which represent the average behavior of a large number of microscopic configurations of the system [151]. These microscopic configurations correspond to any microstate that the system may achieve. And as the temperature increases, the system fluctuates between different microstates. The probability of finding a system in a particular microscopic state i (P_i) can be evaluated by the Boltzmann distribution via:

$$P_i = \frac{1}{Z} \exp\left(-\frac{\Omega_i}{k_B T}\right) \tag{3.35}$$

where k_B and T are the Boltzmann's constant and temperature, respectively. Ω_i is the potential of state i in a specific ensemble. Z is the partition function, which ensures that the probabilities sum up to 1 over all possible states, can be given by:

$$Z = \sum_i \exp\left(-\frac{\Omega_i}{k_B T}\right) \tag{3.36}$$

Then the ensemble average of an observable thermodynamic quantity can be calculated by averaging the values of it over all the states of the system, weighted by the probability of each state. For instance, the average energy of the system can be computed by:

$$E = \sum_i P_i E_i \tag{3.37}$$

By averaging over many such states according to their probabilities, ensemble averages offer insights into the thermodynamic properties and allow predictions of macroscopic observables.

3.6.1 Semi-grand canonical Monte Carlo

To obtain the free energy at finite temperatures and establish phase stability for a system, it is necessary to perform Monte Carlo simulations that sample semi-grand canonical ensembles (SGMC) [152]. In this ensemble, the total number of atoms is fixed, while the externally imposed temperature and chemical potential are allowed to vary. A single-phase equilibria, free of interfaces, is ensured when the system achieves an equilibrium state. Additionally, it simplifies the computation of free energies by thermodynamic integration. The algorithm underlying the SGMC includes four steps. First, potential moves are randomly selected, such as trial potential changes, from a predefined probability distribution. The change in potential caused by the move from microstate i_A to i_B can be calculated by:

$$\Delta\Omega_{A\rightarrow B} = \Omega(i_A) - \Omega(i_B) \tag{3.38}$$

Then, according to the Metropolis criterion [153], the potential move is always accepted if $\Delta\Omega_{A\rightarrow B} < 0$, which means $P_{A\rightarrow B} = 1$. If $\Delta\Omega_{A\rightarrow B} > 0$, the move only can be accepted with the probability:

$$P_{A\rightarrow B} = exp(-\frac{\Delta\Omega_{A\rightarrow B}}{k_B T}) \tag{3.39}$$

Next, the previous two steps are repeated for a large number of iterations, allowing the system to equilibrate and sample configurations according to the semi-grand canonical ensemble. Finally, the sampled configurations are analyzed to calculate relevant properties of interest.

3.6.2 Thermodynamic integration of free energy

The Gibbs free energy, which can be calculated through the thermodynamic averaging from the semi-grand canonical Monte Carlo simulations, is represented by:

$$G = U - TS + PV \tag{3.40}$$

where U and S refer to the internal energy and entropy of the system, respectively. DFT calculations are performed at zero pressure, thus the PV term can be ignored.

The partition function of the system can be used to express the semi-grand canonical thermodynamic potential ϕ by [69, 154]:

$$\phi(\beta, \mu) = -\frac{1}{\beta N} \ln \left(\sum_i \exp(-\beta N(U_i - \mu x_i)) \right) \tag{3.41}$$

where $\beta = 1/(k_B T)$, U_i and x_i are the internal energy and the concentration at a certain state i, respectively. The Helmholtz free energy F can then be calculated via $F = \phi + \mu x$. The thermodynamic potential ϕ can also be written in differential form:

$$d(\beta\phi) = (U - \mu x)d\beta - \beta x d\mu \tag{3.42}$$

here, U and x are the average values of the system. The thermodynamic potential $\phi(\beta, \mu)$ can be obtained by thermodynamic integration according the (3.42) by:

$$\beta_1\phi(\beta_1, \mu_1) = \beta_0\phi(\beta_0, \mu_0) + \int_{\beta_0,\mu_0}^{\beta_1,\mu_1} (U - \mu x, -\beta x)d(\beta, \mu) \tag{3.43}$$

The integral is conducted along a continuous trajectory connecting points β_0, μ_0 and β_1, μ_1 without encountering a phase transition. For any given T and μ, the internal energy U and composition x of the system can be evaluated by the semi-grand canonical Monte Carlo simulations. The advantage of the integration technique is that the property is expressed as the thermody-

namic averaging of computationally inexpensive quantities, implying that the properties of the interested phases are directly reflected by the calculated quantities. In this study, the semi-grand canonical Monte Carlo simulation implemented in $emc2$ and $memc2$ code [62] were performed to get the thermodynamic averages for the binary and ternary systems, respectively.

Chapter 4

Hcp Ti-O system

(The work presented in this chapter is adapted from [131])

The DFT-based first-principles calculations implemented in Vienna Ab-initio Simulation Package (VASP) [115, 118–121] were performed to calculate the electronic structure and total energies of all the structures. The *maps* code in alloy theoretic automated toolkit (ATAT) [62] was used to enumerate the structures, construct the cluster expansion and fit the DFT energies. For the hcp Ti-O system, various configurations containing no more than 6 hcp Ti unit cells with oxygen vacancy random ordering over the octahedral sites were enumerated. The input lattice constants to enumerate the configurations are a = 2.9508 Å and c = 4.6855 Å. It should be noted that, in the configuration enumeration process, the symmetry operations performed in the factor group calculated by ATAT ensure that all the enumerated configurations are unique in terms of symmetry [132]. The *emc*2 code in ATAT was used to perform Monte Carlo simulations using the cluster expansion Hamiltonians via scanning chemical potential range and temperatures specified.

All the DFT calculations are performed using the projector augmented-wave (PAW) method as implemented in VASP. The exchange-correlation functional was described by the generalized gradient approximation parametrised by Perdew-Burke-Ernzerhof (PBE) [108]. The PAW potentials of Ti_sv with 12 valence electrons and O with 6 valence electrons, recommended in the

VASP manual, were used to treat valence states. Energy cutoff of 550 eV and 5000 k-points per reciprocal atom were used which were tested as sufficiently large to have a good calculation convergence for all the hcp Ti-O structures, achieving convergence to 1 meV or lower. For each structure, all the degrees-of-freedom were first allowed to relax (i.e. full relaxation) with ions relaxing using a conjugate-gradient algorithm, followed by a static calculation with reaching the structural convergence criteria, ensuring residual forces on each atom are below 0.02 eV/Å. All electronic self-consistent loops were stopped when the difference in total energy between subsequent iterations dropped below 10^{-6} eV. The second-order Methfessel-Paxton scheme [155] with the smearing width of 0.1 eV was used to treat the partial occupancy for relaxation calculations, meanwhile the tetrahedron method with Blöchl corrections [156] was employed for static calculations. No previous paper reported that magnetism exists in any Ti-O compounds, therefore all the calculations were performed with non-spin polarization.

4.1 Ground-states characteristics

A total of 365 configurations were enumerated over the whole oxygen concentration range to search the ground states and obtain a predictive CE model. All of these fully relaxed structures remain hcp, as confirmed using the common neighbor analysis (conventional, adaptive and interval CNA), which reflects that the oxygen stabilizes the α phases in Ti. After obtaining the total energy of each configuration, directly comparing the total energy is not scientific since the size of each configuration may be several times that of the initial hcp unit cell, and the number of atoms contained in each configuration is different. Therefore, it is necessary to normalize the calculated total energy in order to compare the stability of all the enumerated configurations. Here, the pure αTi and αTiO, where the octahedral sites are totally vacant and occupied in full, respectively, are treated as the reference states to normalize the total energy of each configuration. Then, we can define the formation energy (E_f) for each configuration,

relative to a mechanical mixture of αTi + αTiO, by:

$$E_f = \frac{E_{tot} - xE_{\alpha Ti} - yE_{\alpha TiO}}{x + y} \tag{4.1}$$

where E_{tot} is the total energy of the configuration $\alpha Ti_{x+y}O_y$ which has x vacancies and y oxygen atoms. $E_{\alpha Ti}$ and $E_{\alpha TiO}$ are the total energy per chemical formula of the pure αTi and αTiO. E_f of a configuration describes the energy difference between this configuration and the reference states. Therefore, the E_f of the two endpoints $E_{\alpha Ti}$ and $E_{\alpha TiO}$ are zero, and any E_f above zero are energetically unfavorable. If connecting the lowest E_f points of each component in sequence, we can obtain a convex hull, in which all energetically metastable and stable configurations should fall. Configurations lying on the convex hull line correspond to the most stable configurations (lowest E_f) for each composition and are referred to as ground states. The DFT calculated E_f of all the enumerated configurations are plotted in Figure 4.1, and the O concentration in the oxygen-vacancy sublattice is taken as the x-axis (i.e. $X_O = N_O/N_{Ti}$) since it is convenient to observe the difference on the oxygen composition and compare our data with the relevant reports such as Burton's work [157] which uses this as x-axis as well. It is evident that the E_f of most structures fall in the convex hull, only 4 structures have the E_f above zero. The composition X_O of these 4 structures ranges from 0.2 to 0.5, and we observed the nearest O-O distance in these structures was enlarged from 2.34 Å to 2.43 Å, 2.45 Å, 2.49 Å and 2.58 Å which cause the positive E_f. In addition, with the exception of two end points, there are 5 ground states found, namely Ti_6O, Ti_3O, Ti_2O, Ti_3O_2, and a new unreported compound, $Ti_{12}O_5$. Although the ground-state $Ti_{12}O_5$ was first found in this study, the compounds $Zr_{12}O_5$ and $Hf_{12}O_5$ were previously observed in the αZrO_X and αHfO_X system, respectively [158, 159].

Then we constructed a CE model to fit all the 365 DFT E_f energies and to predict the other potential ground states. A set of optimized clusters, consisting of 40 pairs, 40 triplets and 30 quadruplets, was employed to construct this CE. The DFT and CE fitted E_f and the residuals of the CE fit are shown in Figure 4.2. From the Figure 4.2 (a), we can see that the distribution of all data points is along or near the line of the function y=x, and there are no outliers far away

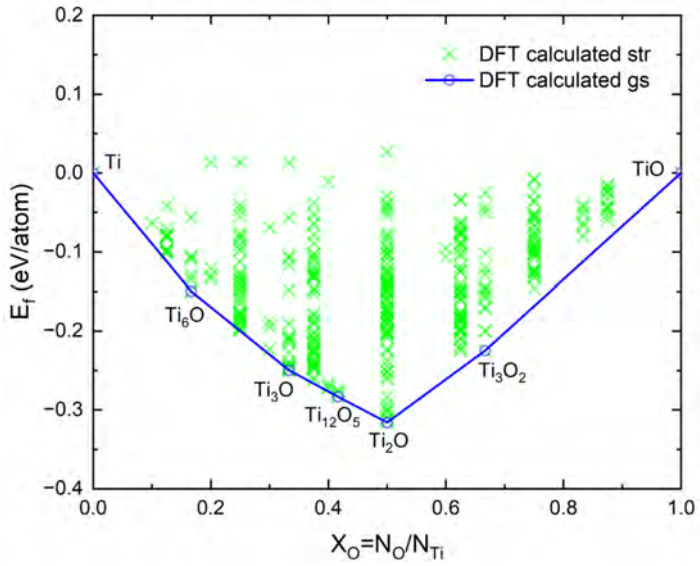

Figure 4.1: DFT Calculated formation energies (E_f) of the enumerated structures in hcp Ti-O system, the DFT ground-state orderings are connected as convex hull.

from y=x, indicating the DFT E_f are well fitted by the constructed CE model. It also can be seen from the Figure 4.2 (b) that the difference between the DFT calculated E_f and CE fitted E_f of all the configurations are less than 25 meV/atom. Most of the residuals of the CE fit are smaller than 10 meV and only the residuals of 3 configurations are slightly larger than 20 meV, which also indicates the constructed CE is well predictive. More importantly, the E_f errors between fitted and actual values of the ground states are 3.1 meV, 0.8 meV, 2.2 meV, 3.2 meV and 0.8 meV for the Ti_6O, Ti_3O, $Ti_{12}O_5$, Ti_2O and Ti_3O_2, respectively, which are very small and indicates the strong power of the constructed CE model for predicting the DFT energies. In addition, no configuration outside the convex hull was predicted by the CE model, which means there was no new ground-state existed in the Ti-O system.

On the other hand, the CV score of a CE model with predictive power is typically less than 25 meV/atom, this CE model achieved a low CV score of 6.13 meV/atom which indicates the CE model is well predictive. In order to get a more precise CE model, we calculated the relaxation amount (RA) of each configuration by taking into account the cell distortion before and after relaxation. As shown in Figure 4.3, the RA of all configurations is within 0.17, the maximum RA value is 0.168 appearing at the higher O content of 0.875 and 1. The value of RA increases with

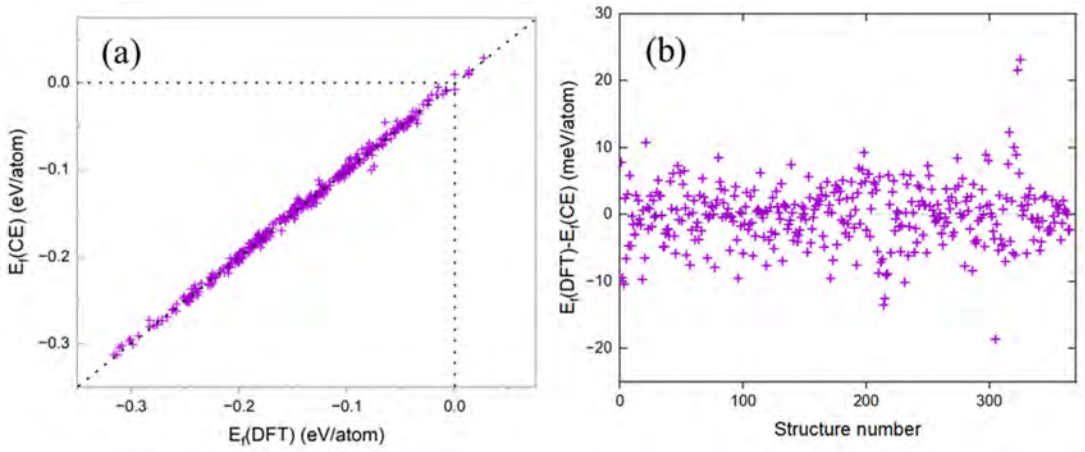

Figure 4.2: (a) The DFT and CE fitted E_f and (b) the residuals of the CE fit.

the increase of O content, which also reflects that the continuous addition of oxygen can increase the strain of the structure. Typically, the RA values above 0.1 are considered too much for the CE to be applicable, therefore those configurations with RA greater than 0.1 should be excluded from the establishment of the CE model, and the oxygen content of all these configurations is greater than 0.5. Many studies have shown that there is a limit to the solubility of oxygen in α Ti, for example as shown in the Ti-O phase diagram updated by H. Okamoto [21], the maximum solubility of oxygen is only 50 at.% which means that oxygen cannot occupy all the octahedral sites. And the fact that the two octahedral sites in the hcp Ti unit cell are highly energetic for oxygen occupation simultaneously was found very early on [160, 161]. Thus, in view of the above, the enumerated structures with E_f above zero and those with X_O larger than 0.5, including the ground-state Ti_3O_2, are excluded during the CE. In addition, structures farther away from the convex hull represent metastable or unstable higher-energy configurations that may exist under certain conditions but are less thermodynamically favorable. Assigning lower weights to these structures highlights their metastable nature and distinguishes them from the more stable phases represented by points closer to the convex hull. By adjusting the weights based on the distance from the convex hull, the convex hull diagram can effectively highlight the most stable phases while still including information about metastable phases. In this work, more importance is given to the configurations that are closer to the convex hull such that a very low weighted CV score of 2.45 meV/atom was obtained by fitting to the remaining 236 structures.

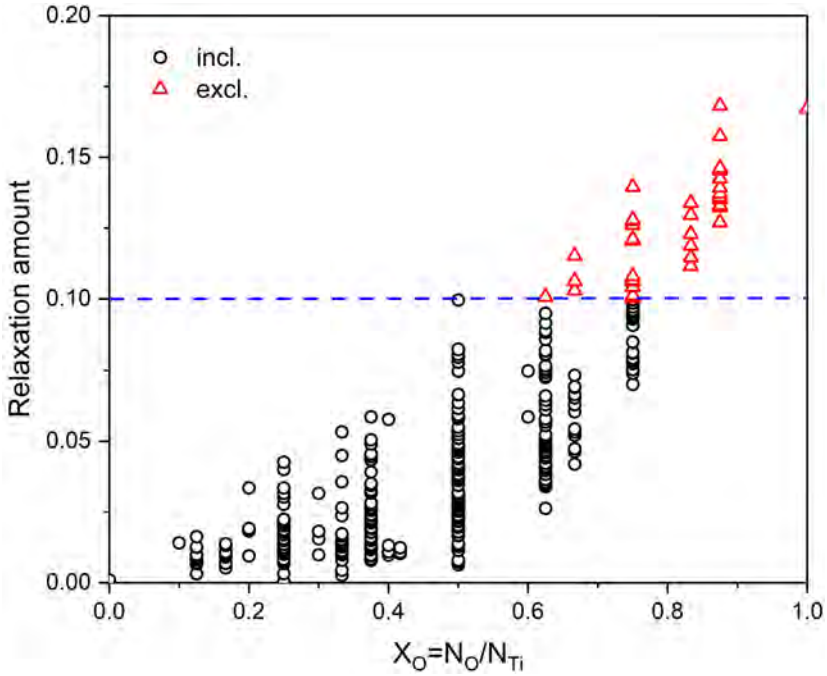

Figure 4.3: The relaxation amount (RA) of all the configurations in the hcp Ti-O system.

The crystal structures and lattice parameters of these 4 ground states are shown in Figure 4.4 and Table 4.1, respectively. It should be noted that, in the process of structure enumeration, first the ATAT calculates the factor group which represents the symmetry of the primitive structure of the input crystal structure, then the symmetry operations in the factor group are used to enumerate only the symmetrically unique configurations. Therefore, all the configurations including the ground states shown in Figure 4.4 and Table 4.1 belong to the same lattice system (hcp), however the space groups can be different. Except for the fact that the Ti_2O has an orthorhombic Pbcn space group, all the other three ground states have trigonal $R\bar{3}$ symmetry. The calculated lattice constants of pure hcp Ti are $a = 2.934$ Å and $c = 4.653$ Å, which are close to the theoretical values of $a = 2.932$ Å and $c = 4.644$ Å at 0 K and comparable with the experimental values of $a = 2.951$ Å and $c = 4.684$ Å at room temperature [162]. The nearest neighbor O-Ti distance in these ground states becomes larger than the Oct-Ti distance in pure Ti, which indicates that the oxygen enlarges the interstitial radius of the octahedral site. The ECIs of the optimized clusters including 20 pairs, 34 triplets and 26 quadruplets are shown in Figure 4.5. A high ECI value of 142 meV for the smallest pairwise cluster, with a radius of 2.34 Å, was calculated, which represents a strong oxygen-vacancy interaction. The magnitude of all the ECIs decays to zero

with the increase of the cluster diameter and the number of the sites it contains, which is due to the fact that the interaction strength between the sites in a structure should drop off with the increase of the site spacing.

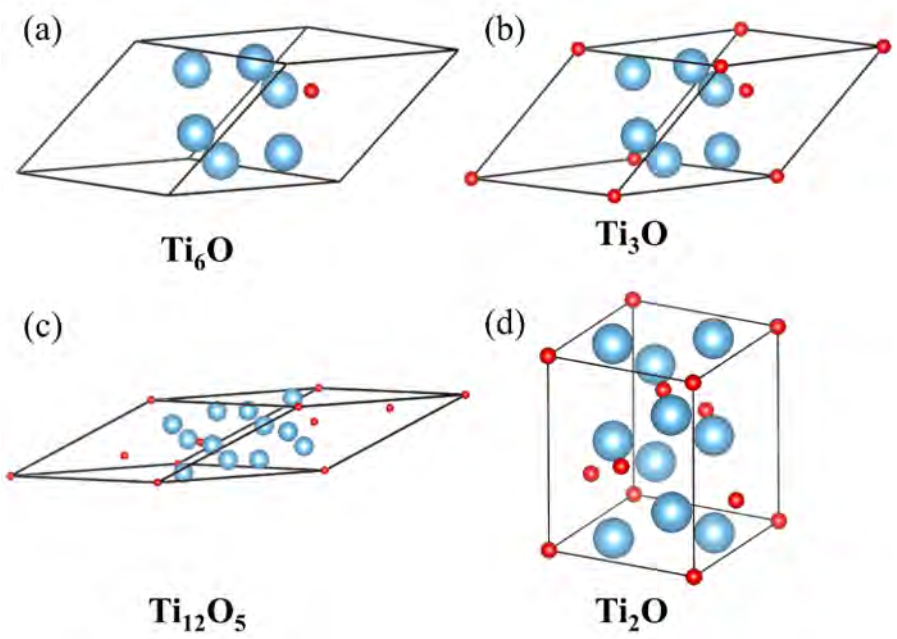

Figure 4.4: Crystal structures of the DFT ground states in hcp Ti-O system: (a) Ti_6O, (b) Ti_3O, (c) $Ti_{12}O_5$, and (d) Ti_2O (red balls are oxygen atoms occupying hcp octahedral sites). All these ground states belong to the hcp lattice system, because the symmetry operations in the factor group are used to enumerate only the symmetrically unique configurations.

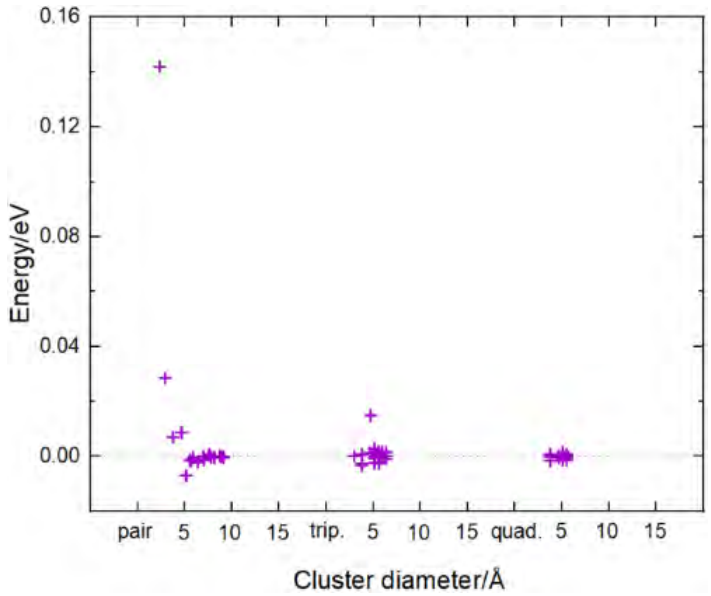

Figure 4.5: The effective cluster interactions (ECIs) of the optimized 20 pairs, 34 triplets and 26 quadruplets in αTiO CE.

Table 4.1: Lattice parameters of the ground states found in hcp Ti-O system.

Ground-state	Structure	Space group	a(Å)	b(Å)	c(Å)	$\alpha(^\circ)$	$\beta(^\circ)$	$\gamma(^\circ)$
Ti_6O	trigonal	R3	5.588	–	–	54.45	54.45	54.45
Ti_3O	trigonal	R3	5.604	–	–	54.83	54.83	54.83
$Ti_{12}O_5$	trigonal	R3	10.029	–	–	29.78	29.78	29.78
Ti_2O	orthorhombic	Pbcn	4.79	5.111	6.01	90	90	90

4.2 Electronic structures of the ground states

To better understand the underlying physical mechanism of the properties of different ground states and phases, electronic structure calculation analysis enables us to reveal the interatomic interactions and bonding characteristics between unlike atoms. First, we calculated the density of states (DOS) which describes the distribution of electronic energy states of a configuration by [163, 164]:

$$D(E) = \frac{1}{V}\sum_{i=1}^{N}\delta(E - E(\mathbf{k}_i)) \tag{4.2}$$

where V, N and δ are the volume, the number of countable energy levels and the Dirac delta function, respectively. E and E($\mathbf{k}_i$), respectively, represent the energy at which the DOS is evaluated and the energy of each electronic state i with the wave vector $\mathbf{k}$. The total density of states (DOS) and O and Ti orbit-projected DOS are illustrated in Figure 4.6, with the energy of Fermi level (E_{Fermi}) set to 0. It can be seen that all the ground states show metallic characteristics, since the Fermi Energy resides in the middle of the d band. The states around 20 eV below E_{Fermi} are contributed by the oxygen 2s orbital when the oxygen is introduced in hcp Ti. Moreover, the p orbitals of oxygen hybridize with the d orbitals of Ti below the E_{Fermi} to form σ and π bonds, and notably the bond strength enhances with the increase of oxygen concentration, which can be demonstrated by the variation trend of the E_f of these ground states, shown in Figure 4.1. The DOS in the energy interval spanning the E_{Fermi} is dominated by the d orbitals of Ti.

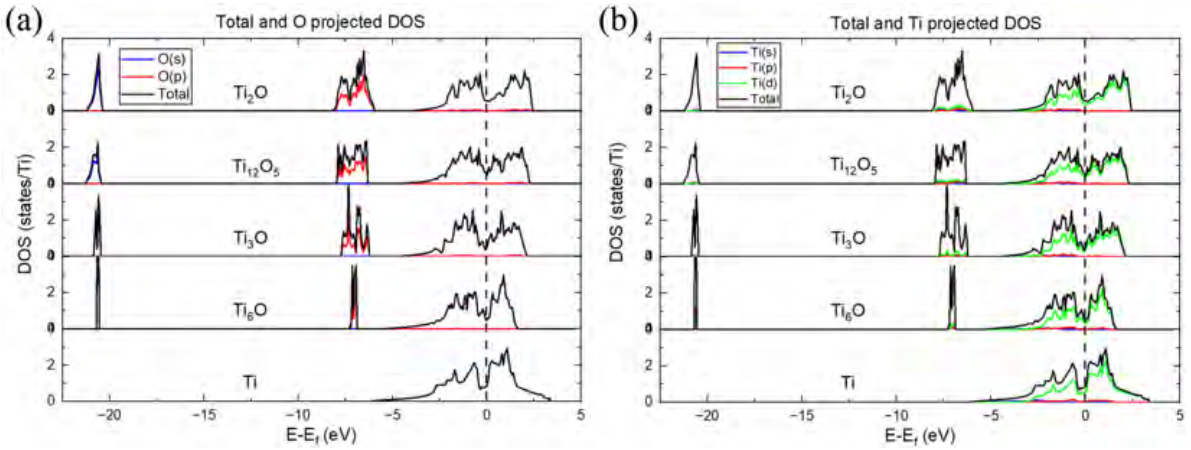

Figure 4.6: DOS of the ground-sates Ti, Ti_6O, Ti_3O, $Ti_{12}O_5$ and Ti_2O: (a) Total and O projected DOS; (b) Total and Ti projected DOS.

To further understand the nature of the chemical bond formation, we evaluated the effect of the addition of oxygen on the electron density by calculating the charge density difference which represents the variation in electron density before and after the addition of oxygen via [165]:

$$\Delta\rho = \rho_{Ti_xO_y} - \rho_{Ti_x} - \rho_{O_y} \tag{4.3}$$

where $\rho_{Ti_xO_y}$ represents the total charge density of the ground-state Ti_xO_y, ρ_{Ti_x} and ρ_{O_y} are the charge density of the systems after removing all the oxygen and Ti atoms from the ground-state Ti_xO_y and leaving the structure unrelaxed, respectively. The 3D charge density difference of all the ground states is shown in Figure 4.7, here in order to view more clearly the gain and loss of electrons between oxygen and Ti, we only intercepted the fragments of the charge density distribution between the oxygen atom and the nearest neighbor Ti atoms (fragments in Figure 4.4). The yellow and green regions indicate the positive and negative charge density difference, respectively. It can be seen that the charge density difference of all the ground states concentrates around the oxygen atom, indicating that the bonding between Ti and O in each ground-state is a process of oxygen atom gaining electrons and Ti atom losing electrons. In addition, except for $Ti_{12}O_5$, which has two types of charge density difference distribution, all other ground states have only one type of Ti-O bond. Ti_6O has a charge density distribution with a shape between spherality and cube. The shape of the charge density difference of Ti_3O looks like a bowl with

a symmetrical central depression. The two types distribution of the charge density difference of $Ti_{12}O_5$ is more like a mixture of charge density difference distribution of Ti_6O and Ti_3O. However, Ti_2O has a charge density difference shape that is completely different from that of the other three ground states, and it appears to be a symmetric semi-ellipsoidal shape. In essence, the difference in the electron cloud shape for the charge density difference of each ground-state demonstrates the difference of the electron configuration in space and thereby the difference in the bond strength. This can be clearly observed from the sliced plane of the 2D charge density difference, as shown in Figure 4.8 where the saturation of the color corresponds to the magnitude of the charge density difference. Warm colors indicate larger differences in charge density, while cool colors indicate smaller differences. In all ground states, compared to oxygen atoms, the change in charge density around Ti atoms is relatively smaller. However, the maximum charge density difference around oxygen atoms increases with the increase of the Ti concentration. For instance, the charge density differences around the oxygen atoms in Ti_6O are distributed in a ring shape with the maximum charge density difference of 0.17 e/A^3, and the changes are more obvious at the four corners, while the charge density changes around the oxygen atoms in Ti_3O are stronger with the maximum charge density difference of 0.20 e/A^3 and are distributed on both sides of the oxygen atoms in a fan shape. Similarly, the changes of the charge density around oxygen atoms in $Ti_{12}O_5$ have two types and look like the mixture of the type of charge density difference in Ti_6O and Ti_3O. In particular, the charge density around the oxygen atom in Ti_2O changes the most and is distributed on both sides of the oxygen atoms, showing a larger fan shape than that in Ti_3O.

The Bader analysis [166, 167] was then performed to compute the gain and loss of electrons on each Ti and oxygen atom. As shown in Table 4.2 where positive and negative values, respectively, refer to the gain and loss of electrons on each atom in the ground states, compared to the ground-state Ti_6O, the oxygen atoms in all the other ground states gain more electrons from Ti atoms. Accordingly, the Ti atoms lose more electrons with the increase of oxygen concentration from $X_{O=0.167}$ to $X_{O=0.5}$, and the gradient of this change achieves the largest when X_O changes from 0.167 to 0.333, that is, each Ti atom loses about 0.268 electrons. On the

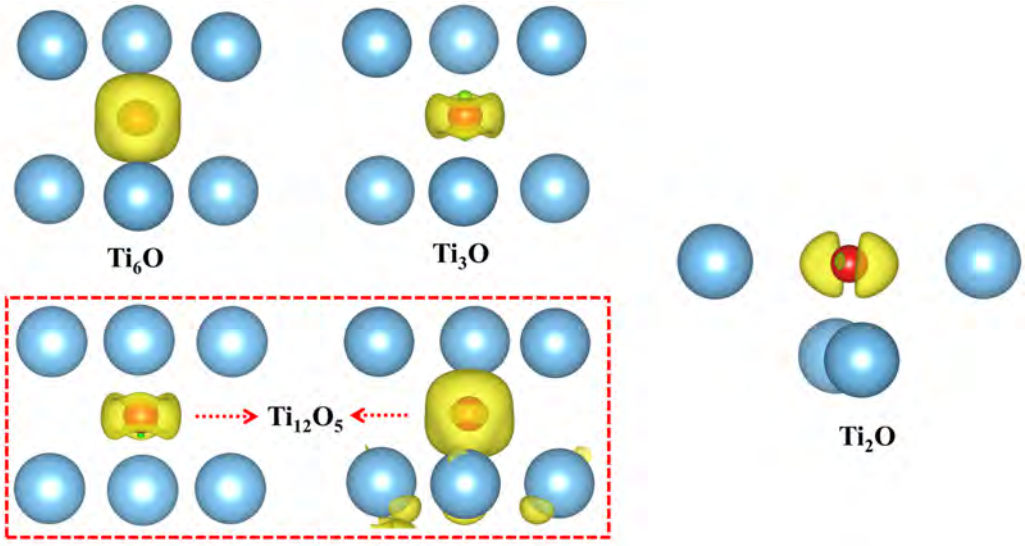

Figure 4.7: Charge density difference of the ground states in hcp Ti-O CE. The yellow and green regions indicate the positive and negative charge density difference, respectively. Warm colors indicate larger differences in charge density, while cool colors indicate smaller differences.

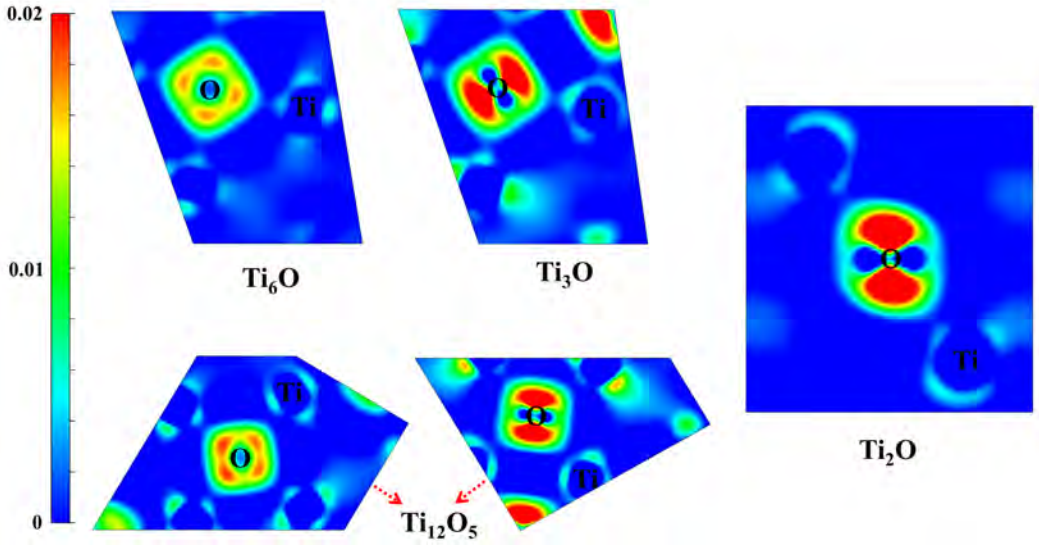

Figure 4.8: Sliced planes of the charge density difference of the ground states in hcp Ti-O CE, the unit is in e/A^3.

other hand, the introduction of oxygen into the hcp Ti lattice can cause the elongation of the lattice parameters and the expansion of the lattice volume. Table 4.3 shows the lattice constants and volumes of the originally relaxed hcp unit cells obtained through symmetry operations for each ground-state. As expected, the lattice constant a and c of all the ground states increased compared to the original pure Ti unit cell, and the volume expansion rates of the ground-states Ti_6O, Ti_3O, $Ti_{12}O_5$ and Ti_2O are 3.64 %, 5.48 %, 6.35 % and 5.68 %, respectively, compared

to the volume of the Ti unit cell. It is unexpected that the $Ti_{12}O_5$ exhibits the largest volume expansion among all the ground states, which may be due to the fact that two type Ti-O bonds with different differential charge densities in $Ti_{12}O_5$ appear alternately on the stacking planes passed by the [111] crystal orientation. Figure 4.9 shows the lattice constants and volume versus the oxygen concentration of the hcp Ti-O ground states. It can be seen that, as expected, the change of the *c* length of each ground state follows Vegard's law, however, the change trend of the *a* length is not linear since the oxygen ordering along each crystal orientation in these ground states is different as confirmed in Figure 4.13. As shown in Figure 4.9 (c), some deviations from the linear change also can be observed in the change of the volume with the composition. This is normal because Vegard's law is indeed seldom perfectly obeyed, and many systems obey Vegard's law but a lot do not [168, 169].

Table 4.2: Gain and loss of electrons of each Ti and oxygen atom in the hcp Ti-O ground states via Bader analysis.

Ground-state	O atoms	Ti atoms
Ti_6O	+1.278	-0.183,-0.188, -0.212, -0.224, -0.246, -0.225
Ti_3O	+1.444	-0.481, -0.481, -0.481
$Ti_{12}O_5$	+1.46, +1.46, +1.445, +1.466, +1.444	-0.503, -0.71, -0.709, -0.503, -0.503, -0.71, -0.709, -0.502, -0.503, -0.71, -0.709, -0.502
Ti_2O	+1.437	-0.718, -0.719

4.3 Vibrational properties and volumetric expansion of the ground states

Thermodynamic properties are essential to describe the state of a solid system at various temperatures. In the previous two sections, we discussed the energetics of the hcp Ti-O system at 0 K and the electronic structure properties of the ground states. However, as the environmental

Table 4.3: Lattice constants and volume of the unit cell of the hcp Ti-O ground states.

Ground-state	a length(Å)	c length(Å)	volume(Å^3)
Ti	2.934	4.653	34.644
Ti_6O	2.952	4.745	35.906
Ti_3O	2.979	4.747	36.542
$Ti_{12}O_5$	2.976	4.788	36.843
Ti_2O	2.964	4.790	36.61

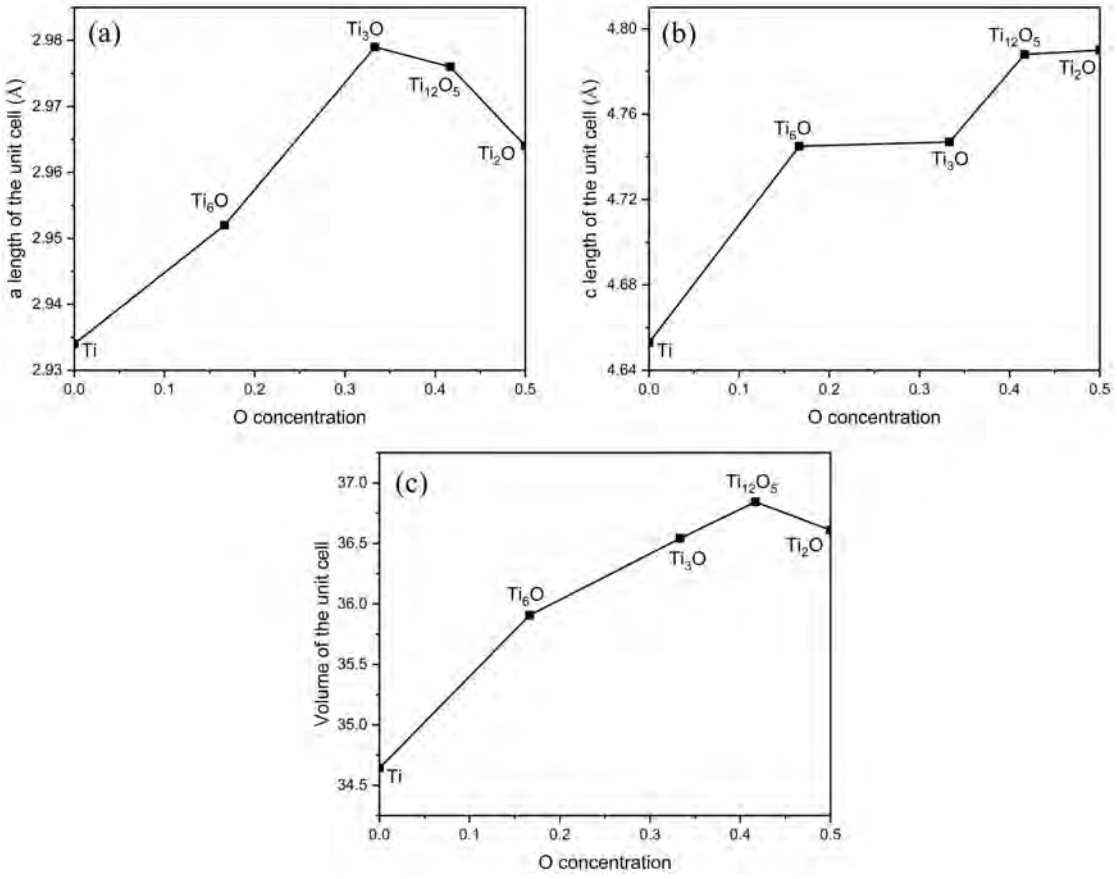

Figure 4.9: Lattice constants and volume versus the oxygen concentration of the hcp Ti-O ground states.

temperature increases, it may be inaccurate to only account for the configurational free energy of the system. This is because when the temperature increases, the atoms or ions in the crystal lattice can oscillate away from the equilibrium position, and this oscillation could be

more severe at high temperatures [170]. For another, the volume expansion of the lattice also increases with the increase of temperature, in which the oscillation of the atoms plays an important role [171]. This atomic oscillation is also known as lattice vibration. In addition, in some cases, lattice volumetric expansion can also be influenced by anharmonic effects, where the restoring forces between atoms or ions are not purely harmonic. Anharmonic effects can lead to deviations from ideal behavior, such as non-linear temperature dependence of lattice parameters and thermal expansion coefficients [172, 173]. Here, the Debye-Grüneisen model we applied accounts for both harmonic and anharmonic effects in the vibrational properties of Ti-O system. Specifically, the Grüneisen parameter, introduced in the Debye-Grüneisen model, quantifies the anharmonicity of the vibrational modes [174].

To investigate the vibrational properties and thermal expansion of the ground states, firstly, a series of energy-volume (E-V) data of the full relaxed structures were calculated and fit to the zero-order Birch–Murnaghan equation of state [175]. The ordering $Ti_{12}O_5$ was not observed in experiments since our study shows it decomposes on heating into Ti_3O and Ti_2O at very low temperature ($\sim$ 50 K), its vibrational properties and thermal expansion are not discussed here. Figure 4.10 shows the E-V curve of all the four stable ground states, the volume changes of all the configurations were imposed by changing the scale factor of the lattice parameters of the relaxed configuration at equilibrium from 0.95 to 1.05, that is, the volume change is within 5 %. It can be seen that there is no unusual point outside the E-V convex hull of all the ground states, thereby all the E-V data points can be well fitted by the Birch–Murnaghan equation of state. These E-V data can then be used to evaluate the thermodynamic properties of the configuration of the ground states. For instance, the calculated static bulk modulus at 0 K is shown in Table 4.4, our results achieve good agreement with the DFT data reported by Tang, Andersson and Mei *et al*. [176–178], though no literature reported the bulk modulus of Ti_6O. Besides, the DFT data in the Materials Project platform overestimated the bulk modulus for all the ground states, especially for Ti_6O and Ti_3O, which is possibly due to that the Ti_6O and Ti_3O structure collected by Materials Project [179] are not the most stable configuration at respective composition. Specifically, the Ti_6O and Ti_3O in the Materials Project have the space group of

$P\bar{3}1c$ which is different from the configurations we obtained. Moreover, the reported E_f of the Ti_6O and Ti_3O in the Materials Project are -0.886 and -1.525 eV/atom which are higher than those we calculated. In other words, the E_f of these configurations should fall inside the convex hull in Figure 4.1, not on or outside the convex hull line. The temperature-dependent isothermal bulk modulus can be calculated by [144]:

$$B_T = -V\left(\frac{\partial p}{V}\right)_T \tag{4.4}$$

where the p and V are the pressure and the initial volume of the ground-state. Figure 4.11 shows the volume expansions and the bulk modulus ratio of the ground states, all thermodynamic data are normalized by V_0 and B_0 which are the equilibrium cell volume and bulk modulus at 300 K, respectively. It is obvious that the change trend of volume expansion for all ground states is very similar, especially below 700 K. As the temperature exceeds 800 K, Ti_2O exhibits the maximum volume expansion rate, followed by Ti_3O and finally Ti_6O. Our results for Ti_2O almost overlap with the data reported by Tang *et al*. [176], though there is a little difference in the volume expansion rate of Ti_3O. Moreover, it can be seen from Figure 4.11(b), compared to Ti_3O and Ti_6O, the bulk modulus of Ti_2O decreases faster when the temperature is above 300 K, and the bulk modulus ratio reaches the lowest value of about 0.74 at 1200 K. However, the results of Tang *et al*. show that the bulk modulus of Ti_3O decreases the fastest, reaching a minimum of 0.77 at 1200 K. This slight difference may be due to the use of different algorithm in relaxing the atoms and lattice parameters of the structures. The Broyden-Fletcher-Goldfarb-Shannon algorithm is used in the relaxation calculations in their study, while we use the conjugate-gradient algorithm to perform full relaxation calculations for these ground states.

The thermal expansion and heat capacity of the ground states, indicating their anharmonicity and heat retention or loss ability [180], were also calculated by the Debye-Grüneisen model. Except for the inclusion of the configurational degrees of freedom, the F_{vib} was also determined to view its effects on phase stability. The obtained equilibrium volume at a given temperature

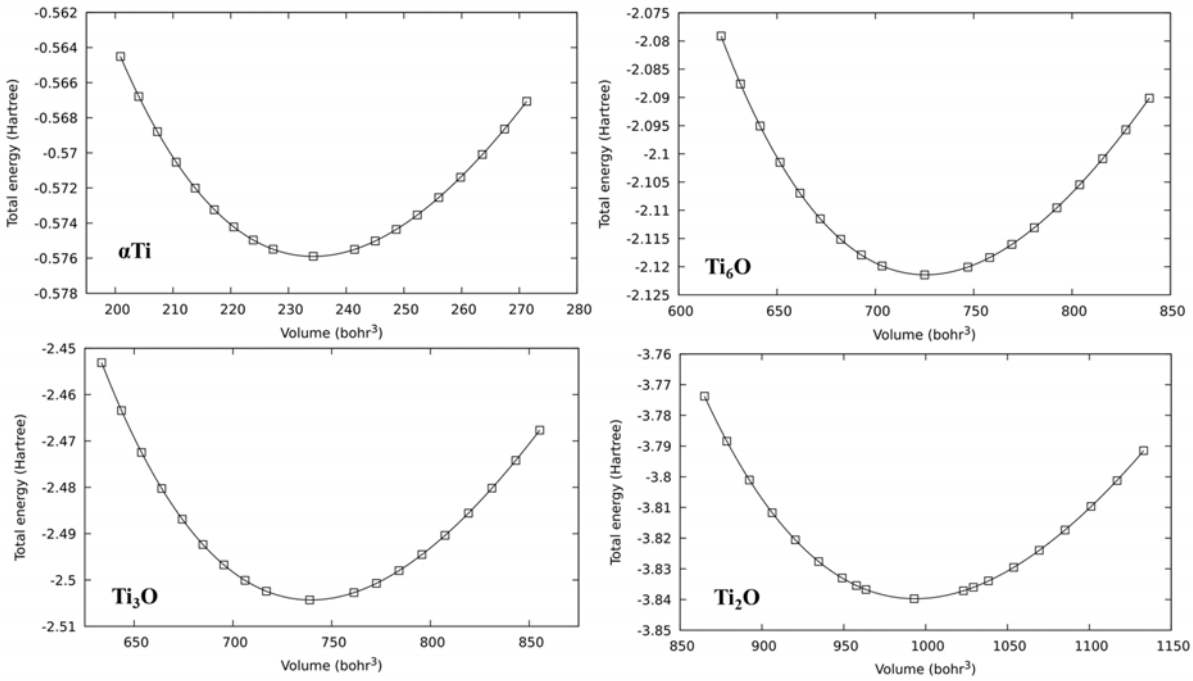

Figure 4.10: E-V data and the fitted curve of the pure αTi, ground-states Ti_6O, Ti_3O and Ti_2O.

Table 4.4: 0 K static bulk modulus of the hcp Ti-O ground states, some DFT data from literature was used for comparison, units in GPa.

Ground-state	This study	Tang *et al.*[176]	Materials Project[179]	Andersson *et al.*[177]	Mei *et al.*[178]
Ti	112	-	113	-	110
Ti_6O	131	-	141	-	-
Ti_3O	153	151	164	160	-
Ti_2O	183	187	184	182	-

and pressure can be used to derive the linear thermal expansion λ by:

$$\lambda = \frac{1}{3V}\left(\frac{\partial V}{\partial T}\right)_p \tag{4.5}$$

The total F_{vib} and the linear thermal expansions of Ti_6O, Ti_3O and Ti_2O are shown in Figure 4.12. With the increase of temperature, the F_{vib} of these three ground states gradually drops,

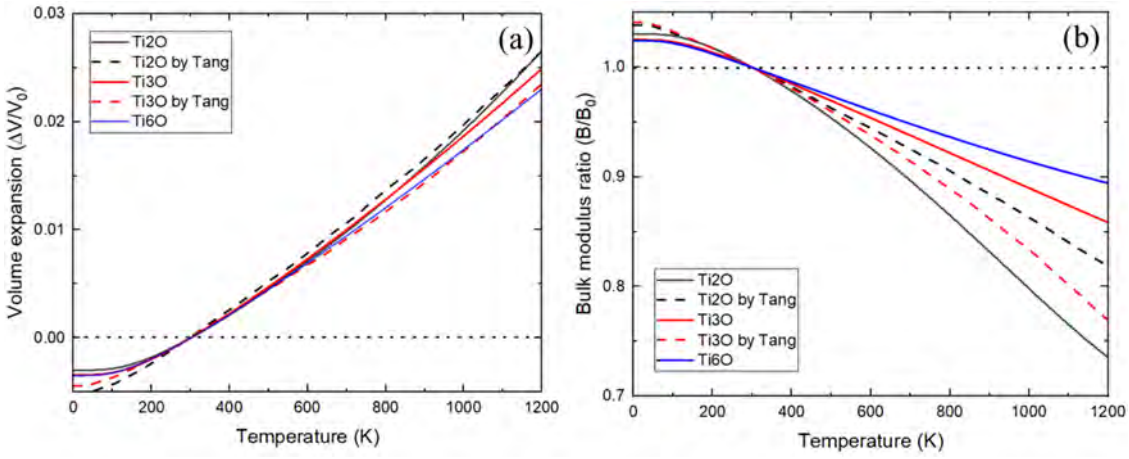

Figure 4.11: (a) volume expansions and (b) the bulk modulus ratio of the ground-state Ti_6O, Ti_3O and Ti_2O.

this can be interpreted by the well-known volume effect which is basically attributed to thermal expansion: the volume expansion of a given compound stretches chemical bonds, which in turn makes them softer, leading to an increase in vibrational entropy [181]. It also can be seen that the Ti_2O has the largest reduction rate over the whole temperature range since it has the biggest growth rate of linear thermal expansion (shown in Figure 4.12(b)), indicating the anharmonic contributions are non-negligible especially at higher temperatures [182]. On the other hand, the number of the bonds between unlike atoms determines the stiffness of a structure or phase in a system [181]. As shown in Figure 4.13, though oxygen atoms fill alternating layers of octahedral sites in Ti_6O and Ti_3O, oxygen occupies more sites in Ti_3O in the same layer. In Ti_2O, oxygen orders as zigzag rows on the same layer of octahedral sites and can be distributed on adjacent octahedral interstitial layers, rather than being distributed on the alternating layers as Ti_6O and Ti_3O. Therefore, Ti_2O has a larger number of Ti-O bonds than Ti_3O, followed by Ti_6O. The increase in bonds not only contributes to the stiffness of the structure and the reduction of the E_f (as shown in Figure 4.1(a)), but also leads to a decrease in vibrational entropy, and therefore a stiffer structure. Therefore, as shown in Figure 4.12(a), the vibrational free energy of the three ground states over a wide temperature range (0 ~ 950 K) show the ordering: Ti_2O>Ti_3O>Ti_6O.

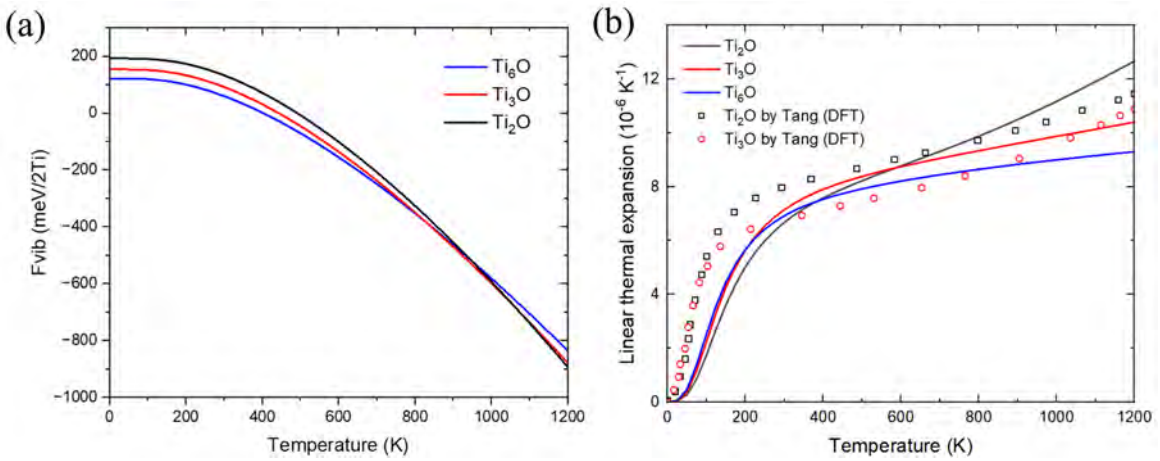

Figure 4.12: Temperature dependence of the (a) total vibrational free energy and (b) linear thermal expansion for the ground-states Ti_6O, Ti_3O and Ti_2O. The data of the Ti_3O with P-31C structure and the Ti_2O with P-3M1 structure used in is plotted here for comparison [176].

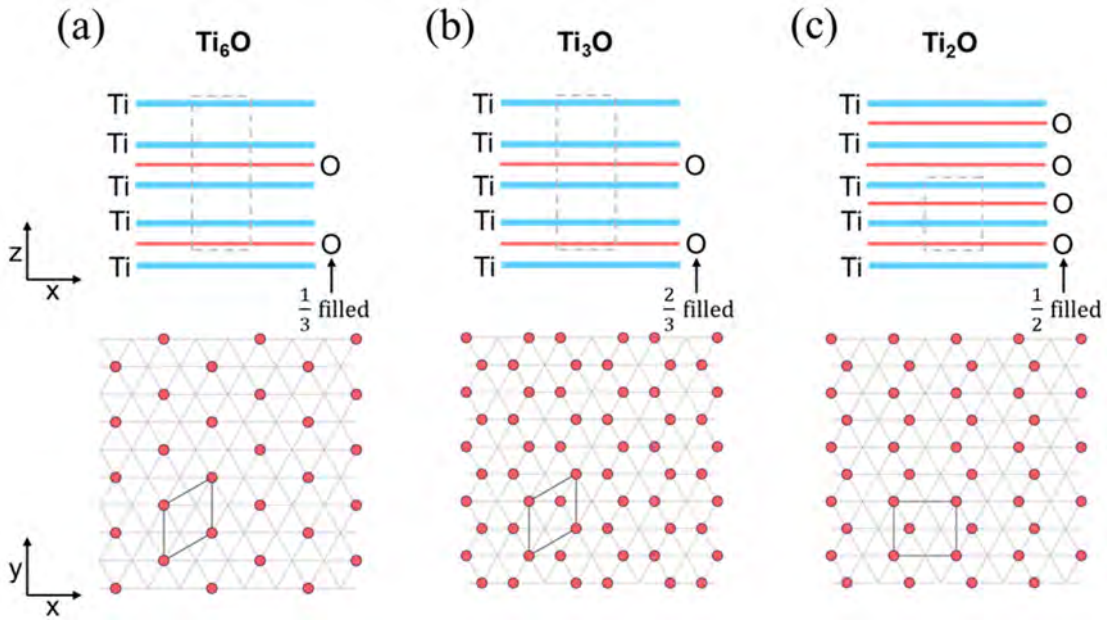

Figure 4.13: The orderings of oxygen atoms on the x-y and x-z planes in Ti_6O, Ti_3O and Ti_2O.

The constant pressure and constant volume heat capacity can be calculated by [144]:

$$C_p = \left(\frac{\partial H}{\partial T}\right)_p \quad C_v = \left(\frac{\partial U}{\partial T}\right)_p \tag{4.6}$$

where H and U are the enthalpy and internal energy of the configuration respectively which can be derived from the Helmholtz free energy. The specific heat at constant pressure (C_p) and constant volume (C_v) of the ground states are shown in Figure 4.14. Similar to other

metal compounds, their heat capacity increases with the increase of temperature, and the higher the temperature, the slower the change rate [183]. In addition, the heat capacity of Ti_6O is significantly higher than that of the other two ground states as more atoms mean more atomic degrees of freedom existed in the structure, where each degree of freedom contributes equally to the heat capacity at higher temperatures. Unfortunately, the simulation and experimental reports on the temperature dependence of the thermodynamic properties of these three ground states are extremely scarce, hence the thermodynamic properties of Ti_2O and Ti_3O with respective P-3M1 and P-31C space groups examined by Tang *et al*. were used for comparison [176]. Our calculated C_p and C_v for Ti_3O and Ti_2O are in good agreement with those reported by Tang, due to the little difference in formation energy of the corresponding ground-state. For instance, the formation energy of the P-31C Ti_3O found in our CE is -0.248 eV/atom which is slightly higher than that of ground-state R3 Ti_3O (-0.25 eV/atom).

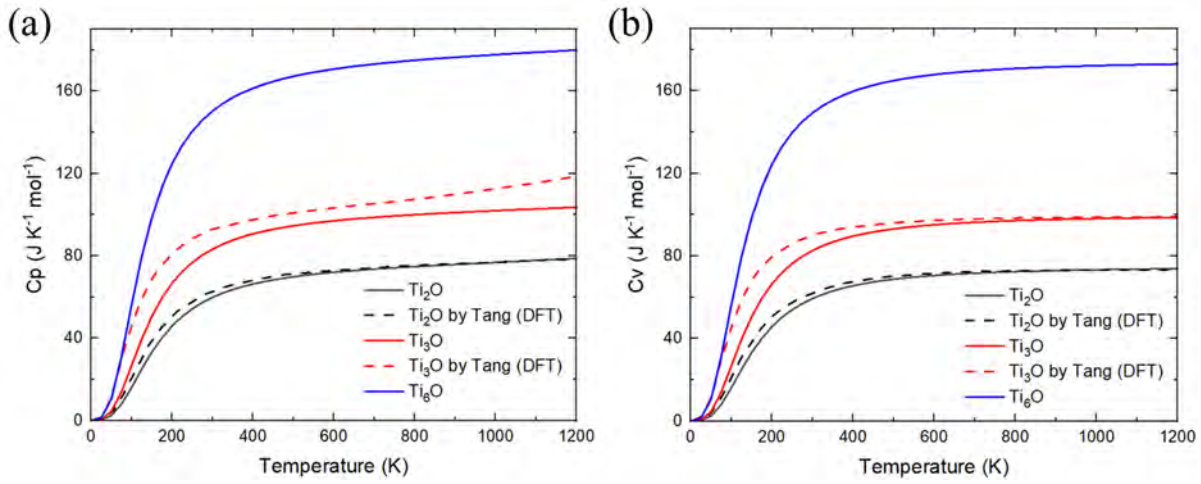

Figure 4.14: The constant-pressure (a) and constant-volume (b) heat capacities of the ground-states Ti_6O, Ti_3O and Ti_2O as a function of temperature.

4.4 Thermodynamic properties of the ground states

Although we have obtained the thermodynamic and mechanical properties of different ground states at various temperatures through Debye-Grüneisen model and DFT calculations, in order to investigate the thermodynamics of the ground states over various compositions and temperatures,

statistical mechanics methods are often applied to get the thermodynamic quantities. Here, Monte Carlo simulation implemented in the *emc*2 code was used to calculate the Gibbs free energy and order-disorder transition temperatures for the Ti-O ground states. The size of the simulation cell in the Monte Carlo simulations is determined by the radius specified, specifically, the simulation cell size is the smallest supercell that both contains that sphere and that is commensurate with the unit cell of the ground-state of interest. Up to 2000 average and equilibrium passes were performed in the Monte Carlo simulations to evaluate thermodynamic quantities at each step of these simulations.

The calculated Helmholtz free energy (F) at several temperatures for the pure αTi phase, ground-state Ti_6O and Ti_3O is shown in Figure 4.15, where the active site in the unit of F indicates the octahedral sites in the O-Vac sublattice without inclusion of the Ti sites since there is no degrees of freedom on the Ti sublattice. The F can be regarded as the Gibbs free energy at atmospheric pressure in solid-state systems because the product of pressure P with changes in specific volume (ΔV) are very small [69]. It can be seen that, at 600 K, αTi and Ti_6O undergo phase transitions at oxygen concentration of 6.4 at.% and 13.1 at.%, respectively. This gap in oxygen concentration narrows with the increase of temperature, decreasing to 2.4 at.% at 800 K, which means as the temperature continues to go up, the αTi and Ti_6O phase may meet and the Ti_6O could undergo an order-disorder phase transition. Besides, for the Ti_6O and Ti_3O phase, the gap in oxygen concentration is 7.4 at.% at 400 K, however as the temperature increases from 400 K to 600 K, this value rapidly drops to 2.2 at.%. This indicates that compared to αTi and Ti_6O, the Ti_6O and Ti_3O phase could meet at a lower temperature. Since the solid-state transformation of αTi + $Ti_2O \rightarrow Ti_3O$ + Ti_2O occurs at around 547 K and the gap in oxygen concentration between Ti_2O and Ti_3O or αTi does not change obviously with increasing temperature, the calculated F of Ti_2O is not shown in Figure 4.15. The phase boundaries between these ground states are then constructed, as shown in Figure 4.16, by applying the common tangent method to the calculated F of each ground-state. The oxygen concentration is calculated by $N_O/(N_O+N_{Ti})$ for convenient comparison with the literature. It is evident our calculated αTi and Ti_6O phase boundary is below those reported by Burton *et al*. [157] and Gunda *et al*. [184], and the solubilities of Ti_6O

and Ti_3O in hcp Ti are a little narrower than the results of Burton. Moreover, our work show that the lowest temperatures that pure Ti_6O and Ti_3O can appear are 370 K and 345 K respectively, which are 190 K and 215 K higher than Burton's results of 180 K and 130 K respectively. In addition, we also underestimated the highest temperature of the coexistence of Ti_3O and Ti_2O and thereby a narrower coexistence span for Ti_3O and Ti_2O was obtained in this study.

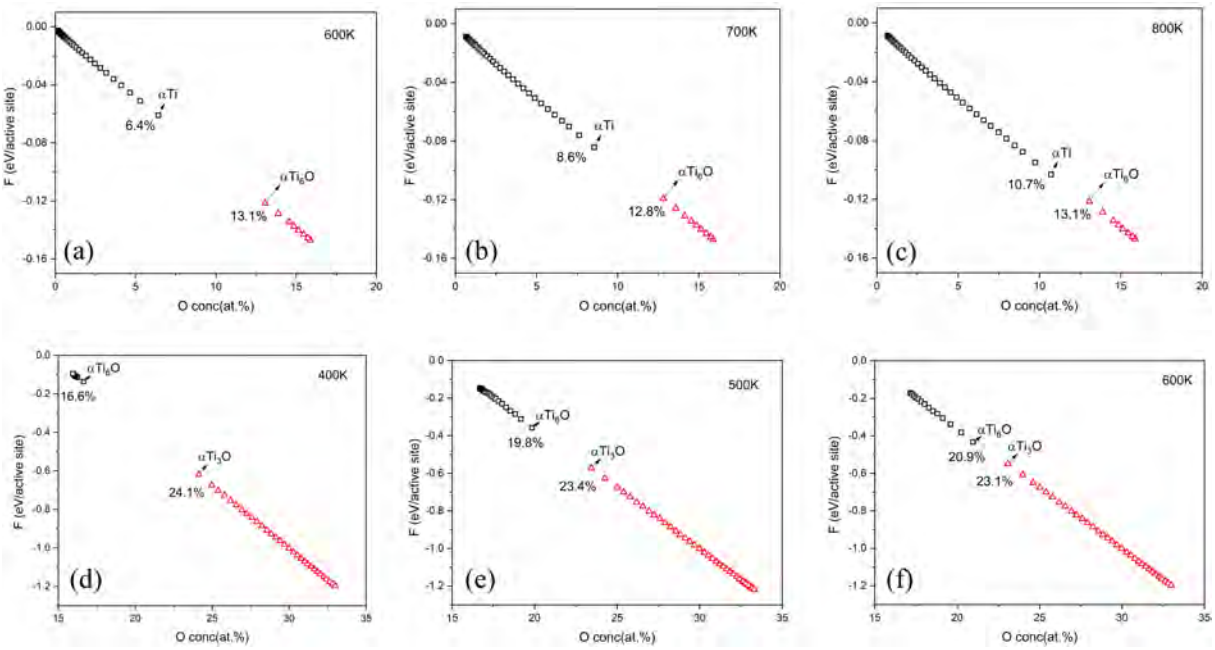

Figure 4.15: The calculated Helmholtz TiO free energy (F) versus composition of the pure αTi, ground-state Ti_6O and Ti_3O at different temperatures.

The effects of lattice vibration on the order-disorder transition temperature of Ti_6O, Ti_3O and Ti_2O were also examined by performing Monte Carlo simulations, as shown in Table 4.5. It is evident that vibrational entropy lowers the transition temperatures for all the phases, and this effect has greater impact on Ti_6O and Ti_2O. Our calculated transition temperatures without including vibrational free energy for all the three ground states are in good agreement with those reported by Gunda *et al*. [184]. About 207 K difference on the transition temperature of Ti_6O excluding vibrational free energy obtained in this paper and Burton *et al*. [157] could arise from the difference of the ground-state structure as obtained from the first-principles simulations. The most stable Ti_6O structure at 0 K found by Burton contains 18 Ti atoms and 3 O atoms with the similar R3 symmetry, and its formation energy (-0.1471 eV/atom) is slightly higher than that of Ti_6O (-0.1489 eV/atom) consisting of 6 Ti atoms and 1 O atom found in this work. It is

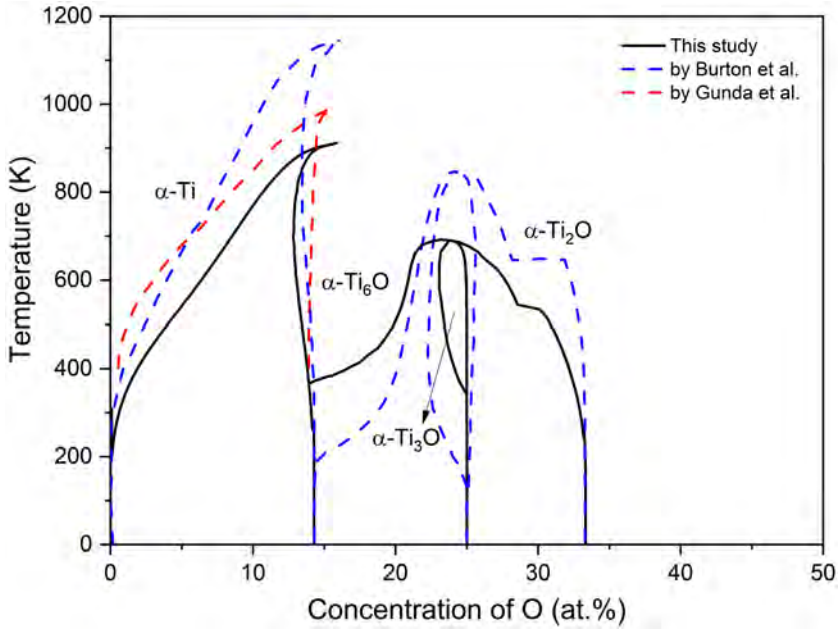

Figure 4.16: The calculated phase boundaries between αTi, ground-state Ti_6O and Ti_3O, with the oxygen concentration calculated by $N_O/(N_O+N_{Ti})$.

worth noting that the transition temperatures of Ti_2O reported by Burton and Ruban *et al.* [185] reach 1612 K and 2860 K, respectively, which is 479 K and 1727 K higher than that reported here. The difference of 1727 K is possibly due to the fact that a different ground-state was used, as Ruban *et al.* used a Ti_2O ground-state that has an anti-CdI2 structure ($P\bar{3}m1$), which we find has a 22.73 meV/atom higher E_f than that of Ti_2O found in this work. The difference in transition temperature between this study and the work by Burton *et al.* is probably due to the higher accuracy of our cluster expansion, which is based on a much larger number of structures. Specifically, 96 supercells were enumerated and calculated by DFT in their work, while the DFT energies of 365 configurations across the whole composition range were analyzed in this study. There is no DFT calculation reported anywhere else to take the vibrational contribution into consideration. Our calculated transition temperature for Ti_6O with the inclusion of F_{vib} (745 K) is the one closest to the experimental data (700 K) among those DFT investigations. This little overestimation on the phase transition temperatures was also observed in some other alloys [186–188]. However, the transition temperature of the phase Ti_3O was unexpectedly underestimated versus experimental observation [185], this was also captured by Gunda *et al.* in spite of their neglect of the effect of vibrational entropy.

Table 4.5: Order-disorder transition temperatures of Ti_6O, Ti_3O and Ti_2O with and without inclusion of vibrational free energy (F_{vib}), temperature in K.

	This study				
Phase	w/o F_{vib}	w/ F_{vib}	Gunda *et al.*[184]	Burton *et al.*[157]	Expt.[185]
Ti_6O	913	745	999	1120	700
Ti_3O	689	656	609	860	780-850
Ti_2O	1133	914	1027	1612	–

4.5 Summary

In this chapter, a comprehensive understanding of the phase stability in the hcp Ti-O system at 0 K was achieved by performing a series of first-principles calculations. Some stable ordering oxides were identified by constructing the convex hull diagram for the E_f of the enumerated structures, namely Ti_6O, Ti_3O, $Ti_{12}O_5$ and Ti_2O. The ground-state compound with stoichiometry $Ti_{12}O_5$ was reported in the αTi-O CE for the first time in this study. CNA results show all the structures keep hcp geometry after full relaxation, which objectively demonstrates oxygen can stabilize α phases in the hcp Ti-O system. To remove the noises in the CE, we excluded the highly distorted structures, structures with X_O larger than 0.5 and configurations with E_f larger than 0. A good predictive CE model, achieving a CV score of 2.45 meV/atom, was constructed by fitting to the remaining structures. We also found a strong O-O or O-Vac interaction with ECI value of 142 meV appeared in the smallest pairwise cluster. The electronic structures of the ground states were further analyzed, and found that bonding strength of the formed σ and π bonds enhances with the increase of interstitial oxygen concentration. This bonding interaction appearing on the nearest-neighbor Ti and O atoms is attributed to the hybridization between oxygen p orbitals and Ti d orbitals. In addition, the thermodynamic properties of the ground-state phases were also investigated for the first time. It was shown that Pbcn Ti_2O has the largest F_{vib} than the other ground states, and our calculated volume expansion, linear thermal expansion, bulk modulus

ratio and heat capacities of the ground-states Ti_3O and Ti_2O are comparable to the work by Tang *et al*. though no data was available for comparison with Ti_6O. Furthermore, the computed phase boundaries between these ground states are lower than the results reported by Burton *et al*. and Gunda *et al*. which may be due to that we constructed a E_f training set with much more configurations, leading to a lower CV score. The vibrational CE was also constructed and the order-disorder transition temperatures of these oxide phases were calculated without and with the inclusion of lattice vibration. It is found that vibrational entropy yields downward corrections to the computed transition temperatures for all the phases, although, compared with experimental data, our results still slightly overestimate and underestimate the transition temperatures for Ti_6O and Ti_3O, respectively.

Chapter 5

Hcp and Bcc Ti-Nb system

(Some of the work presented in this chapter is adapted from [131])

For the Ti-Nb system, VASP was also used to perform DFT calculations to calculate the total energies of the enumerated configurations and analyze the electronic structures of the ground states. The *maps* code in ATAT [62] was used to enumerate the configurations, construct and optimize CE model, and fit the calculated DFT energies. For hcp and bcc Ti-Nb systems, various configurations containing at most 4 hcp Ti and 6 bcc Nb unit cells with Nb and Ti atoms random ordering over the substitutional sites were enumerated, respectively. The symmetric uniqueness of each configuration is also guaranteed by applying the scale factor matrix to the parent lattice vectors in the configuration enumeration process [132]. The initial lattice constants that were imposed by scale factor for the hcp and bcc Ti-Nb system are a=2.9508 Å and c=4.6855 Å and a=b=c=3.3079 Å, respectively. The input lattice constants of the hcp Ti-Nb system remain the same as those in the hcp Ti-O system, this is because the hcp Ti-O and Ti-Nb binary structures can be used as a starting point to construct the cluster expansion model for the hcp Ti-Nb-O ternary system where can only identify the structures with the same initial lattice constants. All the Monte Carlo simulations were performed using the *emc*2 code in ATAT with the input of cluster expansion Hamiltonians in order to compute the thermodynamics of different phases over compositions and temperatures.

The generalized gradient approximation parameterised in PAW-PBE method [108] was used to describe the exchange-correlation functional in DFT calculations. The PAW potentials of Ti_sv with 12 valence electrons and Nb_sv with 6 valence electrons, suggested in the VASP manual, were employed to treat valence states for the configurations in both hcp and bcc Ti-Nb systems. Energy cutoff of 400 eV and 8000 k-points per reciprocal atom were identified sufficiently to achieve good DFT calculation convergence, namely less than 1 meV, for all the Ti-Nb configurations in these two systems. Each structure was first fully relaxed with ion positions relaxing using a conjugate-gradient method, then a static calculation was performed to reach the structural convergence criteria and ensure residual forces on each atom less than 0.001 eV/Å. An energy convergence criteria of 10^{-7} eV was applied to the electronic self-consistent loops, namely the calculation stopped when the total energy difference of the adjacent two steps was lower than 10^{-7} eV. The second-order Methfessel-Paxton scheme [155] with the smearing width of 0.2 eV was employed to treat the partial occupancy for relaxation calculations, while the tetrahedron method [156] was used for static calculations. For both hcp and bcc Ti-Nb systems, all the calculations were performed with non-spin polarization due to no magnetism existing in Ti and Nb.

5.1 ground-states characteristics

166 and 266 configurations were enumerated in total in the range of Nb concentration from 0 to 1 to search the ground states and construct a good converged CE model. However, unlike oxygen, Nb is a strong β stabilizer that can introduce mechanical instability into hcp Ti [189]. Specifically, for the hcp Ti-Nb system, many configurations relaxed too far from the ideal hcp crystal, with some transforming to bcc. CNA methods were performed for each structure, it shows that 20 structures relaxed to bcc or other geometries. To accurately determine the applicability of each structure to the CE model, we calculated the distortion (RA) of all the 166 structures based on the changes in lattice parameters before and after relaxation ((3.26)and(3.27)), as shown in

Figure 5.1(a). A total of 42 % of the 166 enumerated structures were excluded (all red marks). As it can be seen, the higher the Nb content of a structure, the higher the possibility that its RA is larger than 0.1. A total of 92 % of those over-relaxed structures (RA > 0.1) have Nb concentration larger than 50 %, and 80 % of the structures that relax to bcc or other geometries (red triangle) have RA above 0.1. As a result, 97 structures were left to construct the hcp TiNb CE, and the CV score was reduced from 19.1 meV/atom to 5.03 meV/atom before and after excluding the unstable structures.

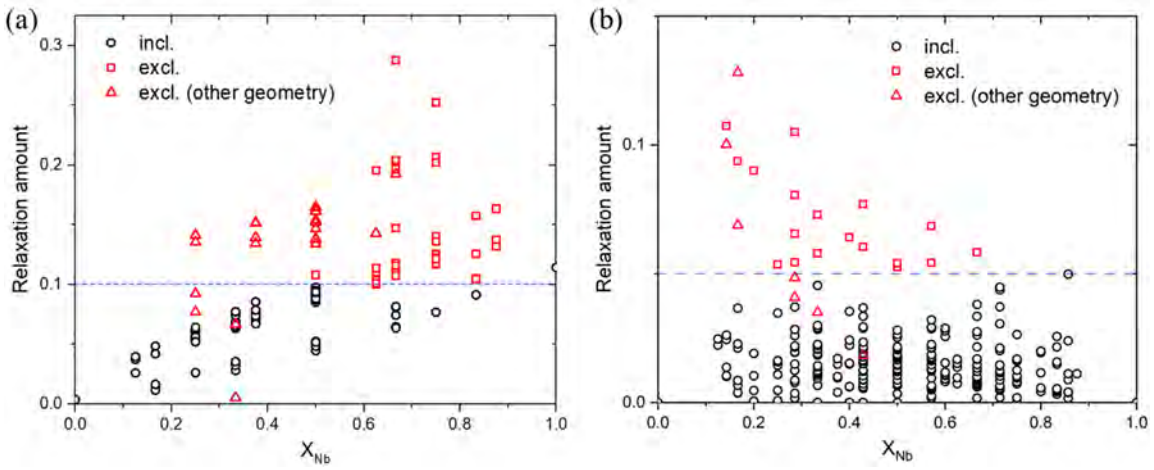

Figure 5.1: Distortion of (a) the 166 structures in the hcp Ti-Nb system and (b) the 266 structures in the bcc Ti-Nb system.

Due to the different parent crystal lattices of Ti and Nb, it is expected that it is hard to accommodate each other between the two. This can also be reflected from Figure 1.5, where it indicates that at 0 K, Nb has no solubility in αTi, and Ti has very narrow solubility in βNb. However, in our work, it is surprising that, compared to the hcp system, the structures in the bcc Ti-Nb system exhibit smaller distortion, resulting in a higher stability of the system. As shown in Figure 5.1(b), the RA values of all the enumerated structures in the bcc system are below 0.15, with only four structures having RA values greater than 0.1. To obtain the most predictive CE model while capturing various Ti-Nb interactions as much as possible, all structures that relaxed to other geometries (red triangles) and structures with RA values greater than 0.05 (red squares) were excluded from the construction of the CE model. It can be seen that among all the excluded structures, only 4 % have an Nb content greater than 50 %, indicating that the bcc Ti-Nb system

exhibits higher stability when the Nb concentration exceeds 50 %. In addition, 43 % of the structures that relaxed to other symmetries have RA values greater than 0.05. For all structures with RA values less than 0.05, their Nb content spans the entire range from 0 to 1, unlike the hcp Ti-Nb system, which shows a trend of an increase in RA values with the increasing content of the element that does not have the hcp parent lattice. This objectively reveals that the bcc lattice has a stronger ability to accommodate Ti atoms compared to the ability of the hcp lattice to accommodate Nb atoms, resulting in more stabilities in bcc Ti-Nb systems. As a result, 241 configurations were used to construct the bcc TiNb CE, and the CV score was reduced from 4.89 meV to 2.59 meV before and after removing these unstable structures from the construction of the CE model.

Then we calculated the E_f of each structure in the hcp and bcc Ti-Nb system using the calculated DFT total energy and normalizing it to the reference states (pure αTi and βNb) by:

$$E_f = \frac{E_{tot} - mE_{\alpha Ti} - nE_{\beta Nb}}{m+n} \tag{5.1}$$

where E_{tot} is the total energy of a configuration $\alpha Ti_m Nb_n$ or $\beta Ti_m Nb_n$ in the hcp or bcc Ti-Nb system which has m Ti atoms and n Nb atoms. $E_{\alpha Ti}$ and $E_{\beta Nb}$ are the total energy per atom of the two end members for the hcp and bcc system. Thus, the E_f of these two end members are zero, and the E_f of all the other structures expresses the energy difference between it and the reference states. The DFT calculated E_f of all the enumerated configurations in the hcp and bcc system are shown in Figure 5.2(a) and (b), respectively, with Nb concentration taken as the x-axis. It can be seen that most structures fall in the convex hull in both two systems, and the E_f of 23 % (22 structures) of the 97 structures in the hcp system is above the dashed line, while in the bcc system, only 10 % (25 structures) of the 241 structures have the E_f above the dashed line. In addition, the E_f of all structures in the hcp system fall within the range of 0-0.3 eV/atom and the E_f of the structures with the Nb concentration larger than 0.5 are further from the convex hull, indicating the introduction of stronger mechanical instability. However, the E_f of all structures in the bcc system are within the range of 0.1 eV/atom, which indicates that, at

0 K, the structures and ordered phases in the bcc system are more stable in energetics than in the hcp system. It is also obvious that a compound having stoichiometry TiNb with orthorhombic Pmmn is predicted to be a ground-state, the inset of Figure 5.2(a) shows its crystal structure. In the bcc system, more stable ground states were found on the convex hull, they are Ti_6Nb, Ti_3Nb, Ti_2Nb, Ti_4Nb_3 and Nb_2Ti. It is worth noting that the E_f of these 5 ground-state structures are close, making the convex hull line, plotted by connecting these 5 E_f points, appear more concave. This differs from the hcp Ti-O and hcp Ti-Nb systems, where the ground states with intermediate compositions have the lowest E_f, resulting in the convex hull line with a distinctly convex peak around the middle. The crystal structures and lattice parameters of these 5 ground states are shown in Figure 5.3 and Table 5.1, respectively. Both the ground-states Ti_6Nb and Nb_2Ti belong to the trigonal crystal system but have two different space groups namely $R\bar{3}$ and $P\bar{3}m1$ symmetry, respectively. Furthermore, the lattice parameters of Ti_6Nb show that exhibit characteristics where $a = b = c$ and α=β=γ< 120°, which can be described by the rhombohedral (primitive) cell of the trigonal crystal system. The ground-state Nb_2Ti has the lattice parameters of $a = b \neq c$, α=β=90° and γ=120°, which can be represented by the hexagonal (R-centered) cell of the trigonal crystal system. Besides, the ground-states Ti_3Nb, Ti_2Nb, Ti_4Nb_3 all belong to the monoclinic crystal system. Both Ti_3Nb and Ti_2Nb share the same space group of P2/m, with the lattice parameters of $a \neq b \neq c$, α=γ=90° and $\beta \neq 120°$. Ti_4Nb_3, however, has the space group of Cm and the characteristics of lattice parameters $a = b \neq c$ and α=$\beta \neq \gamma \neq 90°$.

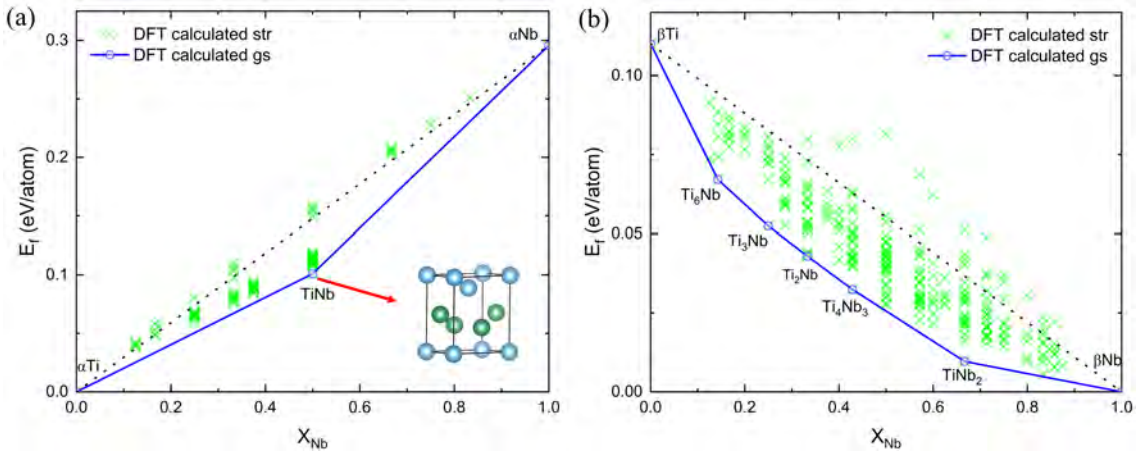

Figure 5.2: DFT Calculated formation energies (E_f) of the enumerated structures in (a) hcp and (b) bcc Ti-Nb system, the DFT ground-state orderings are connected as convex hull.

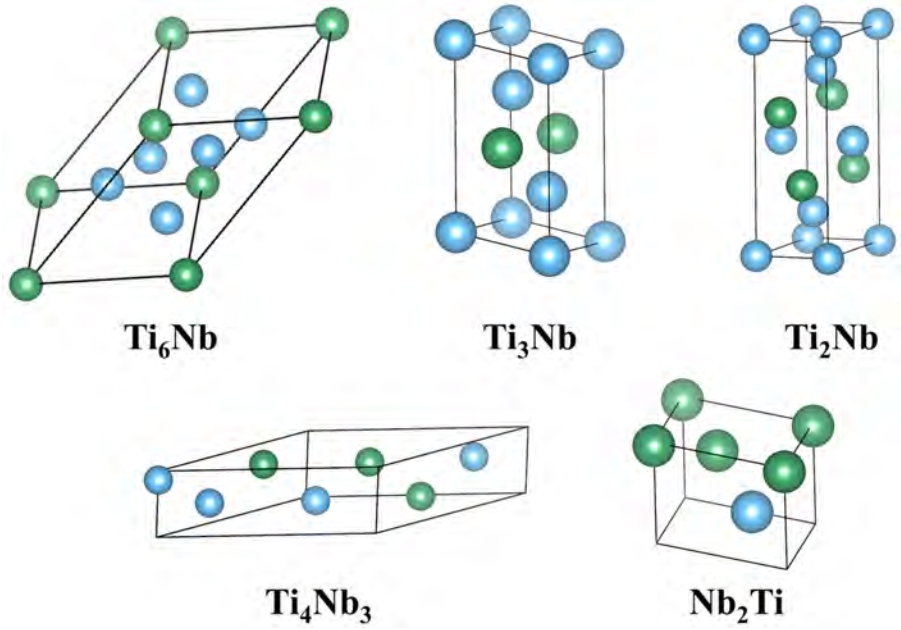

Figure 5.3: Crystal structures of the 5 ground states in the bcc Ti-Nb system. All these ground states belong to the bcc lattice system, because the symmetry operations in the factor group are used to enumerate only the symmetrically unique configurations.

Table 5.1: Lattice parameters of the ground states found in bcc Ti-Nb system.

Ground-state	Structure	Space group	a(Å)	b(Å)	c(Å)	$\alpha(^\circ)$	$\beta(^\circ)$	$\gamma(^\circ)$
Ti_6Nb	trigonal	$R\bar{3}$	7.068	7.068	7.068	118.23	118.23	118.23
Ti_3Nb	monoclinic	P2/m	2.855	4.568	5.439	90	102.11	90
Ti_2Nb	monoclinic	P2/m	2.851	4.606	7.949	90	88.97	90
Ti_4Nb_3	monoclinic	Cm	9.698	9.698	2.856	96.59	96.59	27.36
$TiNb_2$	trigonal	$P\bar{3}m1/m$	4.627	4.627	2.862	90	90	120

The constructed CE models for the hcp and bcc systems by excluding those highly distorted structures (red marks in Figure 5.1) were then optimized and verified. The DFT calculated and CE fitted E_f of the enumerated structures in hcp and bcc system are shown Figure 5.4(a) and (b) respectively, it is evident that all the data points are along or near the line y=x, indicating that the DFT calculated E_f are well reproduced by the constructed CE model for both two systems. Figure 5.4(c) and (d) show the residuals of the CE fit of the structures in the hcp and bcc system,

respectively. For the hcp Ti-Nb system, the E_f residuals for all the 97 structures are acceptable, the largest residual of 8.13 meV/atom appears at a point outside the convex hull with the Nb content of 50 %. Compared to the hcp system, as shown in Figure 5.4(d), the E_f residuals of the bcc Ti-Nb system are smaller than those in the hcp system and closer to the line y=0, the biggest residual is 6.23 meV/atom. For both hcp and bcc systems, most residuals are within 5 meV/atom, to be specific, 90 % and 98 % fitting residuals in the hcp and bcc system are less than 5 meV/atom, respectively. The weighted CV scores of 2.59 meV/atom and 1.71 meV/atom, which is much lower than that reported by Chinnappan *et al*. [44], were obtained by assigning higher weights to structures closer to the convex hull in the hcp and bcc systems, respectively.

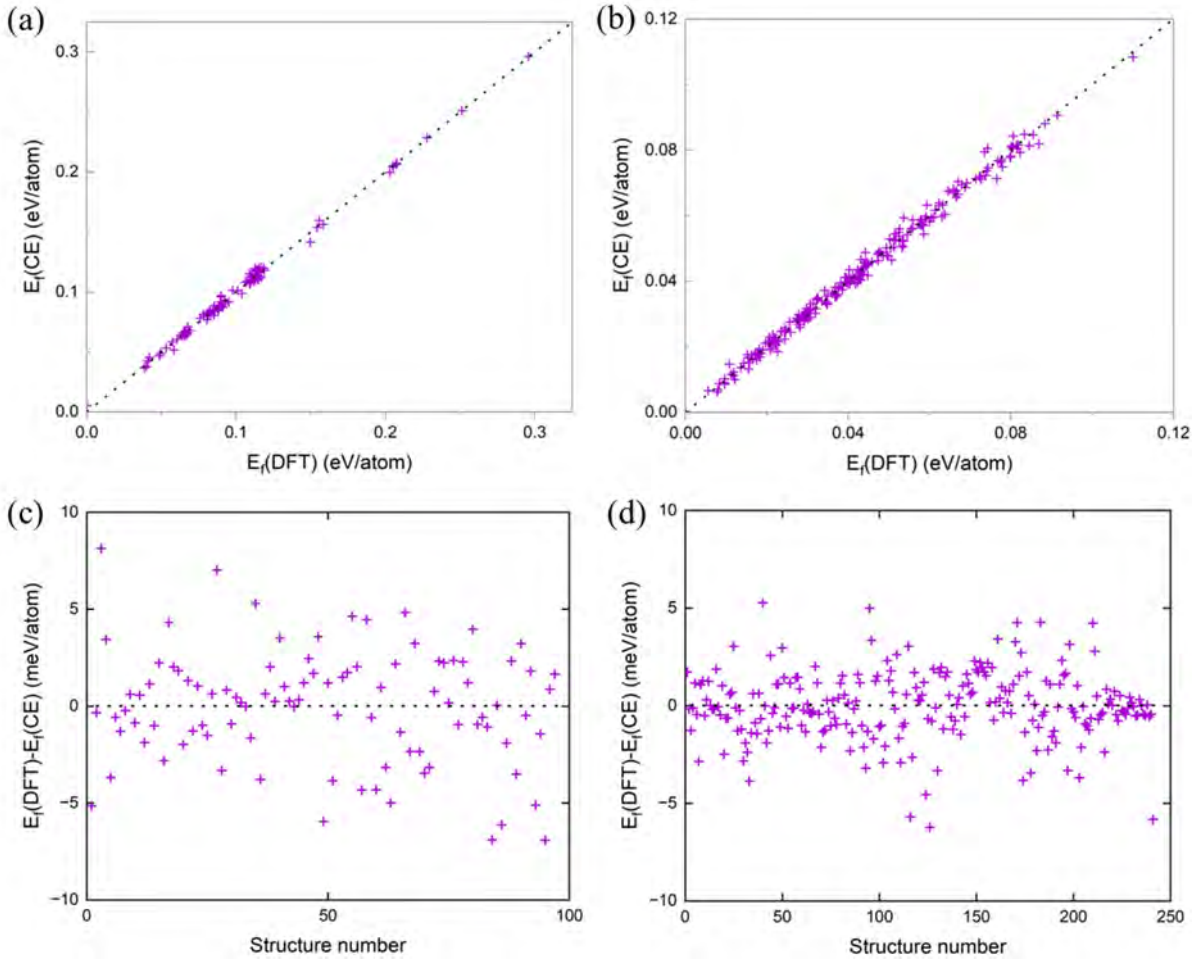

Figure 5.4: The DFT and CE fitted E_f of the structures in (a) hcp and (b) bcc Ti-Nb system and the residuals of CE fit of the (c) hcp and (d) bcc system.

The optimized clusters for the hcp Ti-Nb system include 13 pairs, 15 triplets and 10 quadruplets and their ECIs are illustrated in Figure 5.5(a). The largest value for pairwise and triple-wise

ECIs in this CE appearing at the cluster diameter of 5.1 Å and 2.946 Å respectively is about 10 meV which is much lower than that for pairwise (139.9 meV) calculated in hcp TiO CE. In addition, the values of some ECIs in triplets and quadruplets are comparable to those in pairs at cluster diameter around 5 Å, indicating there are some non-negligible complex Ti-Nb interactions in this system. We note that the magnitude of ECIs decays with the increase in the number of sites contained, as generally expected. The optimized clusters for the bcc TiNb CE, consisting of 20 pairs, 20 triplets and 20 quadruplets are shown in Figure 5.5(b). Compared to the ECIs discovered in the hcp TiNb CE, the ECIs for the bcc TiNb CE are smaller and converge better with the increase in the number of sites that clusters contain, the largest value of ECIs appearing at the cluster diameter of 3.3 Å of a pair is 4.4 meV which is much lower than the maximum in the hcp TiNb CE. This reflects that, the Ti-Nb interactions in the hcp Ti-Nb system are stronger than those in the bcc Ti-Nb system.

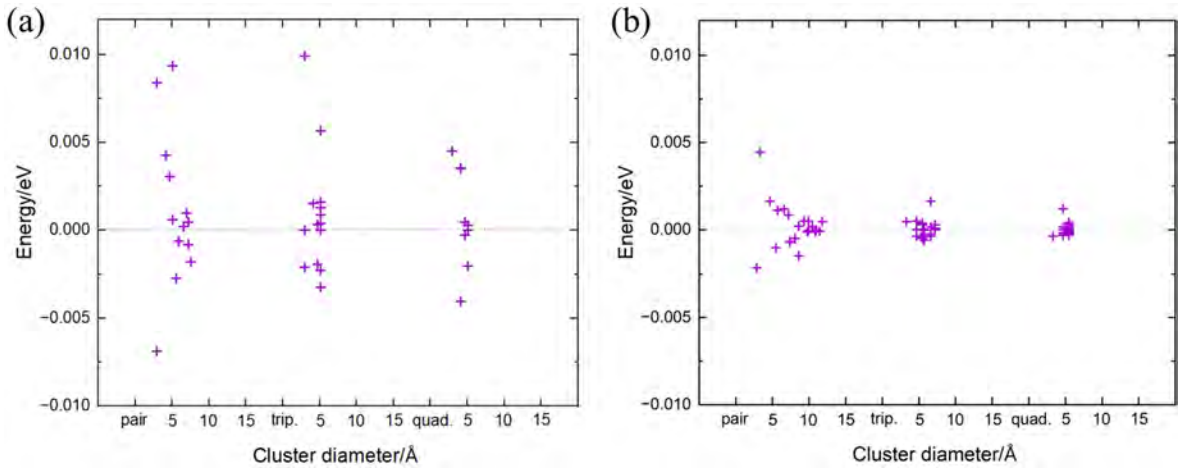

Figure 5.5: The effective cluster interactions (ECIs) of (a) the 13 pairs, 15 triplets and 10 quadruplets in hcp TiNb CE and (b) the 20 pairs, 20 triplets and 20 quadruplets in bcc TiNb CE.

Our finding that, compared to the addition of Ti to bcc Nb, adding Nb to hcp Ti can introduce more mechanical instabilities since DFT calculations indicate more structures in the hcp TiNb system present larger RA and distortion, is contrary to that found by Chinnappan *et al*. [44]. This discrepancy may be due to the smaller number of structures calculated in the Chinnappan study and the different calculation settings used in this study. To be specific, in their DFT calculations of hcp TiNb system, the larger convergence criteria (10^{-4}eV) set for the electronic

self-consistent loop results in some structures maintaining the metastable hcp crystal structure. Different PAW potentials were also used, which leads to small differences in formation energies for some structures. In this study, we opted to use the Ti_sv and Nb_sv potentials, which respectively treat 12 and 13 electrons as valence electrons. This leads, for instance, to the formation energy of TiNb to be 6.8 meV/atom higher than when using Ti_pv and Nb_pv.

5.2 Electronic structure analysis of the ground states

In order to clearly understand the underlying physical mechanism of the energetics and the Ti-Nb interactions in the hcp and bcc Ti-Nb systems, electronic structure calculations are powerful tools to provide us with deep insights into these physical observations such as the bonding characteristics of Ti and Nb in hcp and bcc crystal cells. For the hcp Ti-Nb system, the total and projected DOS of the ground-state TiNb and pure Ti are shown in Figure 5.6, to reveal trends, the DOS of Ti_3Nb and $TiNb_3$ with the lowest E_f at their respective composition are also plotted. We can see, from Figure 5.6(a), that the addition of Nb into hcp Ti parent cell changes the overall shape of each total density of states (TDOS), and it is more evident with the increase of Nb concentration. The TDOS of ground-state TiNb exhibits fewer sharp peaks than pure Ti, indicating stronger metallic bonding present in TiNb thereby a lower obtained E_f. This trend was also captured by Zhou *et al*. [91] although their study investigated this using special quasi-random structures [122, 190]. For the ground-state TiNb, the *d* orbitals of both Ti and Nb contribute to the electronic states of the bonds, whereas anti-bonding was dominated by Ti *d* orbitals alone, implying that the repulsion interaction between the nuclei is mainly caused by Ti. The *d* orbitals of the ground-state TiNb can be split into three separate directional groups, namely d_{xy} and $d_{x^2-y^2}$, d_{yz} and d_{xz}, and d_{z^2} [191]. The d_{xy} and $d_{x^2-y^2}$ orbitals, lying on the $x-y$ plane, facilitate the bonding between the nearest neighbor Ti and Nb atom within the closed-packed plane. The d_{yz} and d_{xz} orbitals, vertical to the $x-y$ plane, promote the hybridization of the Ti and Nb atoms on the $x-y$ plane with those nearest neighbor atoms sitting on the adjacent $x-y$

planes. The d_{z^2} orbitals with lobes pointing along the z axis are responsible for the interactions between atoms on the $x-y$ plane and their second neighbor along the z direction, however this interaction is weaker than that of the first two groups. This can also be confirmed from Figure 5.6(b), the contribution to PDOS by d_{xy} and $d_{x^2-y^2}$ orbitals are comparable to that by d_{yz} and d_{xz} orbitals, both of which are greater than that of the d_{z^2} orbitals, although the electron states of all these three groups spread over the entire energy interval around E_{Fermi}.

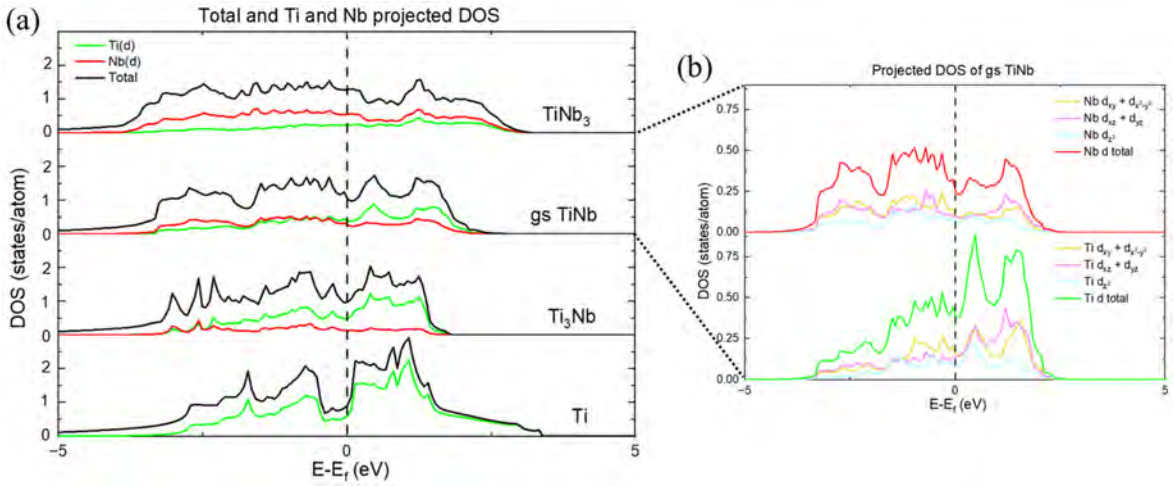

Figure 5.6: (a) DOS of the pure Ti, ground-state TiNb and ordered Ti_3Nb and $TiNb_3$; (b) Projected DOS of the ground-state TiNb in the hcp Ti-Nb system.

For the ground states in the bcc Ti-Nb system, the calculated total DOS and the projected DOS of Ti and Nb d orbitals are shown in Figure 5.7, similar to the hcp Ti-Nb system, the addition of Ti into the bcc Nb lattice cell also changes the shape of each TDOS. Specifically, the electronic states at around 4 eV in pure bcc Nb do not appear in the DOS of all the ground states and the electronic states around the E_{Fermi} gradually represent the characteristics of the d orbitals of Ti. Furthermore, the addition of Ti leads to an increase in the number of TDOS peaks around the E_{Fermi} and a decrease in the number of sharp TDOS peaks, especially for the ground-state Ti_4Nb_3, which has the largest number of low peaks around the E_{Fermi}. This indicates that, when Ti and Nb are mixed in the bcc lattice cells and the concentration of Ti is close to 50 %, the electronic states below the E_{Fermi} will be distributed across more energy levels. It is also can be seen that, above the E_{Fermi}, the electronic states are mainly contributed by the Ti d orbitals, which reflects that the anti-bonding effects and repulsion interaction between nuclei in the bcc

system are also dominated by Ti atoms. From the projected DOS of Ti and Nb d orbitals, we can conclude that the bonding effects appearing in all the ground states are caused by the hybridization between Ti and Nb d orbitals. The hybridization in the ground-states Ti_6Nb, Ti_3Nb and Ti_2Nb are predominantly contributed by the Ti d orbitals, and the contribution from Nb d orbitals becomes less and less with the increase of Ti content. For instance, the Nb d orbitals contribute very little near the E_{Fermi} in the ground-state Ti_6Nb, whereas the Ti d orbitals contribute few around the E_{Fermi} in the ground-state $TiNb_2$. It is worth noting that, for the ground-state Ti_4Nb_3 in which the peaks near the E_{Fermi} are the broadest, the contributions of the electronic states from both Ti and Nb d orbitals are balanced, indicating strong Ti-Nb interactions and complex hybridizations existed in this ground-state. On the other hand, it is well known that the TDOS at the E_{Fermi} affects electrical conductivity and other electronic properties [192–194]. In the hcp Ti-Nb system, as shown in Figure 5.6(a), the TDOS at the E_{Fermi} in these compounds increases with the rise of the Nb content, namely TDOS from 0.92 states/atom to 1.27 states/atom as the Nb concentration from 0 to 0.75. This means the electrical conductivity of these compounds increases when the Nb concentration changes from 0 to 0.75. Nevertheless, for the bcc Ti-Nb system, this trend is not observed in these ground states, that is to say, there is no obvious increase or decrease in the electrical conductivity when Nb content changes. We can also see that the TDOS at the E_{Fermi} in pure bcc Nb (Figure 5.7) is larger than that in pure hcp Ti (Figure 5.6(a)), which demonstrates the fact that Nb has a higher electrical conductivity than Ti.

Figure 5.8 shows the projected DOS of each sub-orbital of the Ti and Nb d orbitals, which helps us further understand the bonding characteristics of these ground states in the bcc Ti-Nb system more specifically. It can be observed that in all ground states, the electron states near the Fermi level resulting from the hybridization of d orbitals between Ti and Nb are mainly contributed by d_{xy} and $d_{x^2-y^2}$, and d_{xz} and d_{yz} orbitals. These orbitals are responsible not only for the interactions between nearest neighbor Ti and Nb atoms within the same $x-y$ plane but also for bonding between nearest neighbor Ti and Nb atoms in adjacent $x-y$ plane. The d_{xz} and d_{yz} orbitals in both Ti and Nb contribute the most to the electron states near the Fermi

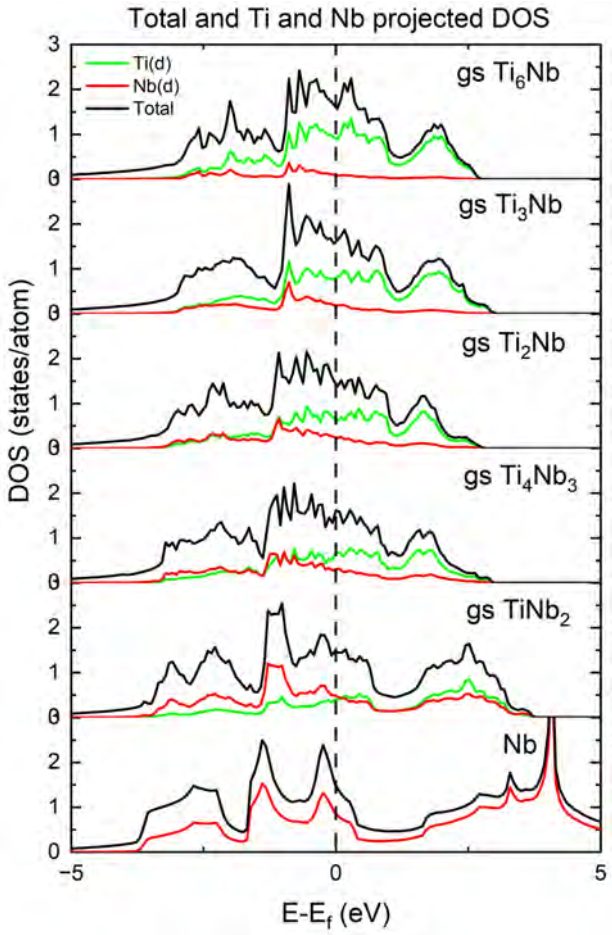

Figure 5.7: Total DOS and the projected DOS of Ti and Nb d orbitals of the ground states in the bcc Ti-Nb system.

level after hybridization, slightly more than the d_{xy} and $d_{x^2-y^2}$ orbitals. This indicates that the hybridization between the $d_{xz} + d_{yz}$ orbitals of Ti and Nb is predominant, followed by the $d_{xy} + d_{x^2-y^2}$ orbitals. The d_{z^2} orbitals contribute very little to the electron states near and below the Fermi level but significantly contribute to the electron states above the Fermi level at around 2.5 eV. This suggests that the d_{z^2} orbitals mainly promote the formation of electron states of anti-bonding between Ti and Nb, contributing little to the formation of metallic bonds. The gain and loss of each atom in each ground-state in the bcc and hcp Ti-Nb systems are then evaluated by performing the Bader analysis, as shown in Table 5.2. It can been seen that, in all the ground states, Nb atoms gain electrons, while Ti atoms lose electrons, and the average number of electrons gained by each Nb atom increases with the Ti concentration. For all the ground states, only the number of electrons gained by each Nb atom in the ground-state Ti_4Nb_3

is different, and only each Ti atom in the ground-state Ti_6Nb lose the same number of electrons. The number of electrons gained and lost between Ti and Nb in the ground-state TiNb in the hcp Ti-Nb system is similar to that in the ground-state Ti_4Nb_3 in the bcc system, which is related to the similar Nb concentrations in both ground states, indicating that when the Nb concentration is close to 50 %, the electron localization around Ti and Nb atoms in these two Ti-Nb systems is similar. Compared to the electron transfer between Ti and Nb in the Ti-Nb system, the number of electrons gained and lost between O and Ti in the ground states in the hcp Ti-O system is higher, indicating a higher degree of electron localization in the ground states in the hcp Ti-O system.

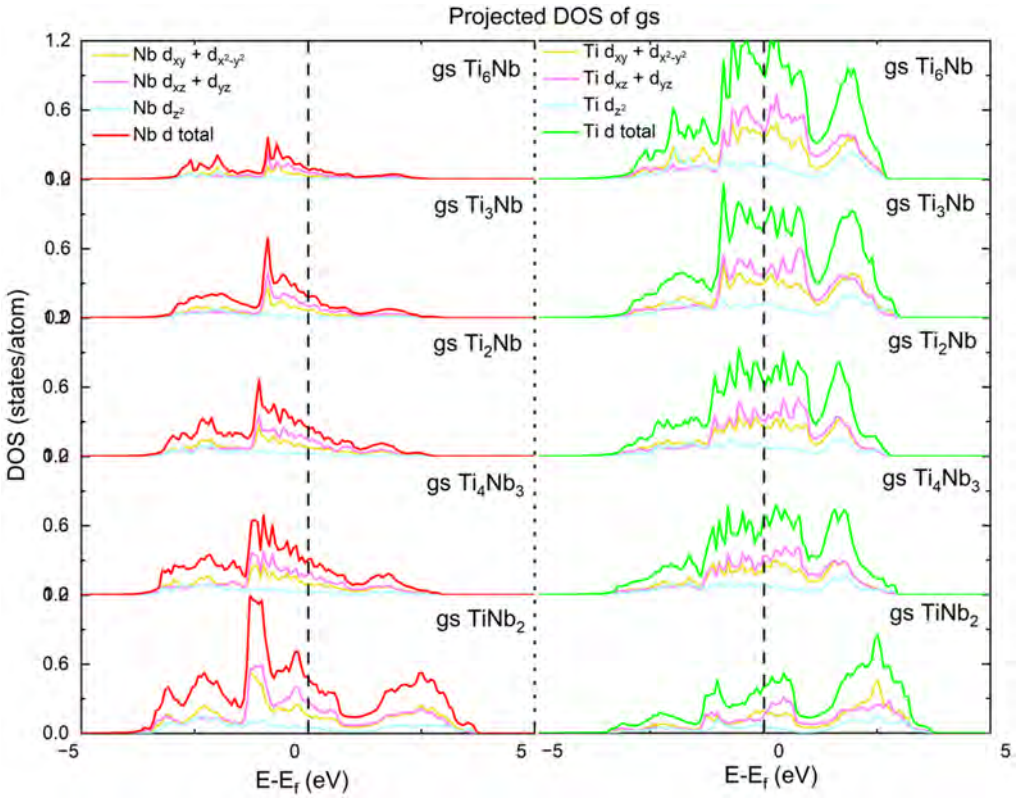

Figure 5.8: Projected DOS of each sub-orbital of the Ti and Nb *d* orbitals of the ground states in the bcc Ti-Nb system.

Table 5.2: Gain and loss of electrons of each Nb and Ti atom in the bcc and hcp Ti-Nb ground states via Bader analysis.

Ground-state	Nb atoms	Ti atoms
Ti_6Nb	+1.136	-0.189, -0.189, -0.189, -0.189, -0.189, -0.189
Ti_3Nb	+1.102	-0.332, -0.332, -0.439
Ti_2Nb	+0.866, +0.87	-0.751, -0.205, -0.571, -0.21
Ti_4Nb_3	+0.359, +0.929, +0.65	-0.532, -0.827, -0.106, -0.473
$TiNb_2$	+0.436, +0.436	-0.871
TiNb(hcp)	+0.664, +0.664	-0.664, -0.664

5.3 Vibrational and thermodynamic properties of the ground states

In order to evaluate the vibrational properties and thermal expansions of these ground states in the hcp and bcc Ti-Nb system, the Debye-Grüneisen model was applied to account for both harmonic and anharmonic effects in the vibrational properties of Ti-Nb system. At first, a set of E-V data points of the ground states were computed by performing full relaxation in DFT calculations, followed by fitting these data points to the zero-order Birch–Murnaghan equation of state. The original E-V points and the fitted E-V curve of all the ground states found in the hcp and bcc Ti-Nb system are shown in Figure 5.9, where the point in each sub graph with the lowest total energy corresponds to the state that the corresponding ground-state is at its equilibrium volume. All the other total energy data points in each sub plot correspond to the states having cell volumes that fall within 5 % contraction or expansion of the equilibrium cell volume. This can be achieved by adjusting the scaling factor of the lattice parameters. It is evident that all the E-V data points of the hcp and bcc ground states are situated on the fitting line of Birch–Murnaghan equation of state, there is no outlier of DFT data. These E-V data were

then used to calculate the vibrational and thermodynamic properties at different temperatures.

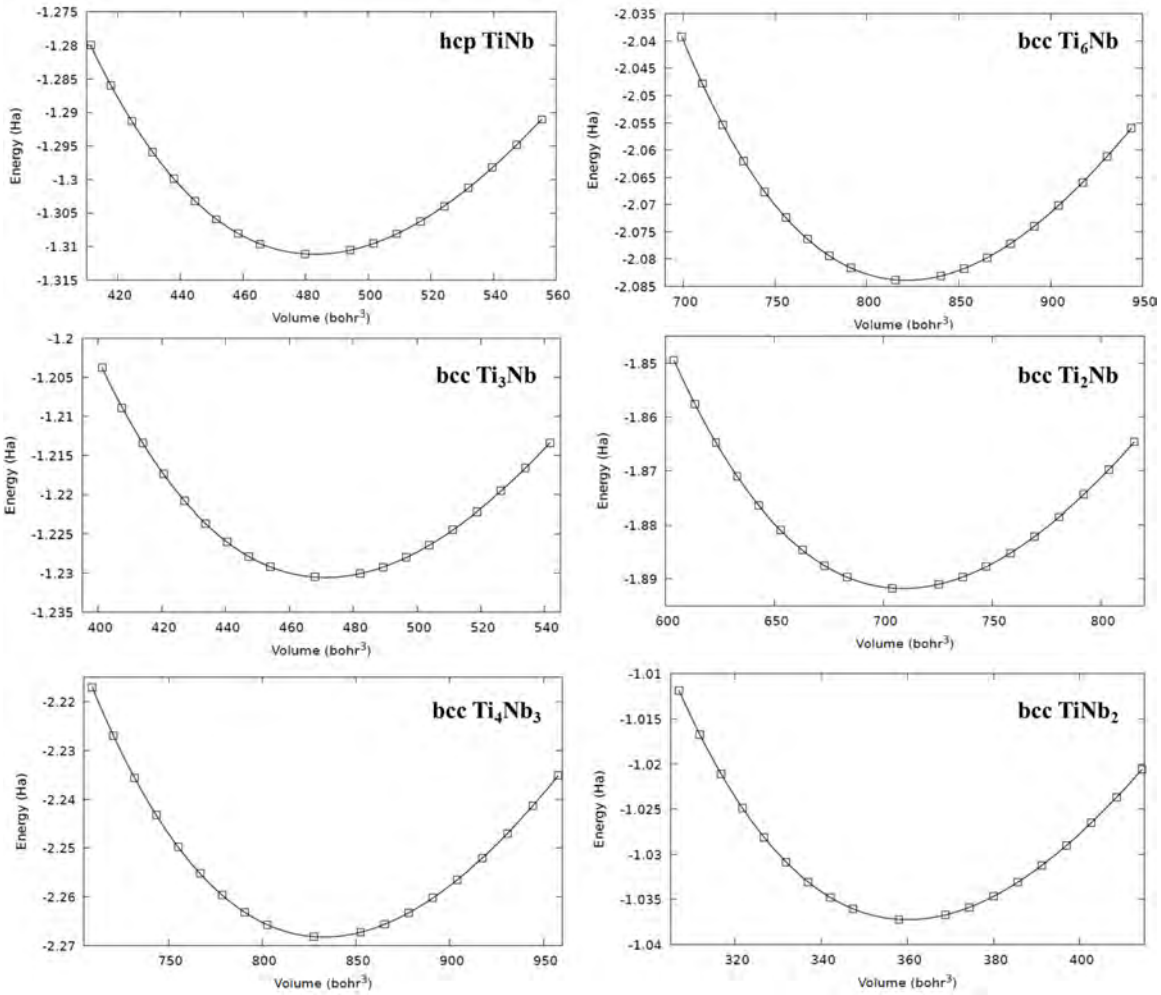

Figure 5.9: E-V data and the fitted curve of all the ground states in the hcp and bcc Ti-Nb system.

Figure 5.10 shows, in the hcp Ti-Nb system, the calculated total F_{vib} of the pure Ti unit cell, the structure with the lowest E_f at X_{Nb}=0.25, and the ground-state TiNb at different temperatures. It can be seen that for the pure Ti, the calculated F_{vib} at low temperatures has a very small difference compared to the results calculated by Zhou *et al*. [54], and this discrepancy gradually increases with the increase in temperature, reaching 84 meV/Ti at 1000 K, though this discrepancy is not large in numerical terms. For the Ti_3Nb, which has the lowest E_f at X_{Nb}=0.25, our data is very close to that obtained by Zhou, with the discrepancy varying little with temperature and reaching 27 meV/Ti at 1000 K. For the ground-state TiNb, our calculated F_{vib} at low temperatures shows a little difference (~80 meV/Ti) from the data reported by Zhou, while this difference gradually drops with rising temperature, achieving 34 meV/Ti at 1000 K. The calculated total F_{vib} for the

bcc Ti-Nb system is shown in Figure 5.11, with the data reported by Zhou plotted as scatter. Similar to the results for pure Ti in the hcp system, the calculated F_{vib} of bcc pure Nb diverges increasingly from Zhou's data as the temperature rises, reaching a difference of 109 meV/Ti at 1000 K, and also exhibits the lowest F_{vib} over almost the entire temperature range. In addition, except for the ground-state $TiNb_2$, the F_{vib} of other ground states are comparable below 400 K. For all the ground states, as the Nb content increases, F_{vib} decreases more rapidly with increasing temperature above 400 K. For both hcp and bcc systems, the discrepancy between our data and that reported by Zhou *et al*. could be mainly due to that, all the supercells used in their study are created by employing the special quasirandom structure (SQS) model [195, 196] and have 128 atoms in total, with different number of solute atoms randomly distributed on the substitutional sites in the supercells. However, all the structures used in the F_{vib} calculation in this study are the ground states that are on the E_f convex hull and those that are close to the E_f convex hull. The supercells generated by the SQS model have random atomic arrangements and can only represent the disordered α and β phases in the Ti-Nb system. In contrast, our work is to search for stable ordered phases and ground states by the combination of DFT calculation with the CE model. Clearly, in general, at the same composition, disordered structures have more possible vibrational modes than ordered structures [197, 198]. Therefore, the entropy change (Δ S) in disordered structures is greater than in ordered structures, which results in a lower F_{vib}, as observed from Figures 5.10 and 5.11.

The calculated linear thermal expansion (LTE) of all the ground states in the hcp and bcc Ti-Nb system are shown in Figure 5.12, the data for the pure hcp Ti, hcp Ti_3Nb with the lowest E_f at its composition and pure bcc Nb are plotted for comparison. It shows that the LTE of all the ground states rapidly increases in the temperature range of 0 – 600 K, and then increases slowly with the further rise of temperature. It can also be observed that, for both the hcp and bcc Ti-Nb systems, the LTE of the structures increases with the increase in Nb content. Moreover, Ti_3Nb and Ti_2Nb in the bcc system exhibit similar LTE curves, which may be attributed to the close proximity of their Nb concentrations. The calculated static bulk modulus of the ground states in both of these two systems is shown in Figure 5.13, with the data for the structures closest to

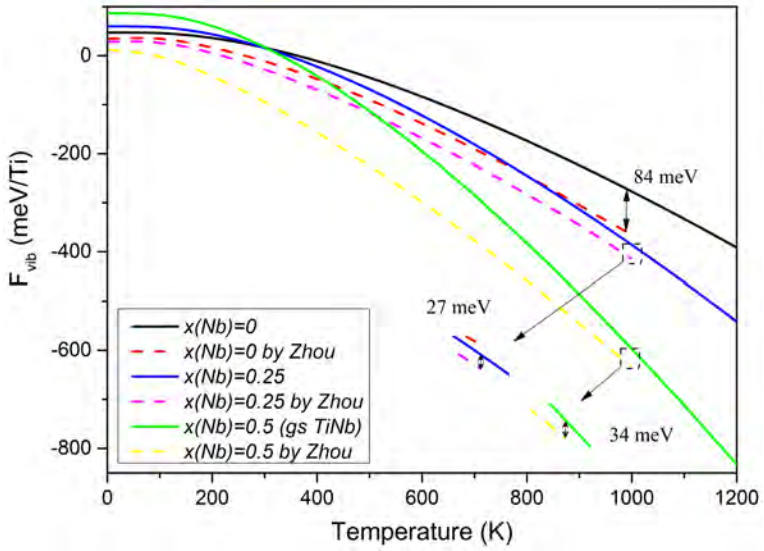

Figure 5.10: The calculated F_{vib} of the pure Ti, ordered Ti_3Nb and the ground-state TiNb in the hcp Ti-Nb system, the data calculated using SQS method by Zhou *et al*. [54] were plotted with dashed lines.

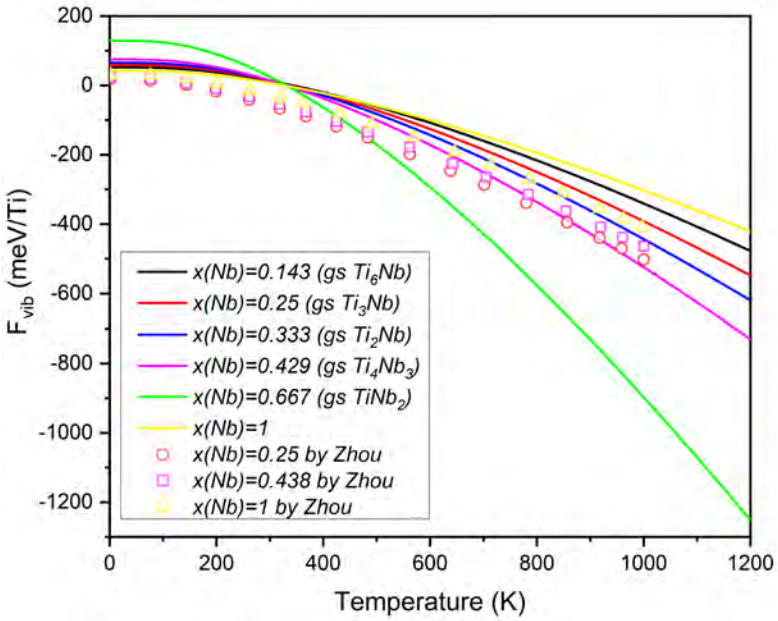

Figure 5.11: The calculated F_{vib} of the pure Nb, the ground-state Ti_6Nb, Ti_3Nb, Ti_2Nb, Ti_4Nb_3 and $TiNb_2$ in the hcp Ti-Nb system, the data calculated using SQS method by Zhou *et al*. [54] were plotted with scatter.

the convex hull at various compositions plotted for observing the overall trend. Obviously, the hcp and bcc Ti-Nb systems have close values and similar change trends for the bulk modulus, especially at X_{Nb}=0.5, where the difference in bulk modulus is only 1.2 GPa. This indicated that the atomic interactions in both the hcp and bcc Ti-Nb systems are similar and the bonding

strength and nature of atomic forces in these two systems are also comparable. Besides, our calculation results agree well with those obtained by Zhou *et al*. [54] using the SQS model, especially for the hcp system, where the differences are minimal. This reflects that the model we established by combining DFT calculation and CE methods can predict the static bulk modulus of the disordered phase in the Ti-Nb system, even though we used the ordered structure with the lowest E_f at the respective composition. However, compared to our work and Zhou's study, the data reported by Zhang *et al*. [199] using the coherent potential approximate (CPA) slightly underestimated the bulk modulus of both systems, which is probably because CPA ignores the local lattice distortion. Although the vibrational, mechanical, and thermodynamic properties of the Ti-Nb system calculated using ordered structures in this work cannot truly represent the properties of disordered α and β phases, they can still provide a quick initial prediction of properties for these disordered phases.

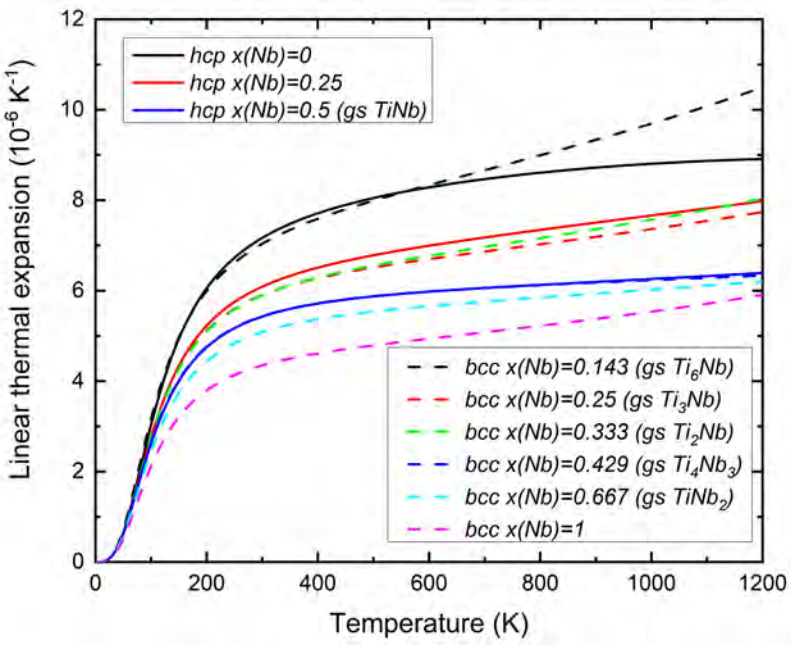

Figure 5.12: The linear thermal expansion (LTE) of the ground states, pure Ti, ordered Ti_3Nb in the hcp Ti-Nb system (solid lines), and the ground states, pure Nb in the bcc Ti-Nb system (dashed lines).

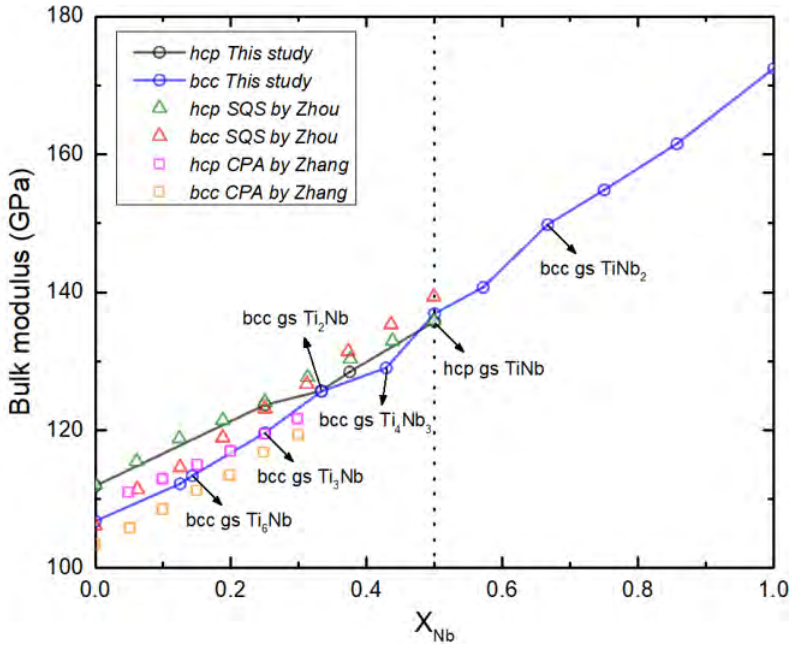

Figure 5.13: The static bulk modulus of the ground states and some ordered structures in the hcp and bcc Ti-Nb system, triangle scatter and square scatter are the data reported by Zhou *et al*. [54] and Zhang *et al*. [199] using SQS and CPA method, respectively.

5.4 Finite temperature phase stability

To evaluate the thermodynamics of the ground states across the compositions and temperatures, the semi-grand canonical Monte Carlo simulations were performed to get the thermodynamic quantities versus composition and temperature. For the inclusion of the vibrational entropy, for both hcp and bcc Ti-Nb systems, the F_{vib} of the structures of which E_f are close to the convex hull of hcp and bcc CE was calculated to construct a vibrational CE to obtain the vibrational ECIs (fvib ECIs) which will then be added to the ECIs obtained using configurational free energy to get the temperature-dependent ECIs (tECIs). The tECIs can be used as new Hamiltonian inputs into Monte Carlo simulations to calculate the changes in thermodynamic quantities after considering vibrational entropy. First, we performed a series of Monte Carlo simulations for all the ground states found in both hcp and bcc systems, however, all of them turn to be unstable and disordered at lower temperatures ($10 - 40$ K), it is unnecessary to discuss their order-disorder transition temperature and thermodynamic quantities. Here, in order to verify the precision of the constructed CE for both two systems, the phase boundaries between the disordered α and β

phases were examined. The computed phase boundaries between α and β phase in the Ti-Nb system are shown in Figure 5.14. As can be seen, compared with αTi-O ordered phases, the vibrational free energy has a greater impact on the phase boundaries in the Ti-Nb system, and significantly reduces the phase transition temperature, which is also observed in the Ti-V and Ti-Ta systems [44]. It is well-known that the vibrational entropy always reduces the transition temperatures in most metallic systems [181]. Our calculated phase boundaries with the inclusion of F_{vib} are more consistent with the experimental data reported by Kumar *et al*. [200], especially in the Ti and Nb rich region.

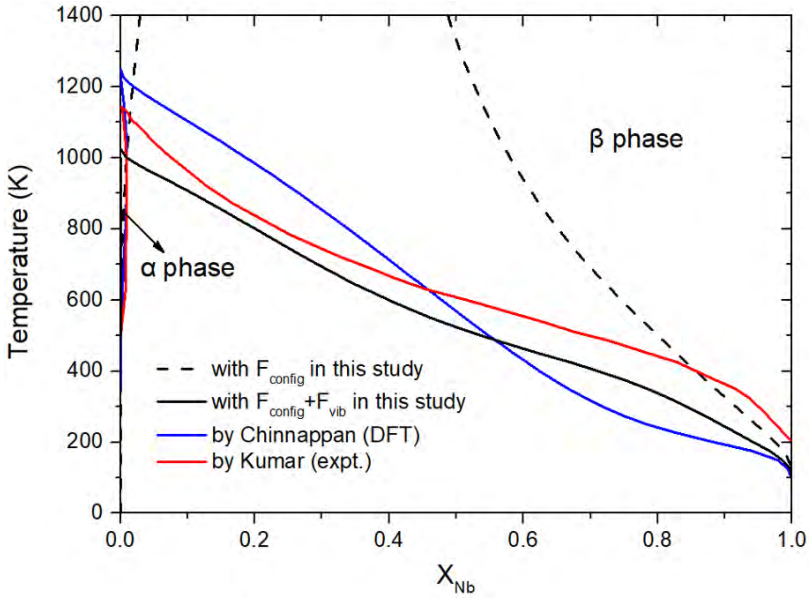

Figure 5.14: Phase boundaries between α and β phase in the Ti-Nb system, DFT results and experimental data calculated by Chinnappan *et al*. [44] and Kumar *et al*. [200] are shown as blue lines and red lines, respectively.

5.5 Summary

In this chapter, we calculated the E_f of a series of hcp and bcc Ti_xNb_{1-x} structures by DFT calculations. However, we analyzed relaxation and the number of nearest-neighbor atoms for each structure using RA calculation ((3.26) and (3.27)) and the CNA method, finding that, unlike the hcp Ti-O system, both systems contain highly distorted structures. Our results show that

the hcp Ti-Nb system has more highly distorted structures compared to the bcc Ti-Nb system, indicating more mechanical instability existed in the hcp system. This is contrary to the findings reported by Chinnappan *et al*. [44], which can be attributed to their training set containing fewer structures and their DFT calculations not fully relaxing the structures, thereby leaving some metastable and unstable structures in the systems. Then, we removed these identified highly distorted and over-relaxed structures from the CE, resulting in the construction of the predictive CE models for the hcp and bcc systems. The constructed CE models can accurately predict the E_f of all the structures in both systems, respectively, thus effectively expressing the energetics of the systems. Although the ECIs of the clusters in both systems are converged, compared to the bcc system, a few stronger ECIs in pairs and triplets are present in the hcp system. This also objectively reflects the relative stability of these two systems. From the two E_f convex hull diagrams, we identified a total of six ground-state structures: TiNb in the hcp system, and Ti_6Nb, Ti_3Nb, Ti_2Nb, Ti_4Nb_3 and Nb_2Ti in the bcc system. We then analyzed the density of states of these six ground states and found that the bonding characteristics of metallic bonds are similar within the two systems. The strength of the metallic bonds is related to the hybridization degree between the d orbitals of Ti and Nb atoms, especially the hybridization of $d_{xy} + d_{x^2-y^2}$ and $d_{xz} + d_{yz}$ orbitals.

Subsequently, we calculated the thermodynamic properties of these ground-state structures at constant composition and different temperatures, including F_{vib} and LTE. We found that, for most ground states, our results showed some discrepancy with those obtained using the SQS method reported in the literature. However, this discrepancy is acceptable since there should be thermodynamic differences between ordered and disordered structures. These differences can ultimately be attributed to the varying strengths of interatomic interactions brought about by the ordered and disordered nature of atomic arrangements at different temperatures, resulting in differences in E_f. Surprisingly, the performance of these ordered ground states in certain static mechanical properties (such as bulk modulus) is very close to the mechanical properties of corresponding compositional disordered structures calculated using the SQS method in the literature. This provides a new approach for predicting the mechanical and thermodynamic

properties of disordered structures using ordered structures. In the end, we calculated the phase stability of all the ground states over various compositions and temperatures through Monte Carlo simulations. It is found that these ordered ground states decompose into disordered hcp or bcc phases at very low temperatures. To verify the accuracy of our DFT and CE models, the phase stabilities of the disordered α and β phases were then computed and the effect of vibrational entropy on their stabilities was also examined. It is observed that the inclusion of vibrational entropy significantly reduces the phase transition temperature of the α and β phase, this effect was also captured in the Ti-V and Ti-Ta systems reported in the literature. In addition, our computed phase boundaries between α and β phase are consistent with experimental results.

Chapter 6

Hcp and Bcc Ti-Nb-O system

Compared to the binary Ti-O and Ti-Nb systems studied in the previous chapters, reports on the thermodynamic data of ordered and disordered phases in the Ti-Nb-O ternary system are very scarce [201]. To efficiently construct and well optimize the cluster expansion models for the Ti-Nb-O ternary systems, the structures used in the hcp Ti-O and hcp Ti-Nb CE, as well as the structures used in the bcc Ti-Nb CE, were thereby employed to train the CE models for the hcp Ti-Nb-O system and the bcc Ti-Nb-O system, respectively. We only investigate the Ti-rich and Nb-rich regions in the hcp and bcc ternary systems, respectively, since this study focuses on the hcp and bcc phases that appeared in the Ti-Nb-O system. All the DFT total energies of the enumerated structures and the electronic structures of the ternary ground states were calculated by VASP. The *mmaps* code implemented in ATAT was used to enumerate ternary ordered structures, train the CE models, and fit the DFT energies. For both hcp and bcc ternary systems, the size of the enumerated symmetric unique supercells was limited to within 25 hcp Ti and bcc Nb unit cells, respectively. The initial lattice constants of these two ternary systems remain consistent with those of the hcp and bcc binary systems described in the previous two chapters. The *memc*2 code in ATAT [202] which is the multicomponent version of the *emc*2 was used to perform Monte Carlo simulations by employing the cluster expansion Hamiltonians as the input in order to obtain the thermodynamic quantities of the ordered and disordered versus

compositions and temperatures. The exchange-correlation functional in all the DFT calculations were described by the GGA which is parameterised in PAW_PBE method [108]. The valence states for all the structures in the ternary systems were treated by the PAW potentials of Ti_sv with 12 valence electrons, Nb_sv with 6 valence electrons and O with 6 valence electrons. Energy cutoff of 550 eV and 8000 k-points per reciprocal atom were tested large enough to achieve good convergence (within 1 meV in total energy) of DFT calculations for the ternary structures in both hcp and bcc ternary systems. Similar to the binary systems, each structure in the ternary systems also underwent full relaxation calculation first using the conjugate-gradient method [203], then a static calculation was followed to achieve the structural convergence criteria and ensure the residual forces on each atom less than 0.001 eV/Å. The total energy convergence criteria of 10^{-7} eV was imposed on the electronic self-consistent loops in both full relaxation calculation and static calculation of each structure. The second-order Methfessel-Paxton scheme [155] with the smearing width of 0.2 eV and the tetrahedron method [156] were employed to treat the partial occupancy for relaxation calculations and static calculations, respectively. For both two ternary systems, all the DFT calculations were performed with non-spin polarization.

6.1 ground-states characteristics

In order to efficiently construct the CE model for the hcp Ti-Nb-O system, all the 236 and 97 structures used in the hcp Ti-O and hcp Ti-Nb systems were employed as a starting point to enumerate structures for the hcp ternary system. The 241 structures used in the bcc Ti-Nb system were employed to start the enumeration of the structures in the bcc ternary system. The hcp Nb-O, bcc Ti-O systems are unstable at 0 K, therefore it is impossible to construct the CE model for these two systems. Also, for the bcc Nb-O system, we also found most of the structures relaxed away from the ideal bcc structure, thus we only included the stable 8 Nb-O binary structures into the CE construction for the bcc ternary system. After the above steps, a total of 926 and 703 configurations were, respectively, included in the hcp and bcc Ti-Nb-O

systems, including all the binary structures used in the CE models of the binary systems. Then, we performed CNA for each structure and found that 105 and 283 structures in the hcp and bcc ternary system, respectively, relax away from the ideal hcp and bcc crystal structure to other geometries. Hence, all these structures were removed from the construction of the CE models for the ternary systems. Based on the changes in lattice vectors before and after relaxation, we calculated the distortion of the remaining 821 and 420 configurations in the hcp and bcc ternary systems, respectively, by using the Equations (3.26) and (3.27). As shown in Figure 6.1(a), there are only two ternary structures in the hcp Ti-Nb-O system with RA values greater than 0.15 (red dots). Both of these two structures have an oxygen content of 33.3 at.%, which is the solubility limit of oxygen in the hcp lattice, and their chemical formulas are Ti_5NbO_3 and $Ti_4Nb_2O_3$, respectively. Besides, there are 16 ternary structures with RA values between 0.1 and 0.15 (yellow dots), accounting for 3.5 % of all ternary structures. Among these, 13 structures have an oxygen content of 33.3 at.%, while the remaining 3 structures have an oxygen content below 12 at.%. It also can be seen that the majority of the ternary structures have RA values below 0.1, indicating that most of the hcp ternary structures are stable. As described in Chapter 5, the addition of Nb to hcp Ti cells introduces significant mechanical instability to the system. However, here, by computing the lattice distortions of the hcp ternary structures, we found that the addition of oxygen to the hcp TiNb structures significantly reduces the distortion effect, thereby improving the mechanical stability of the system. This can be attributed to the fact that the instabilities introduced by the β stabilizers can be counteracted or mitigated by the addition of oxygen which is one of the strong α stabilizers. Figure 6.1(b) shows the distortion values of all structures in the bcc ternary system. It can be seen that, compared to the hcp ternary system, there are more structures with high RA values in the bcc ternary system. The maximum distortion value is 0.57, which is 3.8 times the maximum distortion value (0.15) in the hcp ternary system. Specifically, there are 16 ternary structures in the bcc ternary system with RA values greater than 0.2, and 37 ternary structures with RA values between 0.1 and 0.2, accounting for 15.1 % and 34.9 % of the total bcc ternary structures, respectively. In addition, the oxygen content of all the ternary structures having RA values larger than 0.2 is higher than

13.8 at.%. It is obvious that the RA values of the ternary structures tend to go up with the increase in oxygen content, a trend not observed in the hcp ternary structures. Therefore, ternary structures with smaller RA values in the bcc ternary system are concentrated in the Nb-rich region. This also reflects that, compared to the bcc Ti-Nb system, the hcp Ti-Nb system has the capacity to accommodate more oxygen atoms. This finding can also be confirmed by the CNA result which indicates the bcc ternary system has more configurations that relax to other geometries. In view of the above, to better construct the well-converged and good predictive CE models, only the structures with RA values less than 0.15 and 0.2 in the hcp and bcc ternary systems (orange and blue dots in Figure 6.1), respectively, were employed in the construction and optimization of the CE models.

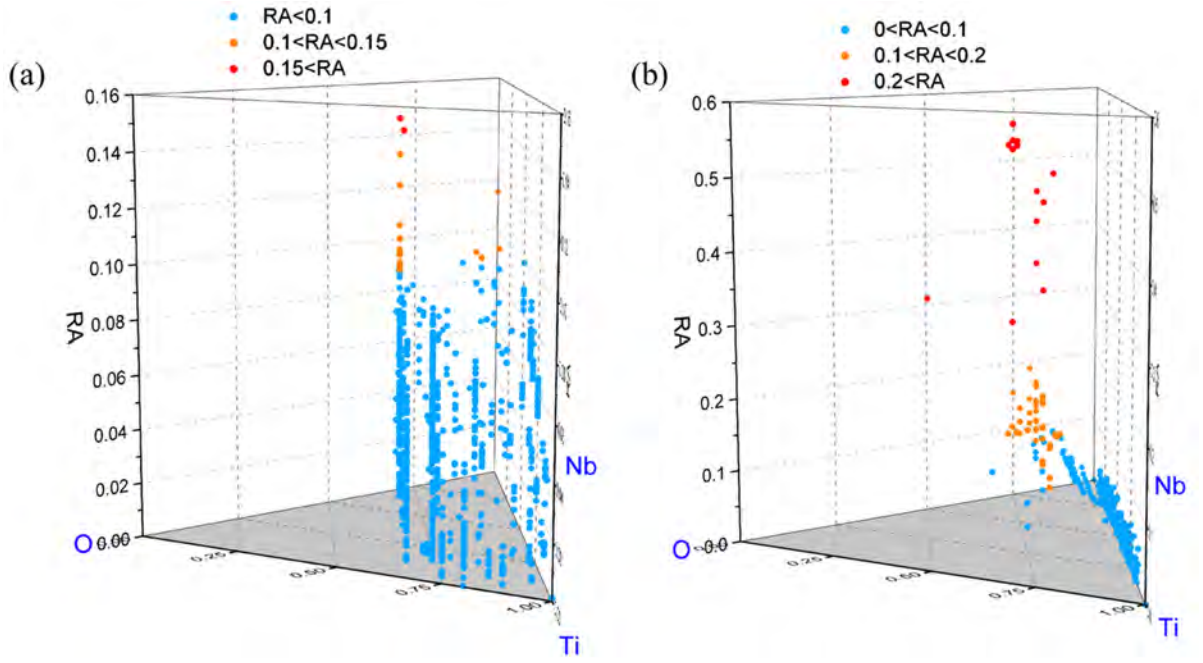

Figure 6.1: Distortion of (a) the 821 structures in the hcp Ti-Nb-O system and (b) the 420 structures in the bcc Ti-Nb-O system.

The E_f of all the structures that were used in the construction of the CE models in the two ternary systems were calculated by taking pure αTi, βNb, single oxygen atom as well as vacancy as reference states:

$$E_f = \frac{E_{tot} - N_{Ti}E_{\alpha Ti} - N_{Nb}E_{\beta Nb} - N_O\frac{1}{2}E_{O_2} - N_{Vac}E_{Vac}}{N_{Ti} + N_{Nb} + N_O + N_{Vac}} \tag{6.1}$$

where E_{tot} is the DFT calculated total energy of a configuration in the ternary systems, $E_{\alpha Ti}$, $E_{\beta Nb}$, E_{O_2} and E_{Vac} are the total energies of pure αTi, pure βNb, oxygen molecule and the vacancy, respectively, where the total energy of vacancy is zero. N_{Ti}, N_{Nb}, N_O, and N_{Vac} represent the number of Ti, Nb, oxygen, and vacancy in the configuration, respectively. Figure 6.2(a) shows the calculated E_f of all the structures used in the CE of the hcp Ti-Nb-O system, it can be seen that only the E_f of the TiNb binary structures and pure hcp Nb are greater than zero, while the E_f of all the TiO binary structures and TiNbO ternary structures are smaller than zero. Among all structures, the binary ground-state Ti_2O has the lowest E_f of -1.55 eV/atom. In addition, the E_f of all ternary structures range between -0.1 and -1.5 eV/atom, with the ground-state Ti_5NbO_3 having the lowest E_f of -1.48 eV/atom, and $Ti_{22}Nb_2O$ having the largest E_f of -0.11 eV/atom. This indicates that ternary structures with dilute oxygen tend to have higher E_f, which can also be confirmed by Figure 6.2(b) that shows the averaged E_f distribution over compositions. It is evident that the E_f of ternary structures exhibits a gradient change with the variation in composition. Specifically, as the oxygen content increases, the E_f decreases, while at the same oxygen content, an increase in Nb content does not significantly affect the E_f. Therefore, it can be seen from the figure that points with the same level of E_f (points with the same color) are distributed horizontally in a linear manner, and as the oxygen content increases, the gradient of E_f changes from cool to warm tones. The E_f convex hull of the structures employed in the bcc Ti-Nb-O system are shown in Figure 6.3(a), similar to the hcp ternary system, only the E_f of the bcc TiNb binary structures are larger than zero, all the ternary structures have the E_f less than zero. However, unlike the hcp ternary system, although the same reference states are taken for calculating E_f in both ternary systems, the E_f of the ternary structures in the bcc ternary system are much higher, ranging from -0.04 to -0.62 eV/atom. The ground-state TiNbO in the ternary structures has the lowest E_f of -0.61 eV/atom, whereas the structure $TiNb_{24}O$, also having diluted oxygen, owns the highest E_f of approximately -0.05 eV/atom. Figure 6.3(b) exhibits the averaged E_f distribution versus compositions for all the structures in the bcc ternary system. Although we can observe similar changes in the E_f gradient as seen in the hcp ternary system, especially in the region with oxygen content below 0.25, it

becomes challenging to obtain more stable ternary structures that can maintain bcc geometry as the oxygen content exceeds 0.25 since most of the ternary structures not included in the figure have significant distortions and relax into other geometries. This also indicates that the bcc ternary system is hard to accommodate more oxygen compared to the hcp ternary system. Therefore, as confirmed in Figure 6.1, the lattice distortions in the hcp ternary structures are relatively smaller. Moreover, it should be pointed out that in the bcc ternary system, even in the low oxygen region, it is also hard to obtain stable ternary structures that can maintain the bcc geometry when the Ti content exceeds 0.5.

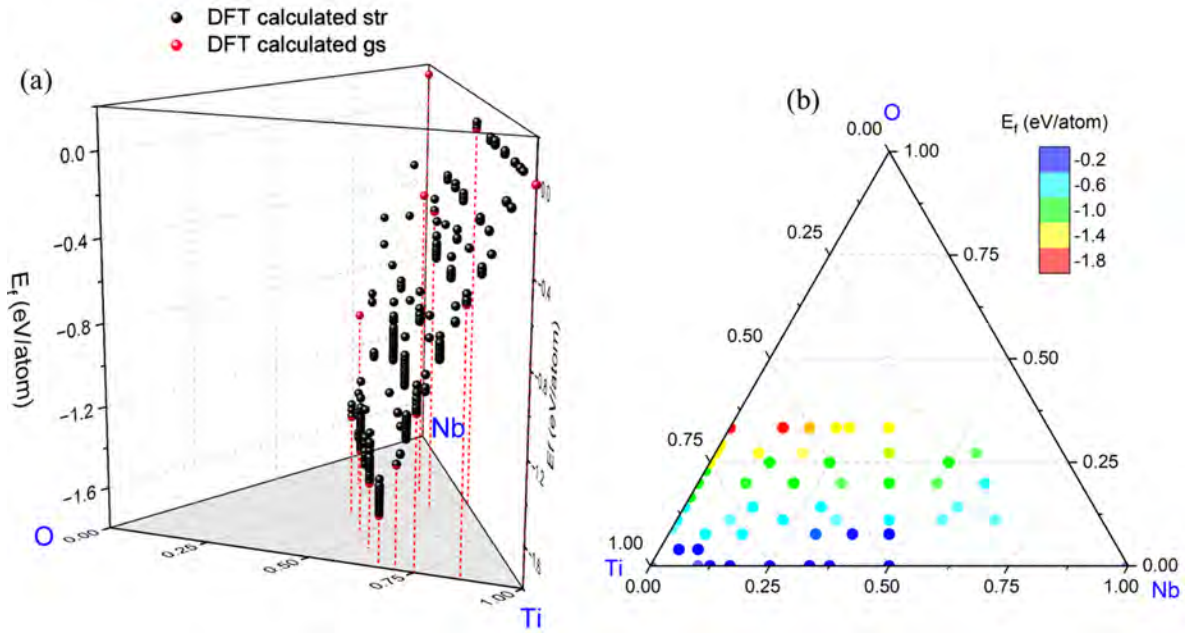

Figure 6.2: (a) DFT calculated E_f of the structures used in the CE in hcp Ti-Nb-O system and (b) E_f distribution versus composition (averaged E_f at each composition) of the structures.

Then, as shown in Figure 6.4, we constructed the 0 K phase equilibrium for the hcp and bcc Ti-Nb-O system, respectively, according to the ground states obtained from the calculated E_f. For both two ternary systems, it is clear that all the binary ground states discovered in the Ti-Nb systems and the hcp Ti-O system are successfully reproduced by the phase stability analysis of the ternary systems. It can be seen from Figure 6.4(a) that, in the hcp ternary system, there are 6 ternary ground states found, i.e. Ti_5NbO_3, $Ti_4Nb_2O_3$, TiNbO, $Ti_2Nb_6O_3$, Ti_4Nb_4O and Ti_3Nb_5O, of which 4 ground states have an Nb content below 0.5, and 2 ground states have an O content below 0.12. The E_f of the ground-state Ti_5NbO_3, $Ti_4Nb_2O_3$, and TiNbO with

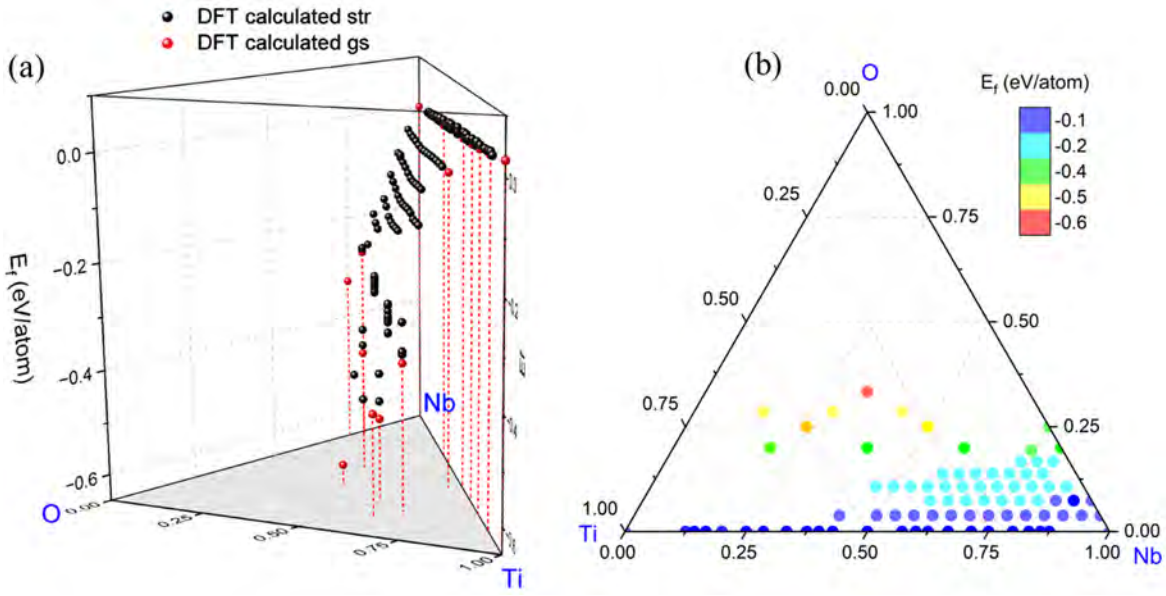

Figure 6.3: (a) DFT calculated E_f of the structures used in the CE in bcc Ti-Nb-O system and (b) E_f distribution versus composition of the structures.

the same oxygen concentration (0.33) are -1.48, -1.41, and -1.32 eV/atom, respectively, which are lower than the E_f of ground-state $Ti_2Nb_6O_3$ at -0.92 eV/atom. These are also lower than the E_f of ground-state Ti_4Nb_4O and Ti_3Nb_5O with an oxygen concentration of 0.11, which are -0.33 and -0.30 eV/atom, respectively. Therefore, these ternary ground states in the hcp system show a gradient decrease on the E_f as the oxygen content increases. In addition, at the same oxygen concentration, the E_f of the ground states increases stepwise with the increase in Nb content. Figure 6.4(b) represents the 0 K phase equilibrium of the ground states in the bcc Ti-Nb-O system, there are also 6 ground states discovered in this system, namely TiNbO, Ti_4NbO_2, Ti_2NbO, $TiNb_2O$, Ti_3NbO and $Ti_{14}Nb_{11}O$. It is surprising that, compared to the hcp ternary system, more ground states found in the bcc ternary system have Ti content larger than 0.5 and an ordering with stoichiometry $Ti_{14}Nb_{11}O$ having diluted oxygen was identified as a ground-state. It can also be observed that, unlike the ground states in the hcp ternary system, the E_f of the ground states in the bcc system decrease stepwise with the increase in solute Ti content. For instance, the Ti content of the ground-state Ti_2NbO is 0.25 higher than that of $TiNb_2O$, while the E_f is 0.07 eV/atom lower.

The lattice parameters of all 6 ground states in the hcp ternary system are shown in Table 6.1,

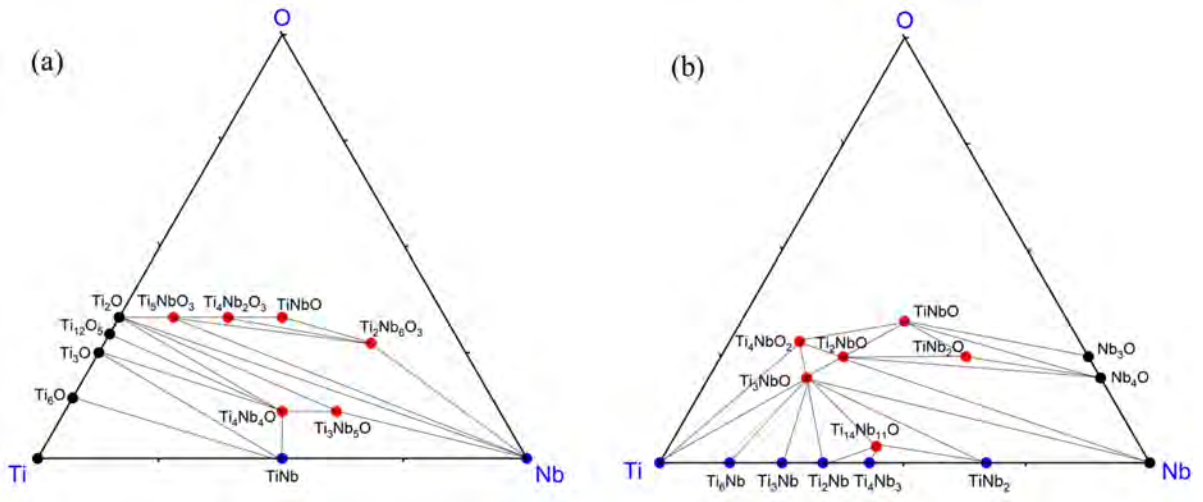

Figure 6.4: The 0 K phase equilibrium in the (a) hcp Ti-Nb-O system and (b) bcc Ti-Nb-O system.

as can be seen, except for the ground-state $Ti_2Nb_6O_3$, which belongs to the triclinic crystal system and features $a \neq b \neq c$ and $\alpha \neq \beta \neq \gamma \neq 90°$, all the other ground states belong to the monoclinic crystal system. Among them, Ti_5NbO_3, $Ti_4Nb_2O_3$, and Ti_3Nb_5O share the same space group Cm and exhibit the characteristic $a = b \neq c$ and $\alpha = \beta \neq \gamma \neq 90°$. The ground-state Ti_4Nb_4O also has the characteristic of $a = b \neq c$ and $\alpha = \beta \neq \gamma \neq 90°$ but belongs to the $C2/m$ space group, whereas the ground-state TiNbO belongs to the $P2_1/c$ space group and features $a \neq b \neq c$ and $\alpha = \gamma = 90° \neq \beta$. The atomic arrangements on different crystal planes of these ground states are presented in Figure 6.5. The arrangements of oxygen atoms in the ground states of $Ti_4Nb_2O_3$ and Ti_5NbO_3 are identical on the (001) and (100) crystal planes. However, Nb atoms are arranged more densely on these planes in the ground-state $Ti_4Nb_2O_3$ than in the ground-state Ti_5NbO_3, with the number of Nb atoms being twice as many. It can also be observed that the distribution of oxygen atoms on the (001) and (100) planes in the ground-states Ti_3Nb_5O and Ti_4Nb_4O is similar, with a tendency to occupy the octahedral sites that neighbor nearest to Ti atoms. The difference lies in the (001) plane, where Nb atoms in Ti_3Nb_5O occupy a layer independently, alternating with Ti atom layers, while in Ti_4Nb_4O, Ti and Nb atoms alternately occupy each layer. Besides, in the ground-state TiNbO, Ti and Nb atoms are alternately distributed on each layer of the (100) and (010) planes, with no separate layers of Ti or Nb atoms. Table 6.2 indicates the lattice parameters of all the ground states in

the bcc ternary system, the ground-states Ti_4NbO_2, Ti_2NbO, $TiNb_2O$ and Ti_3NbO are identified as monoclinic system, while the ground-states TiNbO and $Ti_{14}Nb_{11}O$ are classified as triclinic system. Unlike the hcp ternary ground states, only the bcc Ti_3NbO has the characteristic of $a = b \neq c$ and $\alpha = \beta \neq \gamma \neq 90°$. All the other bcc ground states show the features of $a \neq b \neq c$ and $\alpha \neq \beta \neq \gamma$. Figure 6.6 illustrates the arrangements of the Ti, Nb and oxygen atoms on the different crystal planes in these bcc ternary ground states. Unlike the hcp ternary ground states, for the bcc ground states, only Ti_2NbO and $TiNb_2O$ have similar oxygen arrangements. Specifically, in the (100) plane, adjacent oxygen atom layers are separated by three metal layers, whereas in the (001) plane, separated by two metal layers. All the other ground states show different arrangements of oxygen and metallic atoms, especially the oxygen in the ordering $Ti_{14}Nb_{11}O$ prefers to occupy the octahedral sites in the Ti layers and the oxygen spacing is larger than 5 Å.

Table 6.1: Lattice parameters of the ground states found in hcp Ti-Nb-O system.

Ground-state	Structure	Space group	a(Å)	b(Å)	c(Å)	α(°)	β(°)	γ(°)
Ti_5NbO_3	monoclinic	Cm	5.168	5.189	4.855	88.98	88.98	120.14
$Ti_4Nb_2O_3$	monoclinic	Cm	5.207	5.207	4.899	89.53	89.53	120.22
TiNbO	monoclinic	$P2_1/c$	4.948	5.152	6.11	90	87.93	90
$Ti_2Nb_6O_3$	triclinic	$P\bar{1}$	5.86	5.95	5.991	109.56	105.21	53.31
Ti_4Nb_4O	monoclinic	C2/m	5.508	5.508	10.991	116.83	116.83	29.73
Ti_3Nb_5O	monoclinic	Cm	5.61	5.61	10.997	116.84	116.84	28.82

After excluding all highly distorted structures, we optimized the CE models using the remaining structures in both the hcp and bcc Ti-Nb-O systems. The CV scores of the resulting CE models were 6.69 and 3.55 meV/atom, respectively. Figure 6.7(a) and (b) show the DFT calculated and CE fitted E_f for the hcp and bcc ternary systems, respectively. As can be seen, similar to the binary systems, the data points in both ternary systems are distributed along the y=x

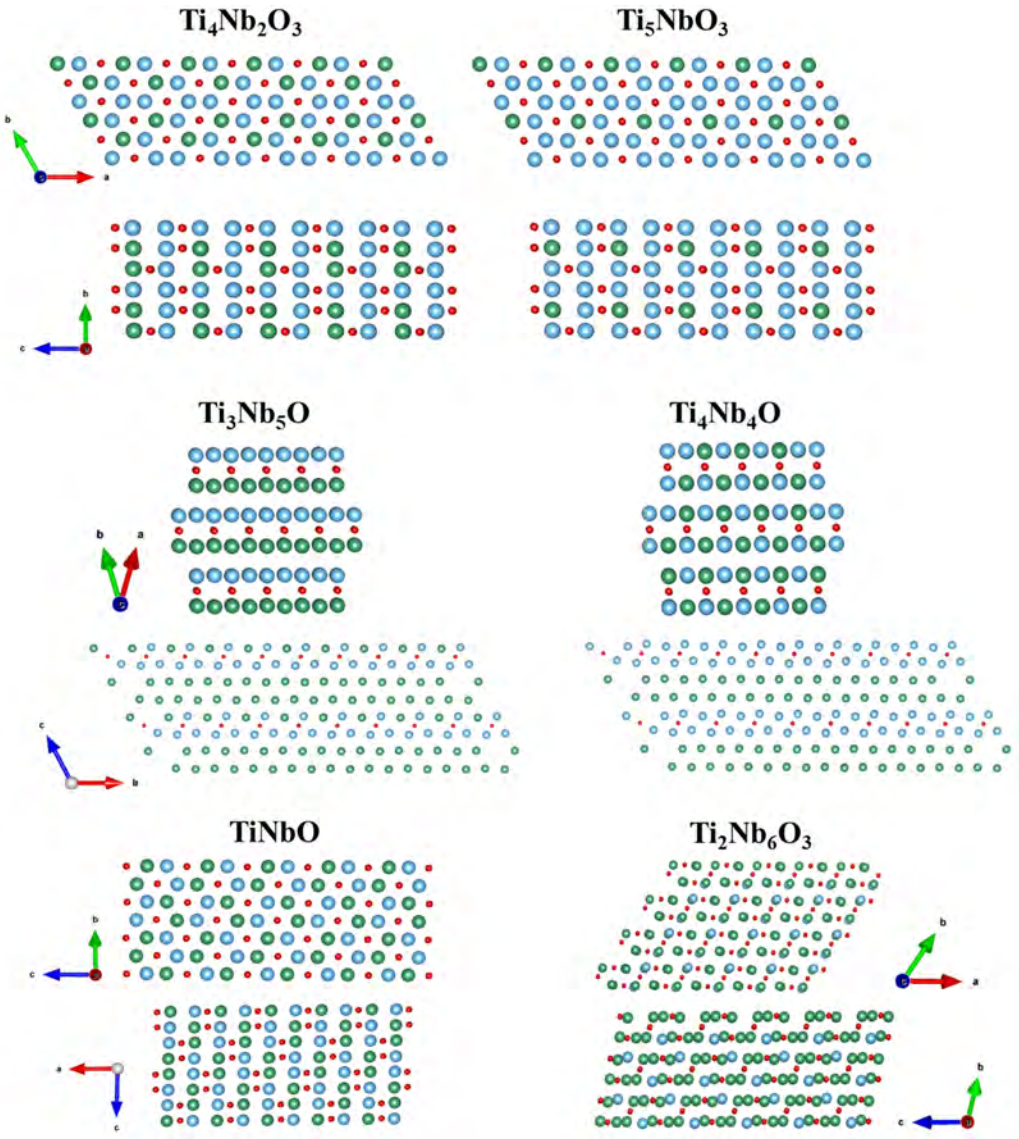

Figure 6.5: The atomic arrangements on different crystal planes of the hcp ternary ground states, blue, green, and red balls are Ti, Nb and oxygen atoms, respectively, the original cells of ground states were transformed to 5×5×5 size for convenient observation.

axis, indicating that the constructed CE models have good predictions. The residuals of the CE fitted E_f of these two systems are shown in Figure 6.7(c) and (d). The maximum residual in the hcp system is 26.2 meV/atom, and 94 % of the structures have a fitting residual lower than 10 meV/atom. In contrast, compared to the hcp system, the residuals of the structures in the bcc system are relatively smaller, with a maximum residual of 10.1 meV/atom, and the fitting residuals of 98 % structures are less than 5 meV/atom. The ECIs of the optimized clusters used in the hcp and bcc ternary systems are depicted in Figure 6.8(a) and (b), respectively. The number

Table 6.2: Lattice parameters of the ground states found in bcc Ti-Nb-O system.

Ground-state	Structure	Space group	a(Å)	b(Å)	c(Å)	$\alpha(^\circ)$	$\beta(^\circ)$	$\gamma(^\circ)$
TiNbO	triclinic	P1	2.98	4.809	5.914	87.55	102.11	85.19
Ti_4NbO_2	monoclinic	Cm	12.597	12.281	3.001	82	77.11	13.78
Ti_2NbO	monoclinic	C2/m	4.766	4.604	2.886	90	90.25	118.88
$TiNb_2O$	monoclinic	Cm	4.899	4.567	2.946	90	97	117.78
Ti_3NbO	monoclinic	C2	5.406	5.406	5.657	116.8	116.8	117.24
$Ti_{14}Nb_{11}O$	triclinic	P1	5.363	5.471	15.232	94.23	94.85	85.88

of the optimized clusters in the hcp system includes 50 pairs, 28 triplets and 6 quadruplets, and it is obvious that the ECIs decay with the increase of cluster diameter which indicates the constructed CE model converges well. The largest ECI value of 137 meV appears at a pair with the cluster diameter of 2.34 Å. For the bcc ternary system, there are totally 60 clusters used in the CE model by optimizing the CV score. The largest ECI of 470 meV also occurs on a pair with same cluster diameter of 2.34 Å, while this value is much higher than that in the hcp system. In addition, the ECIs also converge well with the increase in the cluster diameter, more importantly, most ECIs in the bcc system are larger than the ECIs in the hcp system, reflecting that the cluster interactions in the bcc system are stronger than those in the hcp system [60, 204].

6.2 Electronic structures of the ground states

In order to better understand the effects of oxygen addition on the electronic states, intermetallic interactions, and interactions between metals and oxygen atoms in the Ti-Nb system, we performed electronic structure calculations for the ground states in the hcp and bcc ternary systems. Figures 6.9(a) and (b), respectively, show the contributions of the s and p orbitals of oxygen,

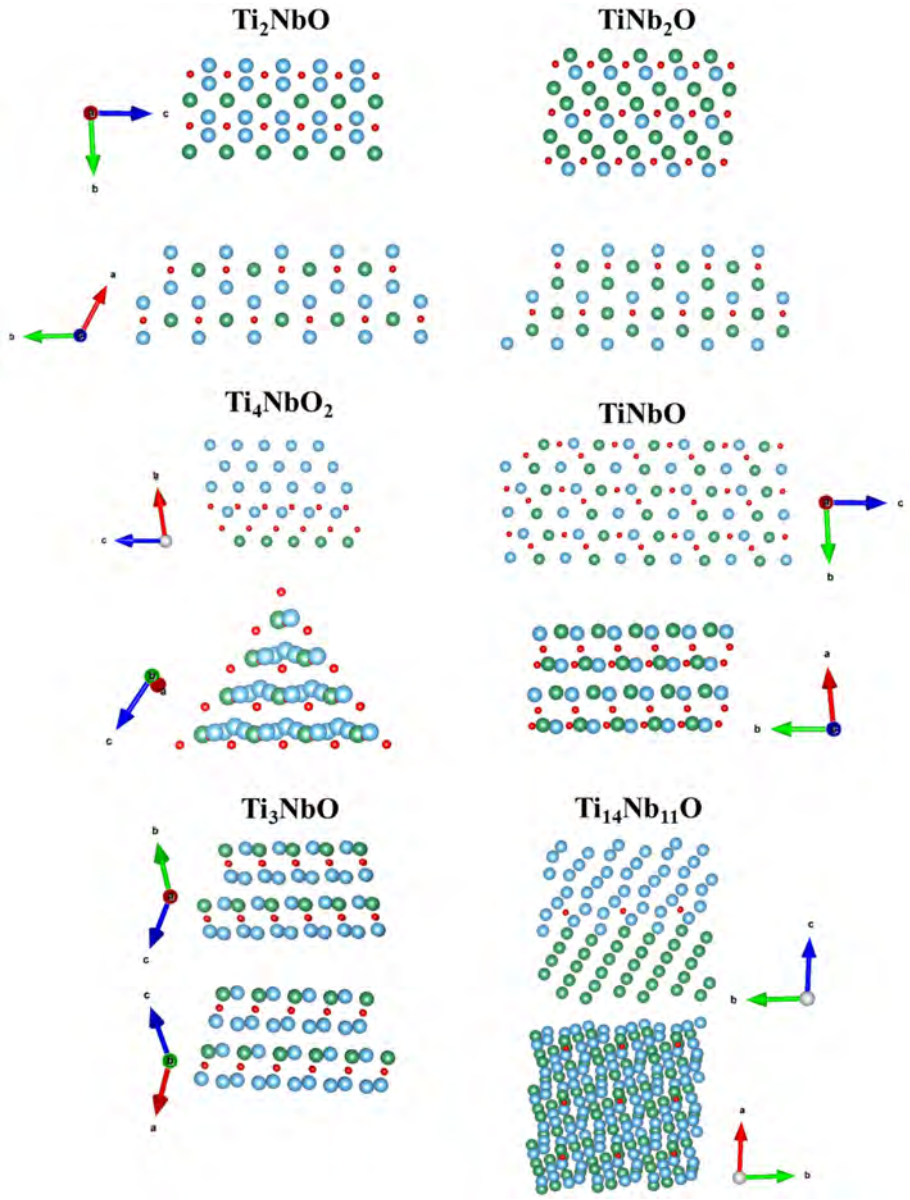

Figure 6.6: The atomic arrangements on different crystal planes of the bcc ternary ground states, blue, green, and red balls are Ti, Nb and oxygen atoms, respectively, the original cells of ground states were also transformed to 5×5×5 size for convenient observation.

as well as the *d* orbitals of Ti and Nb, to the total density of states of the ground states in the hcp ternary system, with normalizing to the Fermi level (black dashed lines). First, it can be observed that the electronic states at the Fermi level for all the ground states are contributed by the *d* orbitals of Ti and Nb, without the involvement of *s* and *p* orbitals of oxygen. This indicates that the hcp ternary system presents the characteristic of the metallic system and the electronic properties of the system are determined by the *d* orbitals of Ti and Nb. It is also shown that the

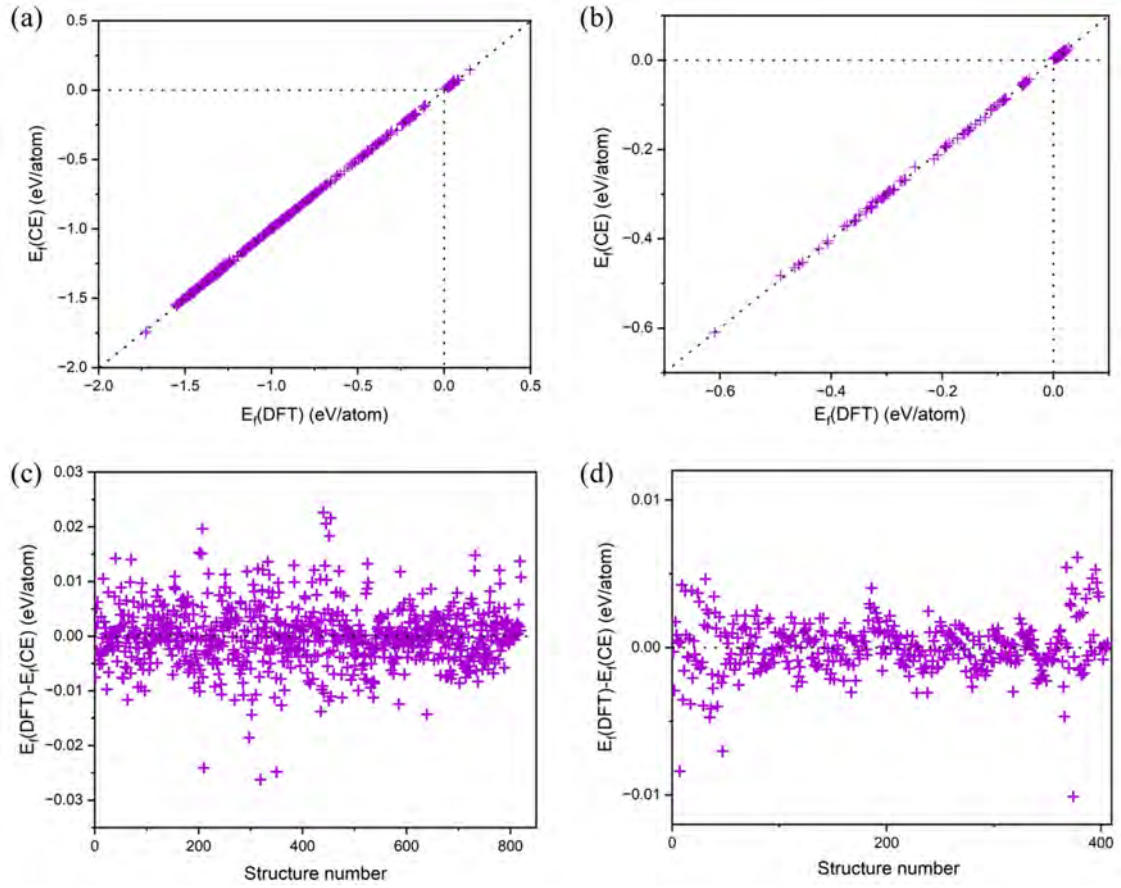

Figure 6.7: The DFT and CE fitted E_f of the structures in (a) hcp and (b) bcc Ti-Nb-O system and the residuals of CE fit of the (c) hcp and (d) bcc system.

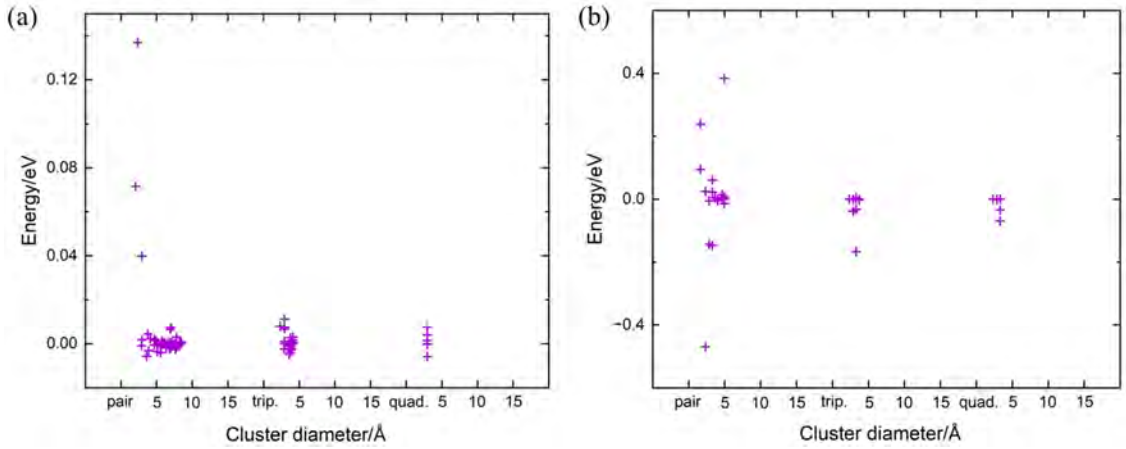

Figure 6.8: The effective cluster interactions (ECIs) of the optimized clusters used in the (a) hcp and (b) bcc Ti-Nb-O CE model.

s and *p* orbitals of oxygen are predominantly responsible for the electronic states below -5 eV. The *d* orbitals of Ti and Nb also contribute to the electronic states at around -7.5 eV where the *p* orbitals of oxygen are predominant, the presence of the overlapping peaks at -7.5 eV suggests

the oxygen p orbitals hybridize with d orbitals of Ti and Nb to form covalent bonds. Therefore, the chemical bonds formed between O, Ti, and Nb are directional and polar, with the electron densities tending to be closer to the more electronegative oxygen atoms, leading oxygen atoms to contribute more significantly to the electronic state density at this energy level. Furthermore, the peak width and intensity at around -7.5 eV are positively correlated with the oxygen content of the ground states. Specifically, the electronic states at this energy level for ground-states TiNbO, $Ti_4Nb_2O_3$, and Ti_5NbO_3 are higher than those for $Ti_2Nb_6O_3$, and greater than those for Ti_4Nb_4O and Ti_3Nb_5O. This also indicates that the degree of orbital hybridization and the electronic interactions enhance with the increase in oxygen content, which is also observed in most transition metal oxides [205–207]. In addition, except for the ground-state $Ti_2Nb_6O_3$, the d orbitals of Ti contribute the most to the anti-bonding interactions in the other ground states. For the ground-state Ti_3Nb_5O, the contributions of the d orbitals from Ti and Nb to the anti-bonding interactions are almost equal. In other words, when the Nb content is less than 0.55, the anti-bonding interactions in the hcp ternary system are dominated by the d orbitals of Ti. Figure 6.10 shows the projected density of states of each sub-orbital in d orbitals of Ti and Nb. It can be seen that the electronic states at -7.5 eV below the Fermi level are mainly contributed by the Ti and Nb $d_{xy} + d_{x^2-y^2}$ orbitals, while the d_{z^2} orbitals have almost no contribution to the electronic states at this energy level. This indicates that the p orbitals of oxygen primarily hybridize with the Ti and Nb $d_{xy} + d_{x^2-y^2}$ and $d_{xz} + d_{yz}$ orbitals to form bonding states through electronic interactions [208, 209]. We can also see that all d sub-orbitals significantly contribute to the electronic states at energy levels from -3 to 0 eV, indicating that the hybridization between the d_{z^2}, $d_{xy} + d_{x^2-y^2}$, and $d_{xz} + d_{yz}$ orbitals facilitates bonding interactions between Ti and Nb atoms on the same layer and between two adjacent layers. Moreover, the Ti and Nb $d_{xy} + d_{x^2-y^2}$ and $d_{xz} + d_{yz}$ orbitals contribute more to the electronic states above the Fermi level compared to the d_{z^2} orbitals, thus causing a greater anti-bonding interaction in the ground-state.

The contribution of the s and p orbitals of oxygen and the d orbitals of Ti and Nb to the total density of states of the ground states in the bcc ternary system was depicted in Figure 6.11. As can be seen, similar to the ground states in the hcp ternary system, the electronic states around

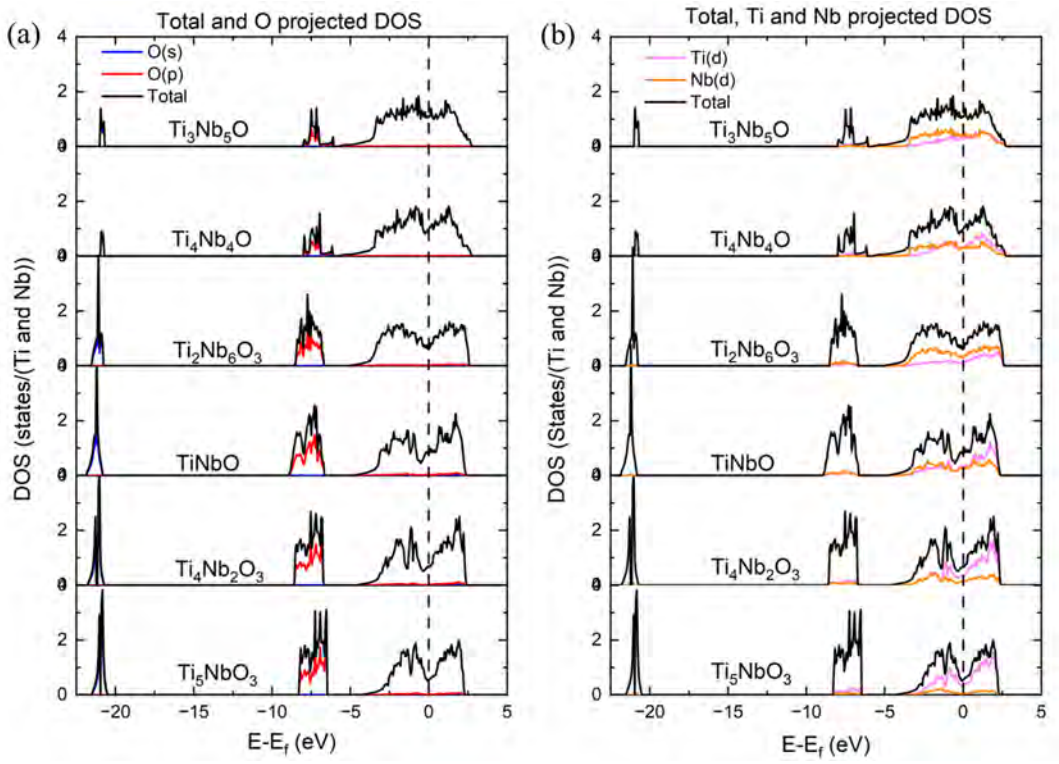

Figure 6.9: Total DOS and the projected DOS of (a) *s* and *p* orbitals of oxygen and (b) Ti and Nb *d* orbitals of the ground states in the hcp Ti-Nb-O system.

the -7.5 eV energy level are mainly contributed by the *p* orbitals of oxygen, while the electronic states around the Fermi level are contributed by the *d* orbitals of Ti and Nb. Moreover, the degree of hybridization and bonding interactions between O and Ti or Nb in the ground states increases with the increase in oxygen content. It is also evident that when the Nb content in the Ti-Nb sublattice is less than 0.5, the hybridization and electronic interactions between Ti and oxygen are stronger. Therefore, in the ground-states Ti_3NbO, Ti_2NbO, and Ti_4NbO_2, the *d* orbitals of Ti contribute more to the electronic states at the energy level of -7.5 eV compared to the *d* orbitals of Nb. Besides, except for the ground-state $TiNb_2O$, the anti-bonding states in other ground states are mainly contributed by the *d* orbitals of Ti. Figure 6.12 presents the contribution of the density of states of *d* sub-orbitals to the total density of states of *d* orbitals of Ti and Nb in these ground states. Similar to the ground states in the hcp ternary system, at the energy level of around -7.5 eV, the orbitals that hybridize with the oxygen *p* orbitals are primarily the Ti and Nb $d_{xy} + d_{x^2-y^2}$ and $d_{xz} + d_{yz}$ orbitals. The d_{z^2} orbital, however, hardly participates in hybridization with the oxygen and also contributes very little to the anti-bonding

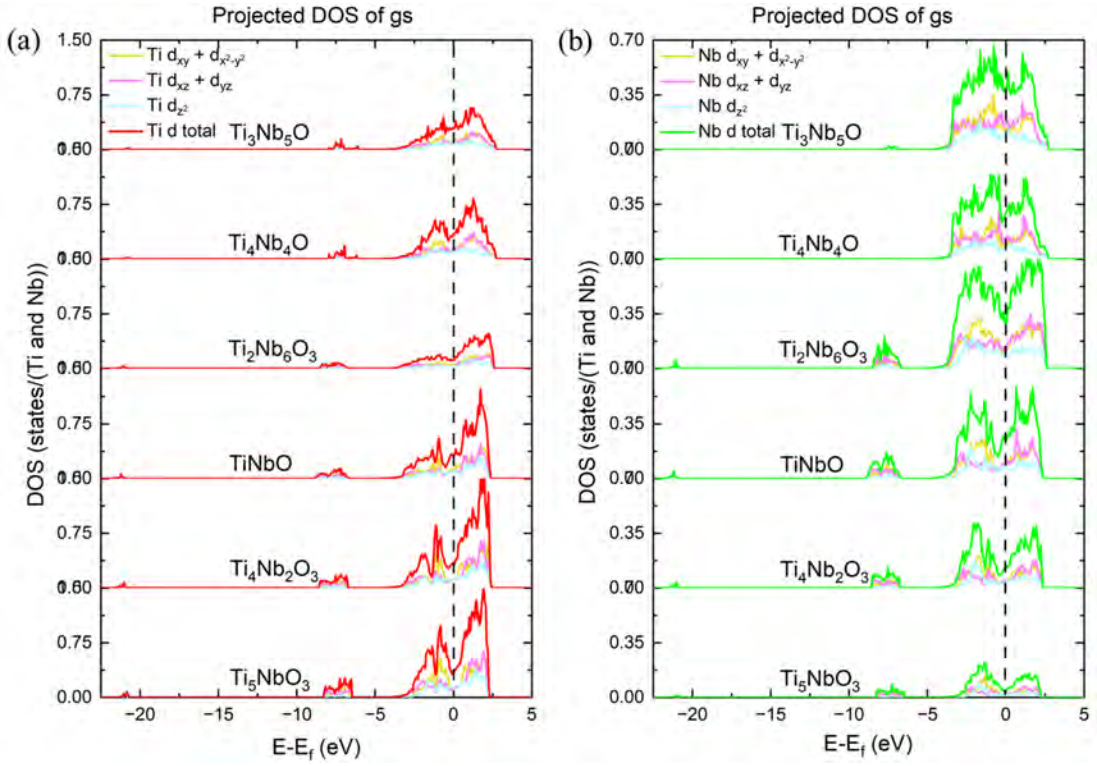

Figure 6.10: Projected DOS of each sub-orbital of the (a) Ti and (b) Nb *d* orbitals of the ground states in the hcp Ti-Nb-O system.

states above the Fermi level. For the energy level from 0 to -2.5 eV below the Fermi level, unlike the hcp ternary ground states where the d_{z^2} orbital significantly influences the bonding between Ti and Nb atoms on the one and adjacent layers, the d_{z^2} orbital has a smaller impact on the bonding between Ti and Nb in the bcc ternary ground states [192]. Instead, the bonding is primarily driven by the $d_{xy} + d_{x^2-y^2}$ and $d_{xz} + d_{yz}$ orbitals.

Bader analysis was then performed to examine the electron gain and loss of each atom in the hcp ternary ground states, as shown in Table 6.3, in all ground states, oxygen and Ti atoms gain electrons and lose electrons, respectively, due to the big electronegativity difference between oxygen and Ti [210, 211]. It is also can be seen that Nb atoms gain electrons in the ground-states Ti_3Nb_5O, Ti_4Nb_4O, and Ti_5NbO_3, while Nb atoms lose electrons in the ground-states $Ti_2Nb_6O_3$, TiNbO, and $Ti_4Nb_2O_3$. The difference in the performance of Nb atoms to gain or lose electrons in different ground states is mainly due to the electronegativity of Nb, which is intermediate between Ti and O. This causes Nb to lose electrons when it tends to bond with

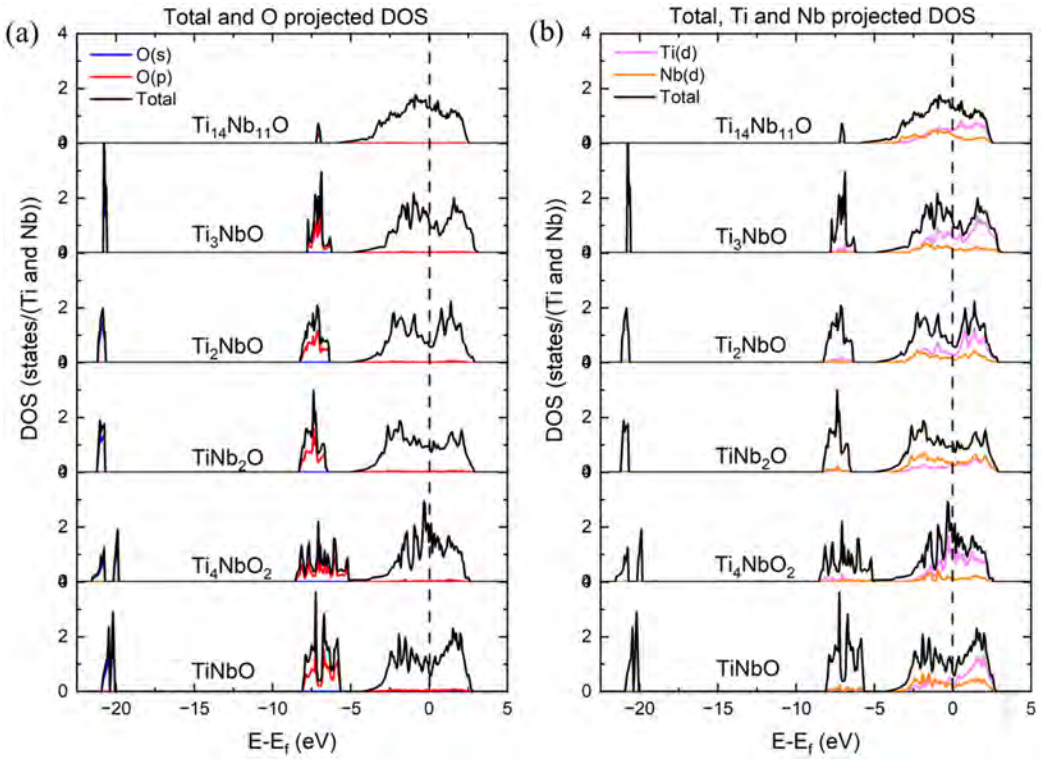

Figure 6.11: Total DOS and the projected DOS of (a) *s* and *p* orbitals of oxygen and (b) Ti and Nb *d* orbitals of the ground states in the bcc Ti-Nb-O system.

oxygen and gain electrons when it tends to bond with Ti. As shown in Figure 6.9, at the energy level around -7.5 eV, the electronic states contributed from Nb in the ground-states $Ti_2Nb_6O_3$, TiNbO, and $Ti_4Nb_2O_3$ are larger than in the other ground states, indicating a stronger tendency to bond with oxygen, thereby a higher possibility of losing electrons for Nb. Furthermore, in the ground-state TiNbO, the number of electrons gained or lost by different atoms of one element is the same. To be specific, each Nb atom loses 0.322 electrons, each Ti atom loses 1.068 electrons, and each oxygen atom gains 1.39 electrons, indicating that only for the ground-state TiNbO, the contribution of different atoms of the same element to orbital hybridization and bonding interactions is identical. Similar to the hcp ternary ground states, as shown in Table 6.4, oxygen can only gain electrons due to its very stronger electronegativity than Ti and Nb and, in some ground states, Nb atoms lose electrons, while in other ground states, they gain electrons. However, in the ground-state $Ti_{14}Nb_{11}O$, one Nb atom loses electrons, the other Nb atoms gain electrons [212, 213], and surprisingly, three Ti atoms in this ground-state gain electrons, indicating the complicated interactions between Ti and Nb.

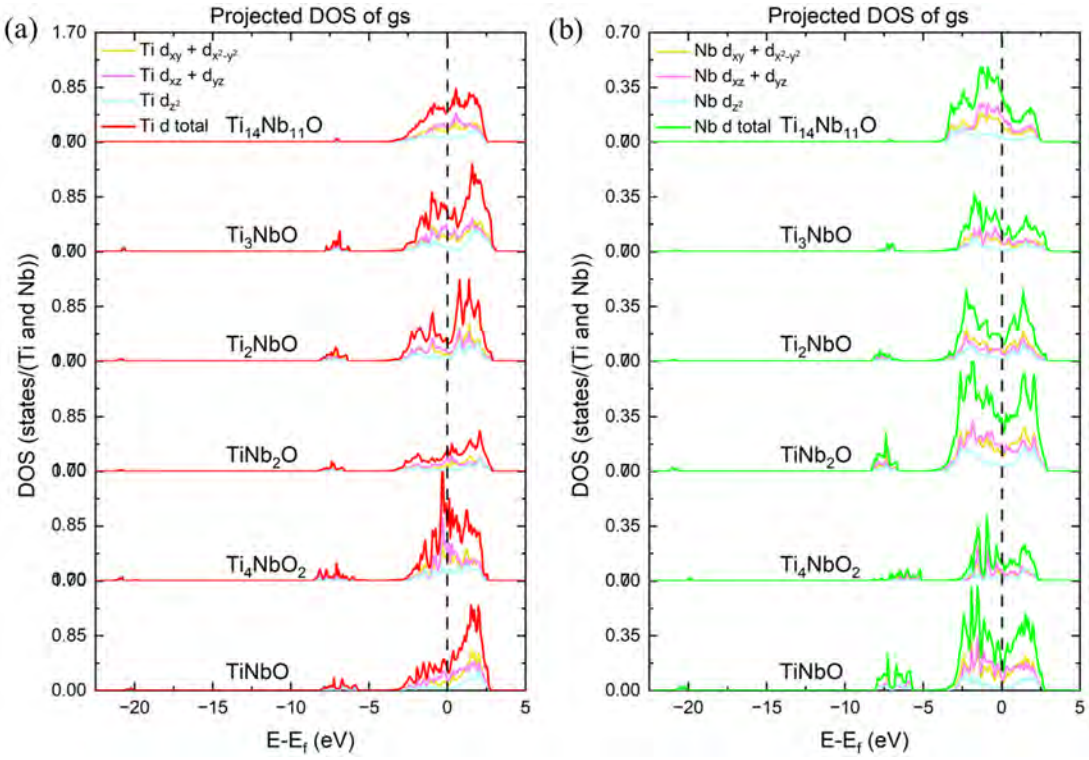

Figure 6.12: Projected DOS of each sub-orbital of the (a) Ti and (b) Nb *d* orbitals of the ground states in the bcc Ti-Nb-O system.

6.3 Thermodynamic properties of the grounds states

Subsequently, the Debye-Grüneisen model was employed to evaluate the thermodynamic and vibrational properties of the ternary ground states in the hcp and bcc Ti-Nb-O systems by fitting a series of E-V data of the ground-state to the Birch–Murnaghan equation of state. As shown in Figure 6.13 and 6.14, the Birch–Murnaghan equation of state well fits the E-V data points of all the ground states, with no outliers. Also, it is evident that the cell volume of the hcp ternary ground states is generally larger compared to most bcc ternary ground states. Furthermore, the volume change of the supercell bcc $Ti_{14}Nb_{11}O$ exceeds 500 bohr^3. Then, the vibrational free energy and some thermodynamic properties of all hcp and bcc ground states were evaluated by importing the E-V data to the Debye-Grüneisen model. The variations of linear thermal expansion (LTE) and vibrational free energy (F_{vib}) of the hcp ternary ground states with temperature are described in Figure 6.15(a) and (b), respectively. It is expected that, like other metallic systems, the LTE of all the hcp ground states increases with temperature,

Table 6.3: Gain and loss of electrons of each O, Nb and Ti atom in the hcp Ti-Nb-O ternary ground states via Bader analysis.

Ground-state	O atoms	Nb atoms	Ti atoms
Ti_3Nb_5O	+1.411	+0.156, +0.314, +0.203, +0.152, +0.256	-0.866, -0.947, -0.678
Ti_4Nb_4O	+1.429	+0.294, +0.292, +0.251, +0.251	-0.762, -0.762, -0.496, -0.496
$Ti_2Nb_6O_3$	+1.369, +1.384, +1.384	-0.337, -0.337, -0.331, -0.331, -0.231, -0.231	-1.170, -1.170
$TiNbO_2$	+1.39, +1.39, +1.39, +1.39	-0.322, -0.322, -0.322, -0.322	-1.068, -1.068, -1.068, -1.068
$Ti_4Nb_2O_3$	+1.412, +1.409, +1.409	-0.244, -0.205	-0.899, -0.947, -0.947, -0.988
Ti_5NbO_3	+1.429, +1.427, +1.425	+0.038	-0.833, -0.880, -0.829, -0.891, -0.886

and the growth rate of the LTE decreases after 400 K, however, the rate of change in LTE varies among different ground states. $Ti_2Nb_6O_3$ and Ti_5NbO_3, which have the highest and lowest Nb content on the Ti-Nb sublattice, respectively, exhibit the highest and lowest LTE across the entire temperature range. Except for Ti_3Nb_5O, which shows comparable LTE to $Ti_4Nb_2O_3$, the LTE of other ground states demonstrate a decrease with an increase in Ti content in the configuration. In addition, as shown in Figure 6.15(b), the ordering $Ti_2Nb_6O_3$ and Ti_5NbO_3, which have the highest and lowest LTE, respectively, exhibit the lowest and highest F_{vib} values throughout the overall temperature range. This is mainly due to that the volume expansion of the compounds extends the chemical bonds [181], leading to an increase in vibrational entropy. It is also observed that at lower temperatures (< 400 K), Ti_3Nb_5O and Ti_4Nb_4O with lower oxygen content have smaller F_{vib}, while the other four ground states have comparable F_{vib}. This is because the lower the oxygen content, the fewer chemical bonds between Ti and Nb atoms with oxygen atoms, resulting in weaker structural stiffness and stability, higher vibrational

Table 6.4: Gain and loss of electrons of each O, Nb and Ti atom in the bcc Ti-Nb-O ternary ground states via Bader analysis.

Ground-state	O atoms	Nb atoms	Ti atoms
$Ti_{14}Nb_{11}O$	+1.426	+0.314, +0.032, +0.032, +0.629, +0.200, +0.107, +0.209, +0.111, +0.121, +0.321, -0.026	+0.303, +0.151, +0.276, -0.369, -0.590, -0.698, -0.059, -0.033, -0.058, -0.437, -0.442, -0.483, -0.383, -0.651
Ti_3NbO	+1.404	+0.507	-0.633, -0.633, -0.645
Ti_2NbO	+1.396	+0.038	-0.718, -0.716
$TiNb_2O$	+1.374	-0.044, -0.302	-1.029
Ti_4NbO_2	+1.369, +1.340	-0.278	-1.722, -0.027, -0.270, -0.412
TiNbO	+1.352, +1.373	-0.076, -0.542	-1.203, -0.905

entropy, and thereby lower F_{vib} [181]. When the temperature exceeds 700 K, the bonding of Ti with Nb and oxygen atoms determines the stiffness and stability of the configuration. That is, at a specific oxygen content, the higher the Ti content in the ground-state, the more chemical bonds formed, leading to higher structural stability and F_{vib}. Consequently, the F_{vib} follows the order: $Ti_5NbO_3 > Ti_4Nb_2O_3 \approx Ti_4Nb_4O > TiNbO \approx Ti_3Nb_5O > Ti_2Nb_6O_3$. Figure 6.16 shows the LTE and F_{vib} of the bcc ternary ground states in the bcc Ti-Nb-O system. Similar to the hcp ternary system, the LTE of bcc ternary ground states with high Ti content is lower than that of bcc ground states with low Ti content, suggesting that the LTE of Ti_2NbO, Ti_4NbO_2, Ti_3NbO, and $Ti_{14}Nb_{11}O$ is lower than that of TiNbO and $TiNb_2O$. For ground states with close Ti content, namely Ti_4NbO_2, Ti_3NbO, and $Ti_{14}Nb_{11}O$, the differences in oxygen content cause slight differences in LTE. Notably, TiNbO, which has the highest oxygen content, exhibits the largest LTE, and its LTE maintains a high growth rate even after the temperature exceeds 400 K. This trend is also observed in the ground-state Ti_2O in the Ti-O binary system. As shown in Figure 6.16(b), compared to the ground states with high Ti content, the F_{vib} of TiNbO and

$TiNb_2O$, which have lower Ti content, decreases more rapidly. Above 500 K, their F_{vib} is lower than that of the other four ground states, and the lower oxygen content in $TiNb_2O$ also leads to a decrease in the number of bonds, resulting in a lower F_{vib}. Therefore, across the entire temperature range, the F_{vib} of $TiNb_2O$ is consistently lower than that of TiNbO. The trends observed in the bcc ternary system are very similar to the conclusions drawn from the hcp ternary system, indicating that the increase of octahedral interstitial oxygen reduces vibrational entropy. Moreover, as the temperature increases, Ti in the substitutional sites of both hcp and bcc lattices more effectively reduces the vibrational entropy compared to Nb, thereby increasing the F_{vib} of the system.

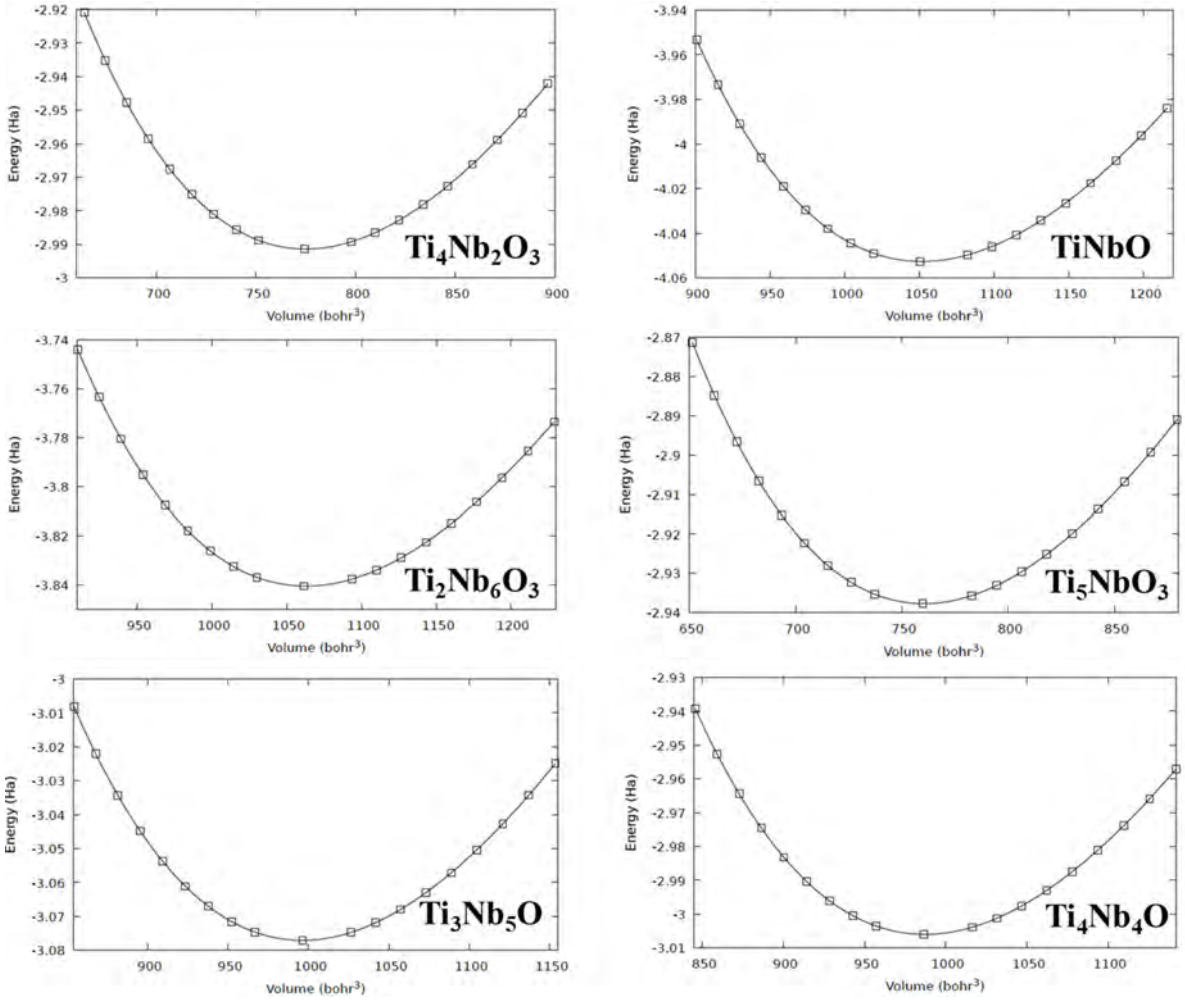

Figure 6.13: E-V data and the fitted curve of the ternary ground states in hcp Ti-Nb-O system.

Finally, we calculated the thermodynamic quantities of the ternary ground states in the hcp Ti-Nb-O system across compositions and temperatures. However, our Monte Carlo results

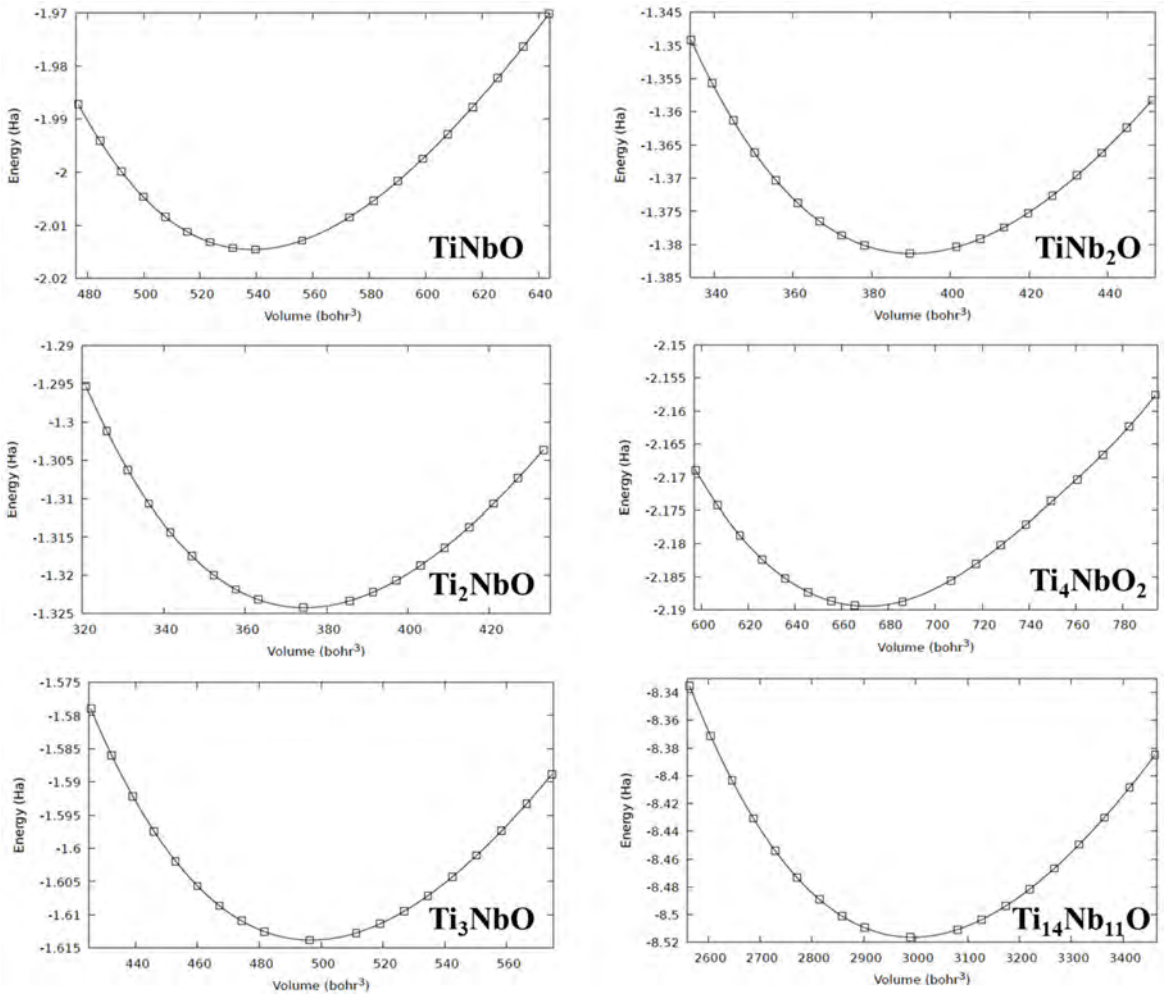

Figure 6.14: E-V data and the fitted curve of the ternary ground states in bcc Ti-Nb-O system.

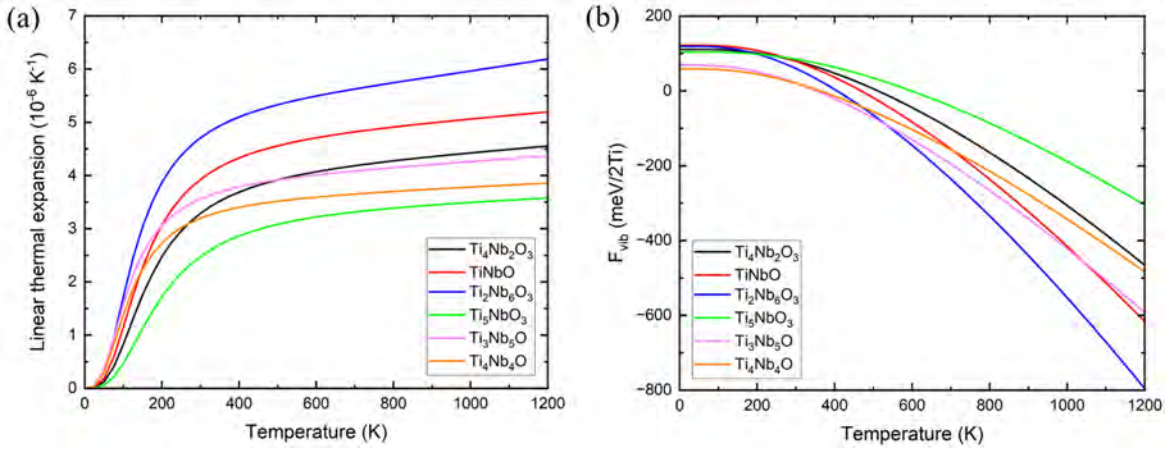

Figure 6.15: Linear thermal expansion and total vibrational free energies of the ternary ground states in hcp Ti-Nb-O system.

show all these ordered compounds can decompose on heating into disordered α phase at very temperatures (20 ~60 K), therefore the Helmholtz free energy (F) of the disordered α phase was

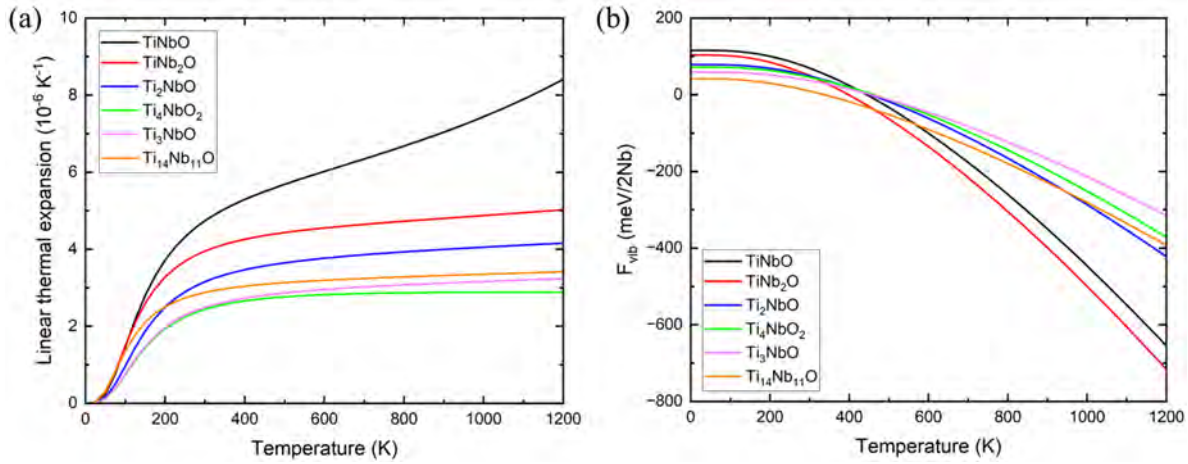

Figure 6.16: Linear thermal expansion and total vibrational free energy of the ternary ground states in bcc Ti-Nb-O system.

studied instead. Figure 6.17(a) shows the curved surface of F of the α phase at 1000 K, by fitting the limited F data points obtained by Monte Carlo simulations to a polynomial function. It is evident that the fitted surface is smooth and the F in the oxygen-rich region is greater than that in the Nb-rich region, both of which are higher than the F in the Ti-rich region. This indicates the α phase presents higher thermodynamic stability over the Ti-rich region than other compositional spaces. Although no literature reports the F of the α phase in Ti-Nb-O systems at any temperatures, our calculated F for the pure hcp Ti at 1000 K is -0.53 eV/active site (-51.1 kJ/mol) which is close to the value of -44.8 kJ/mol calculated by Xiong *et al*. [214]. The projected F on the composition plane, which represents the F gradient change with the composition, is shown in Figure 6.17(b). It also can be seen that oxygen-rich region has the highest F, and Ti-rich region shows the highest thermodynamic stability, especially at the oxygen composition around 0.33 in Ti-O binary line (darkest area of the cool color tones). This can be confirmed by the thermodynamic investigation of the hcp Ti-O binary system in chapter 4 where we found Ti_2O has a lower F than Ti_6O and Ti_3O at 1000 K.

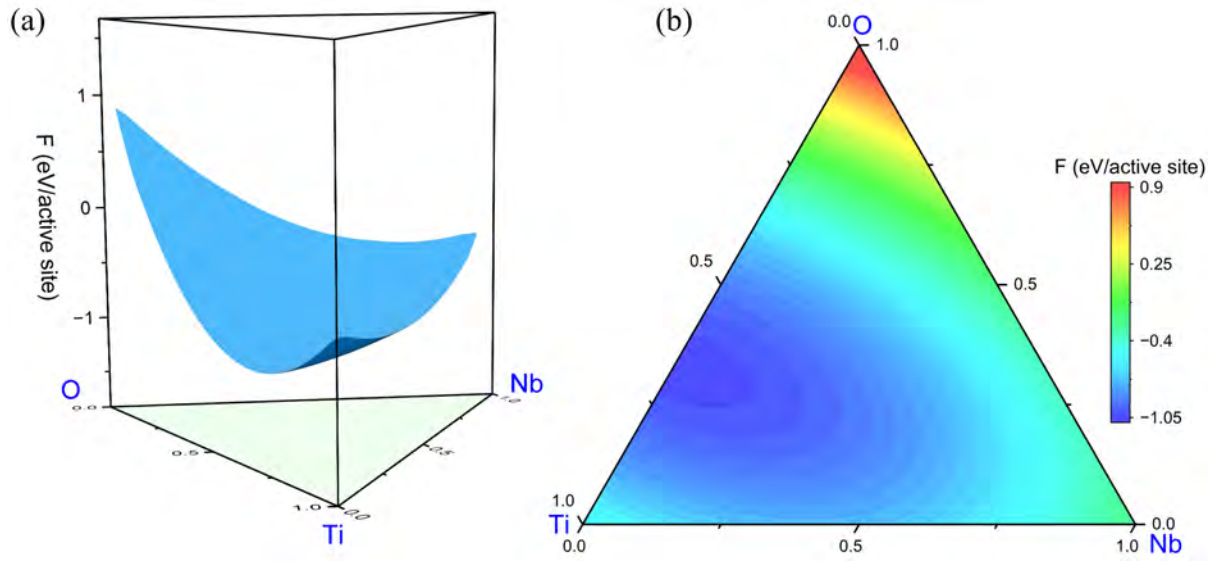

Figure 6.17: The fitted Helmholtz free energy (F) of the disordered α phase in the hcp Ti-Nb-O system across the whole compositional space at 1000 K: (a) 3D curved surface of F and (b) projection of F on the x-y plane.

6.4 Summary

In this chapter, a great number of ternary configurations in the Ti-rich and Nb-rich regions were enumerated, respectively, for the hcp and bcc Ti-Nb-O ternary systems. All the configurations were fully relaxed through DFT calculations and those over-relaxed structures in these two ternary systems were identified by performing CNA and RA calculations. Compared to the hcp system, we found that there are more highly distorted structures in the bcc system, with some structures surprisingly having RA values greater than 0.5.

Subsequently, the E_f of all the structures in the two ternary systems were calculated and it is observed that the ternary structures having higher oxygen content present lower E_f, while the E_f is less sensitive to the Ti and Nb content. Furthermore, some previously unreported ternary ordered ground states were discovered in both systems and the phase equilibria at 0 K were established based on the E_f of the ground states in each system. Two CE models were then accurately developed for the two ternary systems, respectively, by fitting the DFT calculated E_f precisely, which demonstrates the good predictive power of the constructed CE models. The ECIs of both two CE models converge well with increasing cluster diameter, although the ECI

values in the bcc system were larger compared to those in the hcp system.

The density of states for the ground states in both systems was further evaluated, which helps us understand the orbital hybridization and bonding interactions between oxygen and metallic Ti and Nb atoms. A detailed analysis of the projected density of states of the *d* sub-orbitals of Ti and Nb was performed to deeply investigate their interactions with oxygen and intermetallic interactions, as well as the impact on anti-bonding states. After the E-V curves of all ground states were calculated, the LTE and F_{vib} of the ordered ground states in both systems were examined by employing the Debye-Grüneisen model, revealing the roles played by oxygen and metallic Ti and Nb atoms in these thermodynamic quantities. In the end, Monte Carlo simulations were performed to compute the thermodynamics of the disordered α phase in the hcp Ti-Nb-O system over the composition at 1000 K. It can be concluded that Ti-rich region has the highest thermodynamic stability than other composition areas.

Chapter 7

Comparisons Between the Binary Ti-O, Ti-Nb, and Ternary Ti-Nb-O Systems

In the previous three chapters, the energetics, ground-state electronic structure, and thermodynamic properties of the configurations in the hcp Ti-O, hcp Ti-Nb, bcc Ti-Nb, hcp Ti-Nb-O, and bcc Ti-Nb-O systems were systematically investigated. It is found that the introduction of oxygen, within its solubility limit in Ti, does not cause significant distortion in the configurations, and all the structures in the hcp Ti-O system maintain the ideal hcp crystal lattice (Figure 4.3). In contrast, as shown in Figure 5.1, adding Nb to hcp Ti can result in large distortions in many structures, with some even relaxing to other geometries. Our findings differ from the viewpoint of Chinnappan *et al*. [44], in that the addition of Nb to bcc Ti does not induce significant distortions in the configurations. This highlights the critical role of oxygen in stabilizing the α phase in Ti and Nb in stabilizing the β phase in Ti. It was observed, from the RA results of the ternary structures in the ternary systems (Figure 6.1), that although the hcp Ti-Nb system contains many highly distorted configurations, the addition of oxygen significantly reduces these distortions, thereby mitigating the mechanical instability induced by Nb. On the contrary, adding Nb to bcc Ti enhances the mechanical stability of most structures across the entire composition range, while the subsequent introduction of oxygen disrupts this stability, leading to significant relax-

ations and increased distortions, introducing many mechanical instabilities to the bcc ternary system. This indicates that the mechanical instability induced by the introduction of oxygen in the bcc Ti-Nb system is more significant than the stabilization effect provided by Nb as a strong β phase stabilizer.

The stability of the system can also be demonstrated by the E_f convex hull of each system. It is evident, from Figures 4.1 and 5.2, that the E_f of hcp Ti-O structures are lower than the E_f of those in the hcp and bcc Ti-Nb systems. Comparing the E_f of the ternary structures in the hcp and bcc Ti-Nb-O systems (Figures 6.2 and 6.3) which use the same reference states, it shows that the E_f of the hcp ternary structures are much lower, indicating that the hcp ternary system is more stable than the bcc ternary system. For instance, the E_f of the hcp ternary ground-state TiNbO is -1.32 eV/atom, while that of the bcc ternary ground-state TiNbO is -0.61 eV/atom, higher by 0.71 eV/atom. On the other hand, the ECIs derived from the constructed CE models reveal that the ECI values of all clusters in the hcp and bcc Ti-Nb systems fall within the range of $0 \sim 10$ meV, as illustrated in Figure 5.5. In contrast, the ECIs in the hcp Ti-O system (Figure 4.5) are larger, indicating stronger interactions between O-O or O-Vac interstitial sites compared to the Ti-Nb, Ti-Ti, or Nb-Nb substitutional sites in the Ti-Nb system. Notably, as shown in Figure 6.8(a), some crucial clusters with larger ECIs are also observed from the CE model of the hcp Ti-Nb-O system. These clusters not only reproduce the important O-O or O-Vac sites from the hcp Ti-O system but also include significant interactions between interstitial and substitutional cross-sites, such as O-Ti, O-Nb, O-Ti-Nb, O-Ti-Ti, and O-Nb-Nb interactions. It can also be observed from Figure 6.8(b) that the introduction of oxygen into the bcc Ti-Nb system causes significant changes in the ECIs. These ECIs point to the cross-sites of octahedral interstitial sublattices (O-Vac) and substitutional lattices (Ti-Nb), such as O-Ti and O-Nb, reflecting the strong interactions between oxygen and the metallic Ti and Nb in the bcc Ti-Nb-O system. Further analysis of the DOS of each element in the ground states reveals that the p orbitals of oxygen hybridize with the d orbitals of Ti and/or Nb in the hcp Ti-O, hcp Ti-Nb-O and bcc Ti-Nb-O systems, promoting the formation of bonding states exhibiting the characteristics of covalent bonds. Similarly, the d orbitals of Ti hybridize with the d orbitals of Nb in the hcp and

bcc Ti-Nb systems, however, this hybridization is concentrated near the higher energy Fermi level, resulting in the formation of the bonding states having characteristics of metallic bonds and weaker interactions, which is also the evidence of the lower ECI values.

Through the calculation of the thermodynamic properties of ground states in binary and ternary systems, it was found that the LTE of all ground states exhibits exponential growth below 400 K (as seen in Figures 4.12(b), 5.12, 6.15(a) and 6.16(a)), while the growth slows and gradually converges above 400 K. This is because, at lower temperatures, the thermal vibrations of atoms in alloy systems increase as the temperature rises. The anharmonicity of these vibrations causes the atoms to move further apart on average, leading to a rapid increase in linear thermal expansion [215, 216]. The initial stages of heating activate more atomic vibrational modes, which contribute significantly to the thermal expansion. As temperature increases beyond 400 K, most of the vibrational modes that contribute to expansion are already activated. For another, the metallic system approaches a quasi-equilibrium state where the increase in atomic separation due to thermal expansion is balanced by the metallic bonding forces, leading to a slower growth of LTE [217, 218]. More importantly, comparing Figure 5.12 with Figure 6.15(a) and 6.16(a), we notice that the introduction of oxygen in hcp and bcc Ti-Nb system results in the reduction of LTE over the whole temperature. For example, in the temperature range of 0 to 1200 K, the LTE of the ground-state bcc Ti_2Nb ranges from 0 to $8\times10^{-6}K^{-1}$, whereas the LTE of the ternary ground-state bcc Ti_2NbO changes from 0 to $4\times10^{-6}K^{-1}$. This downward change can be attributed to that the bonding interactions of oxygen with Ti and Nb show the characteristics of covalent bonds which leads to a rigidity of the ternary ground states, thereby restricting the movement of Ti and Nb atoms and making the crystal structure of ternary ground states less responsive to thermal expansion [219]. From another point of view, the introduction of oxygen can cause the effect of solution strengthening and thereby increase the hardness of the system. Typically, a harder material tends to exhibit lower thermal expansion since the atomic bonds resist thermal vibrations more effectively [220, 221]. Moreover, the solution of oxygen increases the elastic constants of the Ti-Nb systems, thus improving the elastic modulus of the systems. Generally speaking, alloys with higher elastic modulus show lower coefficients

of thermal expansion due to their increased resistance to deformation under thermal stress [46, 222].

Unlike LTE, the F_{vib} of all binary and ternary ground states decreases slowly before the temperature increases to 400 K. As the temperature rises beyond 400 K, the rate of decrease in F_{vib} gradually accelerates. The main reason is that, at low temperatures, the vibrational entropy, which contributes to the F_{vib}, increases slowly as fewer lattice vibrational modes are excited [223]. The specific heat capacity at constant volume, which is related to the number of excited lattice vibrational modes, is lower. In addition, quantum mechanical effects are more significant at low temperatures, leading to discrete vibrational energy levels. The number of these levels changes with temperature, resulting in a slower decrease in F_{vib} [224, 225]. As temperature increases from ~400 K, the alloy system transitions from quantum to classical behavior. In the classical regime, vibrational energy is more continuous, and higher temperatures significantly increase vibrational entropy. The higher the temperature, the more lattice vibrational modes are excited, leading to a more rapid increase in vibrational entropy. This contributes to a faster decrease in F_{vib} as the temperature continues to rise.

In summary, as two important alloying elements of Ti, oxygen and Nb have significant impacts on the mechanical stability, bonding interactions in the system, and the thermodynamic properties of various structures in both hcp and bcc Ti-Nb-O systems. Despite the multifaceted and complex nature of these influences, we believe that the findings and discussions presented in this study provide valuable insights for the broader readers.

Chapter 8

Conclusions and Future Work

8.1 Conclusions

Oxygen and Nb are two representative alloying elements of Ti to form high-temperature and chemically-aggressive resistance Ti alloys. The investigation on the thermodynamic characteristics of Ti-O, Ti-Nb and especially Ti-Nb-O systems has attracted much attention in recent years. However, in this regard, a satisfied experimental technique or modeling scheme is still yet to be developed due to the appearance of a variety of oxides in hcp Ti-O system and the mechanical instability present in hcp and bcc Ti-Nb and Ti-Nb-O systems. In this dissertation, DFT calculations and the cluster expansion method were combined with the Debye-Grüneisen model and the Monte Carlo simulations to study the ground-states characteristics, electronic structure, thermodynamic properties and phase stabilities of the hcp Ti-O, hcp Ti-Nb, bcc Ti-Nb, hcp Ti-Nb-O and bcc Ti-Nb-O systems.

In chapter 4, we first performed a series of DFT calculations to construct the E_f of convex hull of the hcp Ti-O system such that some stable ordering ground states, namely Ti_6O, Ti_3O, Ti_2O and unreported $Ti_{12}O_5$, were discovered. A predictive cluster expansion model was then constructed to fit the DFT E_f energies and represent the energetics of the whole hcp Ti-O system,

and many crucial ECIs were derived from the CE model. The density of states and the charge density difference of these ordering Ti-O oxides were further analyzed to reveal the underlying bonding interactions between interstitial oxygen and Ti. It was found that σ and π bonds are formed in these ground states and the bonding strength is positively correlated with the oxygen concentration. The thermodynamic properties of these oxides were examined, and it shows that the Ti_2O has the largest F_{vib} and the lowest heat capacities over the entire temperature range. Another CE model was established using the F_{vib} to evaluate the effect of vibrational entropy on the order-disorder transition temperatures of the ground states. Downward corrections on the order-disorder transition temperature appeared for all the Ti-O ground states when including the F_{vib} in the Monte Carlo simulations. The calculated transition temperature for the Ti_6O is only 45 K higher than the experimental data.

At the beginning of chapter 5, the E_f of a group hcp and bcc Ti-Nb structures were calculated. It is determined that the reason for the inability to establish robust CE models is the presence of highly distorted structures in the Ti-Nb systems which can introduce much noise into the construction of the CE model. After performing CNA and RA calculations on all configurations in both hcp and bcc Ti-Nb systems, it was observed that the hcp Ti-Nb system contains more over relaxed structures, indicating that the hcp Ti-Nb system exhibits more mechanical instabilities compared to the bcc Ti-Nb system. These structures were then excluded from the CE model to obtain well-converged CE models with good predictive capability. Further analysis of the density of states of the ground states in both systems revealed that their bonding characteristics are similar, specifically the hybridization of $d_{xy} + d_{x^2-y^2}$ and $d_{xz} + d_{yz}$ orbitals. Subsequently, we calculated the thermodynamic properties of these ground states, including F_{vib}, LTE, and bulk modulus. All the F_{vib} in each system were further employed to construct another CE model such that the effect of vibrational entropy was incorporated into the calculation of the phase boundaries between the α and β phases. The results obtained are in good agreement with the experimental data, indicating that vibrational entropy plays a crucial role in lowering the phase transition temperatures between the disordered α and β phases.

In chapter 6, a larger number of ternary structures in the Ti-rich and Nb-rich regions were enumerated for the hcp and bcc Ti-Nb-O systems, respectively. CNA and RA analysis were executed for each ternary structure in these two systems by performing DFT relaxation calculations. The results indicate that, compared to the hcp ternary structures, the bcc ternary structures exhibit greater relaxation, with some structures showing an RA exceeding 0.5, and many relaxing to different geometries. This suggests that although the bcc Ti-Nb system is more stable than the hcp Ti-Nb system, the introduction of oxygen fundamentally alters the stability of both systems, in other words, the hcp Ti-Nb-O system is mechanically more stable than the bcc Ti-Nb-O system. Subsequent E_f calculations corroborate this conclusion, showing that the E_f of hcp ternary structures are significantly lower than that of bcc ternary structures. Both of these two ternary systems exhibit a trend where E_f decreases with increasing oxygen content while being relatively insensitive to Ti and Nb content. From the E_f convex hulls, some previously unreported ordered ground states in these two ternary systems were identified for the first time, and the 0 K phase equilibria were established based on the E_f. Two separate predictive CE models were then developed, well fitting the DFT E_f, and revealing that the introduction of oxygen significantly affects the ECIs of both Ti-Nb systems. Some important interactions between interstitial and substitutional sites were identified, such as Ti-O, Nb-O, O-Ti-O, O-Nb-O, and O-Ti-Nb-Vac interactions. The density of states calculations were consequently performed to analyze the bonding mechanisms in these ternary ground states. It was found that the hybridization between the *p* orbitals of oxygen and the *d* orbitals of Ti and Nb is responsible for the formation of low-energy bonding states that exhibit strong covalent characteristics. For another, the hybridization between the *d* orbitals of Ti and Nb promotes the formation of high-energy bonding and anti-bonding states, showing metallic bonding characteristics. Furthermore, we calculated the F_{vib} and LTE for all ternary ground states, highlighting the critical role of interstitial oxygen interactions with metallic Ti and Nb in determining these thermodynamic properties. At the end of this chapter, since all the ternary ground states found in the hcp Ti-Nb-O system turn to be unstable at very low temperatures and decompose into disordered α phase, we calculated the F of the disordered α phase in the hcp Ti-Nb-O system at 1000 K. The Monte Carlo results show

the Ti-rich region has the highest thermodynamic stability than other composition area at this temperature.

In the end, in chapter 7, based on the computational results presented in chapters 4, 5, and 6, we conducted an in-depth analysis of the intrinsic connections among ground-state properties, lattice distortions, electronic structures, and thermodynamics in these binary and ternary systems. This comprehensive study reveals the profound impact of energetics and interatomic interactions on the high-temperature thermodynamics of these systems.

8.2 Future work

This study investigates the ground-state characteristics, electronic structures, and thermodynamics of hcp Ti-O, Ti-Nb, Ti-Nb-O systems, and bcc Ti-Nb, bcc Ti-Nb-O systems. A comprehensive analysis of the energetics, internal bonding mechanisms, and high-temperature thermodynamic behavior of each system was achieved. Future work will focus on the thermodynamics of the ordered and disordered β in the bcc Ti-Nb-O system over compositions and temperatures. The effect of vibrational entropy on the phase stabilities of ordered and disordered phases in the hcp and bcc Ti-Nb-O systems will also be worth investigating. Certainly, the design of multi-component materials remains a challenging and complex process. Future research could include the incorporation of additional elements such as Al, Zr, and Sn into the hcp and bcc Ti-Nb-O systems, and controlling their concentrations to achieve the design of Ti-based high-entropy alloys. We believe that the findings and methodologies presented in this dissertation provide significant insights and references for the structural prediction and material design of multi-component Ti-based materials as well as other binary and multicomponent metallic alloys.

References

[1] Schutz, R. W. and Watkins, H. B. “Recent developments in titanium alloy application in the energy industry”. In: *Materials Science and Engineering: A* 243.1-2 (1998), pp. 305–315. DOI: 10.1016/S0921-5093(97)00819-8.

[2] Ribeiro, M. V., Moreira, M. R. V., and Ferreira, J. R. “Optimization of titanium alloy (6Al–4V) machining”. In: *Journal of Materials Processing Technology* 143 (2003), pp. 458–463. DOI: 10.1016/S0924-0136(03)00457-6.

[3] Rahman, M., Wang, Z. G., and Wong, Y. S. “A review on high-speed machining of titanium alloys”. In: *JSME International Journal Series C Mechanical Systems, Machine Elements and Manufacturing* 49.1 (2006), pp. 11–20. DOI: 10.1299/jsmec.49.11.

[4] Leyens, C. and Peters, M. *Titanium and titanium alloys: fundamentals and applications*. John Wiley & Sons, 2003. DOI: 10.1002/3527602119.

[5] Hao, Y. L., Li, S. J., Sun, S. Y., Zheng, C. Y., and Yang, R. “Elastic deformation behaviour of Ti–24Nb–4Zr–7.9Sn for biomedical applications”. In: *Acta Biomaterialia* 3.2 (2007), pp. 277–286. DOI: 10.1016/j.actbio.2006.11.002.

[6] Gurrappa, I. and Gogia, A. K. “High performance coatings for titanium alloys to protect against oxidation”. In: *Surface and Coatings Technology* 139.2-3 (2001), pp. 216–221. DOI: 10.1016/S0257-8972(00)01137-3.

[7] Donachie, M. J. *Titanium: a technical guide*. ASM international, 2000.

[8] Lütjering, G. and Williams, J. C. "Commercially pure (CP) titanium and alpha alloys". In: *Titanium* (2007), pp. 175–201. DOI: 10.1007/978-3-540-73036-1_4.

[9] Kaufman, J. G. and Rooy, E. L. *Aluminum alloy castings: properties, processes, and applications*. Asm International, 2004. DOI: 10.31399/asm.tb.aacppa.9781627083355.

[10] Cverna, F. *ASM ready reference: thermal properties of metals*. Asm International, 2002. URL: https://lccn.loc.gov/2002030544.

[11] Leyens, C. and Peters, M. *Titanium and titanium alloys: fundamentals and applications*. Wiley Online Library, 2006. DOI: 10.1002/3527602119.

[12] Boyer, R. R. "An overview on the use of titanium in the aerospace industry". In: *Materials Science and Engineering: A* 213.1-2 (1996), pp. 103–114. DOI: 10.1016/0921-5093(96)10233-1.

[13] Peters, M., Hemptenmacher, J., Kumpfert, J., and Leyens, C. "Structure and properties of titanium and titanium alloys". In: *Titanium and titanium alloys: fundamentals and applications* (2003), pp. 1–36. DOI: 10.1002/3527602119.ch1.

[14] Joshi, V. A. *Titanium alloys: an atlas of structures and fracture features*. Crc Press, 2006. DOI: 10.1201/9781420006063.

[15] Zhang, L. H., Rittel, D., and Osovski, S. "Thermo-mechanical characterization and dynamic failure of near α and near β titanium alloys". In: *Materials Science and Engineering: A* 729 (2018), pp. 94–101. DOI: 10.1016/j.msea.2018.05.007.

[16] Tabie, V. M., Li, C., Saifu, W., Li, J., and Xu, X. "Mechanical properties of near alpha titanium alloys for high-temperature applications-a review". In: *Aircraft Engineering and Aerospace Technology* 92.4 (2020), pp. 521–540. DOI: 10.1108/AEAT-04-2019-0086.

[17] Semiatin, S. L. “An overview of the thermomechanical processing of α/β titanium alloys: current status and future research opportunities”. In: *Metallurgical and Materials Transactions A* 51.6 (2020), pp. 2593–2625. DOI: 10.1007/s11661-020-05625-3.

[18] Veiga, C., Davim, J. P., and Loureiro, A. J. R. “Properties and applications of titanium alloys: a brief review”. In: *Reviews on Advanced Materials Science* 32.2 (2012), pp. 133–148. URL: https://www.elibrary.ru/rjotpp.

[19] Qian, J. “Ion Nitriding of Ti-10V-2Fe-3Al Alloy for Aerospace Applications”. In: (2013). URL: https://scholar.uwindsor.ca/etd/5039.

[20] Santhosh, R., Geetha, M., Saxena, V. K., and Nageswararao, M. “Studies on single and duplex aging of metastable beta titanium alloy Ti–15V–3Cr–3Al–3Sn”. In: *Journal of Alloys and Compounds* 605 (2014), pp. 222–229. DOI: 10.1016/j.jallcom.2014.03.183.

[21] Okamoto, H. “O-Ti (oxygen-titanium)”. In: *Journal of Phase Equilibria and Diffusion* 32.5 (2011), pp. 473–474. DOI: 10.1007/s11669-011-9935-5.

[22] Zhang, W. S., Zhu, Z. W., and Cheng, C. Y. “A literature review of titanium metallurgical processes”. In: *Hydrometallurgy* 108.3-4 (2011), pp. 177–188. DOI: 10.1016/j.hydromet.2011.04.005.

[23] Dai, J. J., Zhu, J. Y., Chen, C. Z., and Weng, F. “High temperature oxidation behavior and research status of modifications on improving high temperature oxidation resistance of titanium alloys and titanium aluminides: A review”. In: *Journal of Alloys and Compounds* 685 (2016), pp. 784–798. DOI: 10.1016/j.jallcom.2016.06.212.

[24] Wriedt, H. A. and Murray, J. L. “The N-Ti (nitrogen-titanium) system”. In: *Bulletin of Alloy Phase Diagrams* 8 (1987), pp. 378–388. DOI: 10.1007/BF02869274.

[25] San-Martin, A. and Manchester, F. D. "The H- Ti (hydrogen-titanium) system". In: *Bulletin of Alloy Phase Diagrams* 8.1 (1987), pp. 30–42. DOI: 10.1007/BF02868888.

[26] Murray, J. L., Liao, P. K., and Spear, K. E. "The B- Ti (boron-titanium) system". In: *Bulletin of Alloy Phase Diagrams* 7.6 (1986), pp. 550–555. DOI: 10.1007/BF02869864.

[27] Perez, R. A., Nakajima, H., and Dyment, F. "Diffusion in α-Ti and Zr". In: *Materials Transactions* 44.1 (2003), pp. 2–13. DOI: 10.2320/matertrans.44.2.

[28] Shenoy, R. N., Unnam, J., and Clark, R. K. "Oxidation and embrittlement of Ti-6Al-2Sn-4Zr-2Mo alloy". In: *Oxidation of metals* 26 (1986), pp. 105–124. DOI: 10.1007/BF00664276.

[29] Leyens, C., Peters, M., Weinem, D., and Kaysser, W. A. "Influence of long-term annealing on tensile properties and fracture of near-α titanium alloy Ti-6Al-2.75 Sn-4Zr-0.4 Mo-0.45 Si". In: *Metallurgical and Materials Transactions A* 27 (1996), pp. 1709–1717. DOI: 10.1007/BF02649829.

[30] Liu, Z. D. and Welsch, G. "Effects of oxygen and heat treatment on the mechanical properties of alpha and beta titanium alloys". In: *Metallurgical Transactions A* 19 (1988), pp. 527–542. DOI: 10.1007/BF02649267.

[31] Zhao, Z. Y., Hui, P. F., Wang, T., Wang, X., Xu, Y. H., Zhong, L. S., and Zhao, M. X. "New strategy to grow TiC coatings on titanium alloy: Contact solid carburization by cast iron". In: *Journal of Alloys and Compounds* 745 (2018), pp. 637–643. DOI: 10.1016/j.jallcom.2018.02.235.

[32] Vallejo, B., Gonzalez-Mañas, M., Martínez-López, J., Morales, F., and Caballero, M. A. "Characterization of TiO_2 deposited on textured silicon wafers by atmospheric pressure chemical vapour deposition". In: *Solar Energy Materials and Solar Cells* 86.3 (2005), pp. 299–308. DOI: 10.1016/j.solmat.2004.07.011.

[33] Karre, R., Niranjan, M. K., and Dey, S. R. “First principles theoretical investigations of low Young’s modulus beta Ti–Nb and Ti–Nb–Zr alloys compositions for biomedical applications”. In: *Materials Science and Engineering: C* 50 (2015), pp. 52–58. DOI: 10.1016/j.msec.2015.01.061.

[34] Kim, H. S., Kim, W. Y., and Lim, S. H. “Microstructure and elastic modulus of Ti–Nb–Si ternary alloys for biomedical applications”. In: *Scripta Materialia* 54.5 (2006), pp. 887–891. DOI: 10.1016/j.scriptamat.2005.11.001.

[35] Li, S. J., Hao, Y. L., Yang, R., Cui, Y. Y., and Niinomi, M. “Effect of Nb on microstructural characteristics of Ti-Nb-Ta-Zr alloy for biomedical applications”. In: *Materials Transactions* 43.12 (2002), pp. 2964–2969. DOI: 10.2320/matertrans.43.2964.

[36] Gasik, M. and Yu, H. “Phase Equilibria and Thermal Behaviour of Biomedical Ti-Nb-Zr Alloy”. In: *Proceedings 17th Plansee Seminar*. 2009, p. 29.

[37] Xu, S. H., Lu, T. T., Shen, K. J., Lan, J. J., Hu, B., Zhang, H. B., Tang, Y. P., Cao, H. Z., and Zheng, G. Q. “High temperature oxidation resistance of Ti-5553 alloy with electrodeposited SiO_2 coating”. In: *Materials Chemistry and Physics* 275 (2022), p. 125306. DOI: 10.1016/j.matchemphys.2021.125306.

[38] Tegner, B. E., Zhu, L., Siemers, C., Saksl, K., and Ackland, G. J. “High temperature oxidation resistance in titanium–niobium alloys”. In: *Journal of Alloys and Compounds* 643 (2015), pp. 100–105. DOI: 10.1016/j.jallcom.2015.04.115.

[39] Poulain, R., Delannoy, S., Guillot, I., Amann, F., Guillou, R., Lartigue-Korinek, S., Thiaudière, D., Béchade, J.-L., Clouet, E., and Prima, F. “First experimental evidence of oxygen ordering in dilute titanium–oxygen alloys”. In: *Materials Research Letters* 10.7 (2022), pp. 481–487. DOI: 10.1080/21663831.2022.2057202.

[40] Sun, J., Yao, Q., Xing, H., and Guo, W. Y. “Elastic properties of β, α'' and ω metastable phases in Ti–Nb alloy from first-principles”. In: *Journal of Physics: Condensed Matter* 19.48 (2007), p. 486215. DOI: 10.1088/0953-8984/19/48/486215.

[41] Yılmaz, E., Gökçe, A., Fındık, F., and Gülsoy, H. “Electrochemical Corrosion Behavior of Ti and Ti-16Nb Alloy for Implant Applications”. In: *8th International Advanced Technologies Symposium*. Vol. 8. Elazığ. 2017, pp. 2244–2251.

[42] Bönisch, M., Stoica, M., and Calin, M. “Routes to control diffusive pathways and thermal expansion in Ti-alloys”. In: *Scientific Reports* 10.1 (2020), p. 3045. DOI: 10.1038/s41598-020-60038-x.

[43] Korneva, A., Straumal, B., Gornakova, A., Kilmametov, A., Gondek, Ł., Lityńska-Dobrzyńska, L., Chulist, R., Pomorska, M., and Zięba, P. “Formation and thermal stability of the ω-phase in Ti–Nb and Ti–Mo alloys subjected to HPT”. In: *Materials* 15.12 (2022), p. 4136. DOI: 10.3390/ma15124136.

[44] Chinnappan, R., Panigrahi, B. K., and Van De Walle, A. “First-principles study of phase equilibrium in Ti–V, Ti–Nb, and Ti–Ta alloys”. In: *Calphad* 54 (2016), pp. 125–133. DOI: 10.1016/j.calphad.2016.07.001.

[45] Aperador, W., Yate, L., Pinzón, M. J., and Caicedo, J. C. “Optical and semiconductive properties of binary and ternary thin films from the Nb-Ti-O system”. In: *Results in Physics* 9 (2018), pp. 328–336. DOI: 10.1016/j.rinp.2018.02.060.

[46] Salloom, R., Reith, D., Banerjee, R., and Srinivasan, S. G. “First principles calculations on the effect of interstitial oxygen on phase stability and β–α'' martensitic transformation in Ti–Nb alloys”. In: *Journal of Materials Science* 53 (2018), pp. 11473–11487. DOI: 10.1007/s10853-018-2381-6.

[47] Marzari, N., Ferretti, A., and Wolverton, C. “Electronic-structure methods for materials design”. In: *Nature Materials* 20.6 (2021), pp. 736–749. DOI: 10.1038/s41563-021-01013-3.

[48] Ludena, E. V. “Is the Hohenberg–Kohn–Sham version of DFT a semi-empirical theory?” In: *Journal of Molecular Structure: THEOCHEM* 709.1-3 (2004), pp. 25–29. DOI: 10.1016/j.theochem.2004.03.047.

[49] Fang, C. M., Van Huis, M. A., Thijsse, B. J., and Zandbergen, H. W. “Stability and crystal structures of iron carbides: A comparison between the semi-empirical modified embedded atom method and quantum-mechanical DFT calculations”. In: *Physical Review B* 85.5 (2012), p. 054116. DOI: 10.1103/PhysRevB.85.054116.

[50] Shen, H. L., Xia, K., Wang, P., and Tan, R. R. “The electronic, structural, ferroelectric and optical properties of strontium and zirconium co-doped $BaTiO_3$: First-principles calculations”. In: *Solid State Communications* 355 (2022), p. 114930. DOI: 10.1016/j.ssc.2022.114930.

[51] Shin, D. W. and Wolverton, C. “First-principles density functional calculations for Mg alloys: A tool to aid in alloy development”. In: *Scripta Materialia* 63.7 (2010), pp. 680–685. DOI: 10.1016/j.scriptamat.2009.12.032.

[52] Wu, X. Y., Dou, Y. Y., Lian, R. Q., Wang, Y. Z., and Wei, Y. J. “Understanding rechargeable magnesium ion batteries via first-principles computations: A comprehensive review”. In: *Energy Storage Materials* 48 (2022), pp. 344–355. DOI: 10.1016/j.ensm.2022.03.039.

[53] Chen, S. M., Ma, Z. J., Qiu, S., Zhang, L. J., Zhang, S. Z., Yang, R., and Hu, Q. M. “Phase decomposition and strengthening in HfNbTaTiZr high entropy alloy from first-

principles calculations". In: *Acta Materialia* 225 (2022), p. 117582. DOI: 10.1016/j.actamat.2021.117582.

[54] Zhou, W. C., Souissi, M., Abe, T., Sahara, R., Sit, P. H. L., and Tsuchiya, K. "Evaluating the phase stability of binary titanium alloy Ti-X (X= Mo, Nb, Al, and Zr) using first-principles calculations and a Debye model". In: *Calphad* 71 (2020), p. 102207. DOI: 10.1016/j.calphad.2020.102207.

[55] Hui, J., Zhang, X. Y., Liu, T., Liu, W. G., and Wang, B. "First-principles calculation of twin boundary energy and strength/embrittlement in hexagonal close-packed titanium". In: *Materials & Design* 213 (2022), p. 110331. DOI: 10.1016/j.matdes.2021.110331.

[56] Sonwane, C. G., Wilcox, J., and Ma, Y. H. "Solubility of hydrogen in PdAg and PdAu binary alloys using density functional theory". In: *The Journal of Physical Chemistry B* 110.48 (2006), pp. 24549–24558. DOI: 10.1021/jp064507t.

[57] Wang, J., Yu, L. M., Liu, Y. C., Liu, C. X., Li, H. J., and Wu, J. F. "First-Principles Study of the Effect of Cr Content on Interstitial Oxygen Solution Behavior in Nb-Cr Alloys". In: *Materials Science Forum*. Vol. 913. Trans Tech Publ. 2018, pp. 582–588. DOI: 10.4028/www.scientific.net/MSF.913.582.

[58] Epifano, E. and Hug, G. "First-principle study of the solubility and diffusion of oxygen and boron in γ-TiAl". In: *Computational Materials Science* 174 (2020), p. 109475. DOI: 10.1016/j.commatsci.2019.109475.

[59] Wu, H. H. and Trinkle, D. R. "Solute effect on oxygen diffusion in α-titanium". In: *Journal of Applied Physics* 113.22 (2013). DOI: 10.1063/1.4808283.

[60] Sanchez, J. M., Ducastelle, F., and Gratias, D. "Generalized cluster description of multi-component systems". In: *Physica A: Statistical Mechanics and its Applications* 128.1-2 (1984), pp. 334–350. DOI: 10.1016/0378-4371(84)90096-7.

[61] Zunger, A. "First-principles statistical mechanics of semiconductor alloys and intermetallic compounds". In: *Statics and Dynamics of Alloy Phase Transformations*. Springer, 1994, pp. 361–419. DOI: 10.1007/978-1-4615-2476-2_23.

[62] Van De Walle, A., Asta, M., and Ceder, G. "The alloy theoretic automated toolkit: A user guide". In: *Calphad* 26.4 (2002), pp. 539–553. DOI: 10.1016/S0364-5916(02)80006-2.

[63] Sun, R. S., Woodward, C., and Van De Walle, A. "First-principles study on Ni_3Al (111) antiphase boundary with Ti and Hf impurities". In: *Physical Review B* 95.21 (2017), p. 214121. DOI: 10.1103/PhysRevB.95.214121.

[64] Dodaran, M., Ettefagh, A. H., Guo, S. M., Khonsari, M. M., Meng, W. J., Shamsaei, N., and Shao, S. "Effect of alloying elements on the γ' antiphase boundary energy in Ni-base superalloys". In: *Intermetallics* 117 (2020), p. 106670. DOI: 10.1016/j.intermet.2019.106670.

[65] Drautz, R., Reichert, H., Fähnle, M., Dosch, H., and Sanchez, J. M. "Spontaneous $L1_2$ Order at $Ni_{90}Al_{10}$ (110) Surfaces: An X-Ray and First-Principles-Calculation Study". In: *Physical Review Letters* 87.23 (2001), p. 236102. DOI: 10.1103/PhysRevLett.87.236102.

[66] Han, B. C., Van der Ven, A., Ceder, G., and Hwang, B. J. "Surface segregation and ordering of alloy surfaces in the presence of adsorbates". In: *Physical Review B* 72 (20 Nov. 2005), p. 205409. DOI: 10.1103/PhysRevB.72.205409.

[67] Lerch, D., Wieckhorst, O., Hammer, L., Heinz, K., and Müller, S. "Adsorbate cluster expansion for an arbitrary number of inequivalent sites". In: *Physical Review B* 78 (12 Sept. 2008), p. 121405. DOI: 10.1103/PhysRevB.78.121405.

[68] Müller, S., Wang, L. W., Zunger, A., and Wolverton, C. "Coherent phase stability in Al-Zn and Al-Cu fcc alloys: The role of the instability of fcc Zn". In: *Physical Review B* 60 (24 Dec. 1999), pp. 16448–16462. DOI: 10.1103/PhysRevB.60.16448.

[69] Van De Walle, A. and Asta, M. "Self-driven lattice-model Monte Carlo simulations of alloy thermodynamic properties and phase diagrams". In: *Modelling and Simulation in Materials Science and Engineering* 10.5 (2002), p. 521. DOI: 10.1088/0965-0393/10/5/304.

[70] Hoover, W. G. *Computational statistical mechanics*. Elsevier, 2012. URL: https://lccn.loc.gov/90027140.

[71] Landsberg, P. T. *Thermodynamics and statistical mechanics*. Courier Corporation, 1990. DOI: 10.1007/978-1-4612-0827-3.

[72] Abraham, F. F. "Computational statistical mechanics methodology, applications and supercomputing". In: *Advances in Physics* 35.1 (1986), pp. 1–111. DOI: 10.1080/00018738600101851.

[73] Aleksandr, I. and Khinchin, A. *Mathematical foundations of statistical mechanics*. Courier Corporation, 1949. URL: https://lccn.loc.gov/49009707.

[74] Ballentine, L. E. "The statistical interpretation of quantum mechanics". In: *Reviews of Modern Physics* 42.4 (1970), p. 358. DOI: 10.1103/RevModPhys.42.358.

[75] Gentle, J. E. "Monte carlo methods". In: *Random Number Generation and Monte Carlo methods* (2003), pp. 229–281. DOI: 10.1007/0-387-21610-3_7.

[76] Shapiro, A. "Monte Carlo sampling methods". In: *Handbooks in Operations Research and Management Science* 10 (2003), pp. 353–425. DOI: 10.1016/S0927-0507(03)10006-0.

[77] Metropolis, N., Rosenbluth, A. W., Rosenbluth, M. N., Teller, A. H., and Teller, E. "Equation of state calculations by fast computing machines". In: *The Journal of Chemical Physics* 21.6 (1953), pp. 1087–1092. DOI: 10.1063/1.1699114.

[78] Fishman, G. *Monte Carlo: concepts, algorithms, and applications*. Springer Science & Business Media, 2013. DOI: 10.1007/978-1-4757-2553-7.

[79] Graham, C. and Talay, D. *Stochastic simulation and Monte Carlo methods: mathematical foundations of stochastic simulation*. Vol. 68. Springer Science & Business Media, 2013. DOI: 10.1007/978-3-642-39363-1.

[80] Hammersley, J. *Monte carlo methods*. Springer Science & Business Media, 2013. DOI: 10.1007/978-94-009-5819-7.

[81] Rajabi, M. M. and Ataie-Ashtiani, B. "Sampling efficiency in Monte Carlo based uncertainty propagation strategies: application in seawater intrusion simulations". In: *Advances in Water Resources* 67 (2014), pp. 46–64. DOI: 10.1016/j.advwatres.2014.02.004.

[82] Miras, H., Jiménez, R., Miras, C., and Gomà, C. "CloudMC: a cloud computing application for Monte Carlo simulation". In: *Physics in Medicine & Biology* 58.8 (2013), N125. DOI: 10.1088/0031-9155/58/8/N125.

[83] Hung, Y. C. "A review of Monte Carlo and quasi-Monte Carlo sampling techniques". In: *Wiley Interdisciplinary Reviews: Computational Statistics* 16.1 (2024), e1637. DOI: 10.1002/wics.1637.

[84] Drummond, N. D., Monserrat, B., Lloyd-Williams, J. H., Ríos, P. L., Pickard, C. J., and Needs, R. J. "Quantum Monte Carlo study of the phase diagram of solid molecular hydrogen at extreme pressures". In: *Nature Communications* 6.1 (2015), p. 7794. DOI: 10.1038/ncomms8794.

[85] Heinisch, H. L., Singh, B. N., and Golubov, S. I. "A kinetic Monte Carlo study of mixed 1D/3D defect migration". In: *Journal of Computer-Aided Materials Design* 6 (1999), pp. 277–282. DOI: 10.1023/A:1008777901639.

[86] Scotti, L. and Mottura, A. “Interstitial diffusion of O, N, and C in α-Ti from first-principles: Analytical model and kinetic Monte Carlo simulations”. In: *The Journal of Chemical Physics* 144.8 (2016). DOI: 10.1063/1.4942030.

[87] Wierzchowski, S. J. and Monson, P. A. “Calculation of free energies and chemical potentials for gas hydrates using Monte Carlo simulations”. In: *The Journal of Physical Chemistry B* 111.25 (2007), pp. 7274–7282. DOI: 10.1021/jp068325a.

[88] Chandran, M., Subramanian, P. R., and Gigliotti, M. F. “Energetics of interstitial oxygen in β-TiX (X= transition elements) alloys using first principles methods”. In: *Journal of Alloys and Compounds* 571 (2013), pp. 107–113. DOI: 10.1016/j.jallcom.2013.03.140.

[89] Avner, S. H. *Introduction to physical metallurgy*. Vol. 2. McGraw-hill New York, 1974.

[90] Gunda, N. S. H., Levi, C. G., and Van Der Ven, A. “Investigating the electronic origins of the repulsion between substitutional and interstitial solutes in hcp Ti”. In: *Physical Review Materials* 5.7 (2021), p. 073604. DOI: 10.1103/PhysRevMaterials.5.073604.

[91] Zhou, W. C., Sahara, R., and Tsuchiya, K. “First-principles study of the phase stability and elastic properties of Ti-X alloys (X= Mo, Nb, Al, Sn, Zr, Fe, Co, and O)”. In: *Journal of Alloys and Compounds* 727 (2017), pp. 579–595. DOI: 10.1016/j.jallcom.2017.08.128.

[92] Kleppner, D. and Jackiw, R. “One hundred years of quantum physics”. In: *Science* 289.5481 (2000), pp. 893–898. DOI: 10.1126/science.289.5481.893.

[93] Kussow, A. G. “Many-Electron Problem in an Atomic Lattice Reduced Exactly to Two-Particle Pseudo-Electron Excitations: Key to Alternative First-Principles Methods”. In: *New Advances in Semiconductors* (2022), p. 3. DOI: 10.5772/intechopen.103045.

[94] Ashcroft, N. W. and Mermin, N. D. “Solid State Physics, College edn”. In: *Thomson Learning Inc* (1976).

[95] Martin, R. M. *Electronic structure: basic theory and practical methods*. IEEE, 2020. DOI: 10.1109/MCD.2006.1708383.

[96] Lykos, P. and Pratt, G. W. "Discussion on the Hartree-Fock approximation". In: *Reviews of Modern Physics* 35.3 (1963), p. 496. DOI: 10.1103/RevModPhys.35.496.

[97] Sherrill, C. D. and Schaefer III, H. F. "The configuration interaction method: Advances in highly correlated approaches". In: *Advances in quantum chemistry*. Vol. 34. Elsevier, 1999, pp. 143–269. DOI: 10.1016/S0065-3276(08)60532-8.

[98] Čížek, J. "On the correlation problem in atomic and molecular systems. Calculation of wavefunction components in Ursell-type expansion using quantum-field theoretical methods". In: *The Journal of Chemical Physics* 45.11 (1966), pp. 4256–4266. DOI: doi.org/10.1063/1.1727484.

[99] Essén, H. "The physics of the Born–Oppenheimer approximation". In: *International Journal of Quantum Chemistry* 12.4 (1977), pp. 721–735. DOI: 10.1002/qua.560120410.

[100] Hohenberg, P. and Kohn, W. "Inhomogeneous electron gas". In: *Physical Review* 136.3B (1964), B864. DOI: 10.1103/PhysRev.136.B864.

[101] Kohn, W. and Sham, L. J. "Self-consistent equations including exchange and correlation effects". In: *Physical Review* 140.4A (1965), A1133. DOI: 10.1103/PhysRev.140.A1133.

[102] Besalú, E. and Martí, J. "Exploring the rayleigh-ritz variational principle". In: *Journal of Chemical Education* 75.1 (1998), p. 105. DOI: 10.1021/ed075p105.

[103] Burke, K. and Wagner, L. O. "DFT in a nutshell". In: *International Journal of Quantum Chemistry* 113.2 (2013), pp. 96–101. DOI: doi.org/10.1002/qua.24259.

[104] Becke, A. D. "Perspective: Fifty years of density-functional theory in chemical physics". In: *The Journal of Chemical Physics* 140.18 (2014). DOI: 10.1063/1.4869598.

[105] Perdew, J. P., Chevary, J. A., Vosko, S. H., Jackson, K. A., Pederson, M. R., Singh, D. J., and Fiolhais, C. "Atoms, molecules, solids, and surfaces: Applications of the generalized gradient approximation for exchange and correlation". In: *Physical Review B* 46.11 (1992), p. 6671. DOI: 10.1103/PhysRevB.46.6671.

[106] Becke, A. D. "Density-functional exchange-energy approximation with correct asymptotic behavior". In: *Physical Review A* 38.6 (1988), p. 3098. DOI: 10.1103/PhysRevA.38.3098.

[107] Langreth, D. C. and Mehl, M. J. "Beyond the local-density approximation in calculations of ground-state electronic properties". In: *Physical Review B* 28.4 (1983), p. 1809. DOI: 10.1103/PhysRevB.28.1809.

[108] Perdew, J. P., Burke, K., and Ernzerhof, M. "Generalized gradient approximation made simple". In: *Physical Review Letters* 77.18 (1996), p. 3865. DOI: 10.1103/PhysRevLett.77.3865.

[109] Yang, J., Tan, L. Z., and Rappe, A. M. "Hybrid functional pseudopotentials". In: *Physical Review B* 97.8 (2018), p. 085130. DOI: 10.1103/PhysRevB.97.085130.

[110] Harrison, W. A. *Electronic structure and the properties of solids: the physics of the chemical bond*. Courier Corporation, 2012. URL: https://lccn.loc.gov/89034153.

[111] Matta, C. F. and Gillespie, R. J. "Understanding and interpreting molecular electron density distributions". In: *Journal of Chemical Education* 79.9 (2002), p. 1141. DOI: 10.1021/ed079p1141.

[112] Singh, D. J. and Nordstrom, L. *Planewaves, Pseudopotentials, and the LAPW method*. Springer Science & Business Media, 2006. URL: https://www.osti.gov/biblio/978055.

[113] Böer, K. W. and Pohl, U. W. "Quantum Mechanics of Electrons in Crystals". In: *Semiconductor Physics*. Springer, 2023, pp. 219–255. DOI: 10.1007/978-3-031-18286-0_7.

[114] Hamann, D. R., Schlüter, M., and Chiang, C. "Norm-conserving pseudopotentials". In: *Physical Review Letters* 43.20 (1979), p. 1494. DOI: 10.1103/PhysRevLett.43.1494.

[115] Kresse, G. and Joubert, D. "From ultrasoft pseudopotentials to the projector augmented-wave method". In: *Physical Review B* 59.3 (1999), p. 1758. DOI: 10.1103/PhysRevB.59.1758.

[116] Blöchl, P. E. "Projector augmented-wave method". In: *Physical Review B* 50.24 (1994), p. 17953. DOI: 10.1103/PhysRevB.50.17953.

[117] Vanderbilt, D. "Soft self-consistent pseudopotentials in a generalized eigenvalue formalism". In: *Physical Review B* 41.11 (1990), p. 7892. DOI: 10.1103/PhysRevB.41.7892.

[118] Kresse, G. and Hafner, J. "Ab initio molecular dynamics for liquid metals". In: *Physical Review B* 47.1 (1993), p. 558. DOI: 10.1103/PhysRevB.47.558.

[119] Kresse, G. and Hafner, J. "Ab initio molecular-dynamics simulation of the liquid-metal–amorphous-semiconductor transition in germanium". In: *Physical Review B* 49.20 (1994), p. 14251. DOI: 10.1103/PhysRevB.49.14251.

[120] Kresse, G. and Furthmüller, J. "Efficient iterative schemes for ab initio total-energy calculations using a plane-wave basis set". In: *Physical Review B* 54.16 (1996), p. 11169. DOI: 10.1103/PhysRevB.54.11169.

[121] Kresse, G. and Furthmüller, J. "Efficiency of ab-initio total energy calculations for metals and semiconductors using a plane-wave basis set". In: *Computational Materials Science* 6.1 (1996), pp. 15–50. DOI: 10.1016/0927-0256(96)00008-0.

[122] Van De Walle, A. and Ceder, G. "Automating first-principles phase diagram calculations". In: *Journal of Phase Equilibria* 23.4 (2002), p. 348. DOI: 10.1361/105497102770331596.

[123] Van De Walle, A. "Multicomponent multisublattice alloys, nonconfigurational entropy and other additions to the Alloy Theoretic Automated Toolkit". In: *Calphad* 33.2 (2009), pp. 266–278. DOI: 10.1016/j.calphad.2008.12.005.

[124] Van De Walle, A. "Methods for first-principles alloy thermodynamics". In: *Jom* 65 (2013), pp. 1523–1532. DOI: 10.1007/s11837-013-0764-3.

[125] Lavrentiev, M. Y., Nguyen-Manh, D., and Dudarev, S. L. "Cluster expansion models for Fe–Cr alloys, the prototype materials for a fusion power plant". In: *Computational Materials Science* 49.4 (2010), S199–S203. DOI: 10.1016/j.commatsci.2010.04.033.

[126] Wolverton, C. and Didier, D. F. "Cluster expansions of alloy energetics in ternary intermetallics". In: *Physical Review B* 49.13 (1994), p. 8627. DOI: 10.1103/PhysRevB.49.8627.

[127] Leong, Z. D. and Tan, T. L. "Robust cluster expansion of multicomponent systems using structured sparsity". In: *Physical Review B* 100.13 (2019), p. 134108. DOI: 10.1103/PhysRevB.100.134108.

[128] Garbulsky, G. D. and Ceder, G. "Linear-programming method for obtaining effective cluster interactions in alloys from total-energy calculations: Application to the fcc Pd-V system". In: *Physical Review B* 51.1 (1995), p. 67. DOI: 10.1103/PhysRevB.51.67.

[129] Sanchez, J. M. and Mohri, T. "Approximate solutions to the cluster variation free energies by the variable basis cluster expansion". In: *Computational Materials Science* 122 (2016), pp. 301–306. DOI: 10.1016/j.commatsci.2016.05.035.

[130] Milligan, G. W., Soon, S. C., and Sokol, L. M. "The effect of cluster size, dimensionality, and the number of clusters on recovery of true cluster structure". In: *IEEE Transactions on Pattern Analysis and Machine Intelligence* 1 (1983), pp. 40–47. DOI: 10.1109/TPAMI.1983.4767342.

[131] Zhang, N. and Mottura, A. "First-principles thermodynamic investigation on the α phases in TiO and TiNb binary system". In: *The Journal of Chemical Physics* 160.19 (2024). DOI: 10.1063/5.0203644.

[132] Ghosh, G., Van De Walle, A., and Asta, M. "First-principles calculations of the structural and thermodynamic properties of bcc, fcc and hcp solid solutions in the Al–TM (TM= Ti, Zr and Hf) systems: a comparison of cluster expansion and supercell methods". In: *Acta Materialia* 56.13 (2008), pp. 3202–3221. DOI: 10.1016/j.actamat.2008.03.006.

[133] Prysyazhnyuk, P., Bishchak, R., Korniy, S., Panchuk, M., and Kaspruk, V. "Virtual crystal approximation study of the complex refractory carbides based on Ti-Nb-Mo-VC system with CASTEP computer code." In: *ITTAP*. 2021, pp. 300–305.

[134] Wang, S., Xiong, J., Li, D., Zeng, Q., Xiong, M., and Chai, X. S. "Comparison of two calculation models for high entropy alloys: Virtual crystal approximation and special quasi-random structure". In: *Materials Letters* 282 (2021), p. 128754. DOI: 10.1016/j.matlet.2020.128754.

[135] Singh, P. P. and Gonis, A. "Effective cluster interactions using the generalized perturbation method in the atomic-sphere approximation". In: *Physical Review B* 47.11 (1993), p. 6744. DOI: 10.1103/PhysRevB.47.6744.

[136] Connolly, J. W. D. and Williams, A. R. "Density-functional theory applied to phase transformations in transition-metal alloys". In: *Physical Review B* 27.8 (1983), p. 5169. DOI: 10.1103/PhysRevB.27.5169.

[137] Kleiven, D., Akola, J., Peterson, A. A., Vegge, T., and Chang, J. H. "Training sets based on uncertainty estimates in the cluster-expansion method". In: *Journal of Physics: Energy* 3.3 (2021), p. 034012. DOI: 10.1088/2515-7655/abf9ef.

[138] Honeycutt, J. D. and Andersen, H. C. "Molecular dynamics study of melting and freezing of small Lennard-Jones clusters". In: *Journal of Physical Chemistry* 91.19 (1987), pp. 4950–4963. DOI: 10.1021/j100303a014.

[139] Larsen, P. M. "Revisiting the common neighbour analysis and the centrosymmetry parameter". In: *arXiv preprint arXiv:2003.08879* (2020). DOI: 10.48550/arXiv.2003.08879.

[140] Stukowski, A. "Structure identification methods for atomistic simulations of crystalline materials". In: *Modelling and Simulation in Materials Science and Engineering* 20.4 (2012), p. 045021. DOI: 10.1088/0965-0393/20/4/045021.

[141] Nataraj, C., Borda, E. J. L., Van De Walle, A., and Samanta, A. "A systematic analysis of phase stability in refractory high entropy alloys utilizing linear and non-linear cluster expansion models". In: *Acta Materialia* 220 (2021), p. 117269. DOI: 10.1016/j.actamat.2021.117269.

[142] Moruzzi, V. L., Janak, J. F., and Schwarz, K. "Calculated thermal properties of metals". In: *Physical Review B* 37.2 (1988), p. 790. DOI: 10.1103/PhysRevB.37.790.

[143] Lu, X. G., Selleby, M., and Sundman, B. "Theoretical modeling of molar volume and thermal expansion". In: *Acta Materialia* 53.8 (2005), pp. 2259–2272. DOI: 10.1016/j.actamat.2005.01.049.

[144] Otero-De-La-Roza, A., Abbasi-Pérez, D., and Luaña, V. "Gibbs2: A new version of the quasiharmonic model code. II. Models for solid-state thermodynamics, features

and implementation". In: *Computer Physics Communications* 182.10 (2011), pp. 2232–2248. DOI: 10.1016/j.cpc.2011.05.009.

[145] Otero-de-la-Roza, A. and Luaña, V. "Gibbs2: A new version of the quasi-harmonic model code. I. Robust treatment of the static data". In: *Computer Physics Communications* 182.8 (2011), pp. 1708–1720. DOI: 10.1016/j.cpc.2011.04.016.

[146] Herper, H. C., Hoffmann, E., and Entel, P. "Ab initio full-potential study of the structural and magnetic phase stability of iron". In: *Physical Review B* 60.6 (1999), p. 3839. DOI: 10.1103/PhysRevB.60.3839.

[147] Slater, J. C. *Introduction to chemical physics*. International series in pure and applied physics. McGraw-Hill, 1939. URL: https://cir.nii.ac.jp/crid/1130282272895396608.

[148] Dugdale, J. S. and MacDonald, D. K. C. "The thermal expansion of solids". In: *Physical Review* 89.4 (1953), p. 832. DOI: 10.1103/PhysRev.89.832.

[149] Vashchenko, V. Y. and Zubarev, V. "On grüneisen coefficient". In: *Fizika tverdogo tela* 5 (1963), pp. 886–890.

[150] Vocadlo, L., Poirer, J. P., and Price, G. D. "Gruneisen parameters and isothermal equations of state". In: *American Mineralogist* 85.2 (2000), pp. 390–395. DOI: 10.2138/am-2000-2-319.

[151] Landau, D. and Binder, K. *A Guide to Monte Carlo Simulations in Statistical Physics*. USA: Cambridge University Press, 2005. DOI: 10.1017/CBO9781139696463.

[152] Kofke, D. A. and Glandt, E. D. "Monte Carlo simulation of multicomponent equilibria in a semigrand canonical ensemble". In: *Molecular Physics* 64.6 (1988), pp. 1105–1131. DOI: 10.1080/00268978800100743.

[153] Mathé, P. and Novak, E. "Simple Monte Carlo and the metropolis algorithm". In: *Journal of Complexity* 23.4-6 (2007), pp. 673–696. DOI: 10.1016/j.jco.2007.05.002.

[154] Dalton, A. S., Belak, A. A., and Anton, V. D. V. "Thermodynamics of lithium in TiO_2(B) from first principles". In: *Chemistry of Materials* 24.9 (2012), pp. 1568–1574. DOI: 10.1021/cm203283v.

[155] Methfessel, M. P. A. T. and Paxton, A. T. "High-precision sampling for Brillouin-zone integration in metals". In: *physical Review B* 40.6 (1989), p. 3616. DOI: 10.1103/PhysRevB.40.3616.

[156] Blöchl, P. E., Jepsen, O., and Andersen, O. K. "Improved tetrahedron method for Brillouin-zone integrations". In: *Physical Review B* 49.23 (1994), p. 16223. DOI: 10.1103/PhysRevB.49.16223.

[157] Burton, B. P. and Van De Walle, A. "First principles phase diagram calculations for the octahedral-interstitial system αTiO_X, O≤X≤1/2". In: *Calphad* 39 (2012), pp. 97–103. DOI: 10.1016/j.calphad.2012.09.004.

[158] Burton, B. P., Van De Walle, A., and Harold, T. S. "First Principles phase diagram calculations for the octahedral-interstitial system ZrO_X, 0≤X≤1/2". In: *Journal of the Physical Society of Japan* 81.1 (2011), p. 014004. DOI: 10.1143/JPSJ.81.014004.

[159] Burton, B. P. and Van De Walle, A. "First principles phase diagram calculations for the octahedral-interstitial system HfO_X, 0≤X≤1/2". In: *Calphad* 37 (2012), pp. 151–157. DOI: 10.1016/j.calphad.2011.12.011.

[160] Tsuji, T. "Thermochemistry of IVA transition metal-oxygen solid solutions". In: *Journal of Nuclear Materials* 247 (1997), pp. 63–71. DOI: 10.1016/S0022-3115(97)00064-0.

[161] Yamaguchi, S. “Interstitial Order-Disorder Transformation in the Ti–O Solid Solution. I. Ordered Arrangement of Oxygen”. In: *Journal of the Physical Society of Japan* 27.1 (1969), pp. 155–163. DOI: 10.1143/JPSJ.27.155.

[162] Czerwinski, F. “Thermal stability of aluminum alloys”. In: *Materials* 13.15 (2020), p. 3441. DOI: 10.3390/ma13153441.

[163] Adetunji, B. I., Adebambo, P. O., and Adebayo, G. A. “First principles studies of band structure and electronic properties of ZnSe”. In: *Journal of Alloys and Compounds* 513 (2012), pp. 294–299. DOI: 10.1016/j.jallcom.2011.10.039.

[164] Dong, K., Benson, A. R., and Bindel, D. “Network density of states”. In: *Proceedings of the 25th ACM SIGKDD International Conference on Knowledge Discovery & Data Mining*. 2019, pp. 1152–1161. DOI: 10.1145/3292500.3330891.

[165] Oddershede, J. and Larsen, S. “Charge density study of naphthalene based on X-ray diffraction data at four different temperatures and theoretical calculations”. In: *The Journal of Physical Chemistry A* 108.6 (2004), pp. 1057–1063. DOI: 10.1021/jp036186g.

[166] Tang, W., Sanville, E., and Henkelman, G. “A grid-based Bader analysis algorithm without lattice bias”. In: *Journal of Physics: Condensed Matter* 21.8 (2009), p. 084204. DOI: 10.1088/0953-8984/21/8/084204.

[167] Henkelman, G., Arnaldsson, A., and Jónsson, H. “A fast and robust algorithm for Bader decomposition of charge density”. In: *Computational Materials Science* 36.3 (2006), pp. 354–360. DOI: 10.1016/j.commatsci.2005.04.010.

[168] Petkov, V., Maswadeh, Y., Vargas, J. A., Shan, S., Kareem, H., Wu, Z. P., Luo, J., Zhong, C. J., Shastri, S., and Kenesei, P. “Deviations from Vegard’s law and evolution of the electrocatalytic activity and stability of Pt-based nanoalloys inside fuel cells

by in operando X-ray spectroscopy and total scattering". In: *Nanoscale* 11.12 (2019), pp. 5512–5525. DOI: 10.1039/C9NR01069F.

[169] Castellanos, M. and West, A. R. "Deviations from Vegard's law in oxide solid solutions. The systems Li_2TiO_3–MgO and Li_2TiO_3–Na_2TiO_3". In: *Journal of the Chemical Society, Faraday Transactions 1: Physical Chemistry in Condensed Phases* 76 (1980), pp. 2159–2169. DOI: 10.1039/F19807602159.

[170] Langmuir, I. "Oscillations in ionized gases". In: *Proceedings of the National Academy of Sciences* 14.8 (1928), pp. 627–637. DOI: 10.1073/pnas.14.8.627.

[171] Goyal, M. and Gupta, B. R. K. "Shape, size and temperature dependency of thermal expansion, lattice parameter and bulk modulus in nanomaterials". In: *Pramana* 90 (2018), pp. 1–8. DOI: 10.1007/s12043-018-1563-8.

[172] Garrett, C. "Nonlinear optics, anharmonic oscillators, and pyroelectricity". In: *IEEE Journal of Quantum Electronics* 4.3 (1968), pp. 70–84. DOI: 10.1109/JQE.1968.1075030.

[173] Cowley, R. A. "The lattice dynamics of an anharmonic crystal". In: *Advances in Physics* 12.48 (1963), pp. 421–480. DOI: 10.1080/00018736300101333.

[174] Lu, X. G., Selleby, M., and Sundman, B. "Calculations of thermophysical properties of cubic carbides and nitrides using the Debye–Grüneisen model". In: *Acta Materialia* 55.4 (2007), pp. 1215–1226. DOI: 10.1016/j.actamat.2006.05.054.

[175] Birch, F. "Finite elastic strain of cubic crystals". In: *Physical Review* 71.11 (1947), p. 809. DOI: 10.1103/PhysRev.71.809.

[176] Tang, S. L., Li, Y. F., Wang, Y. R., Gao, Y. M., Zheng, Q. L., and Yi, D. W. "Theoretical study of mechanical and thermodynamic properties of titanium oxides Ti_xO_y". In: *Ma-*

terials Chemistry and Physics 213 (2018), pp. 538–547. DOI: 10.1016/j.matchemphys.2018.01.038.

[177] Andersson, D. A., Korzhavyi, P. A., and Johansson, B. "Thermodynamics of structural vacancies in titanium monoxide from first-principles calculations". In: *Physical Review B* 71.14 (2005), p. 144101. DOI: 10.1103/PhysRevB.71.144101.

[178] Mei, Z. G., Shang, S. L., Wang, Y., and Liu, Z. K. "Density-functional study of the pressure-induced phase transitions in Ti at zero Kelvin". In: *Physical Review B* 79.13 (2009), p. 134102. DOI: 10.1103/PhysRevB.79.134102.

[179] Jain, A., Ong, S. P., Hautier, G., Chen, W., Richards, W. D., Dacek, S., Cholia, S., Gunter, D., Skinner, D., and Ceder, G. "Commentary: The Materials Project: A materials genome approach to accelerating materials innovation". In: *APL Materials* 1.1 (2013). DOI: 10.1063/1.4812323.

[180] Chaplot, S. L., Mittal, R., and Choudhury, N. "Thermodynamic properties of solids: Experiment and modeling". In: *Thermodynamic Properties of Solids: Experiment and Modeling* (2010), pp. 1–5. DOI: 10.1002/9783527630417.

[181] Van De Walle, A. and Ceder, G. "The effect of lattice vibrations on substitutional alloy thermodynamics". In: *Reviews of Modern Physics* 74.1 (2002), p. 11. DOI: 10.1103/RevModPhys.74.11.

[182] Mittal, R., Gupta, M. K., and Chaplot, S. L. "Phonons and anomalous thermal expansion behaviour in crystalline solids". In: *Progress in Materials Science* 92 (2018), pp. 360–445. DOI: 10.1016/j.pmatsci.2017.10.002.

[183] Flynn, T. *Cryogenic engineering, revised and expanded*. CRC Press, 2004. DOI: 10.1201/9780203026991.

[184] Gunda, N. S. H., Puchala, B., and Van Der Ven, A. "Resolving phase stability in the Ti-O binary with first-principles statistical mechanics methods". In: *Physical Review Materials* 2.3 (2018), p. 033604. DOI: 10.1103/PhysRevMaterials.2.033604.

[185] Ruban, A. V., Baykov, V. I., Johansson, B., Dmitriev, V. V., and Blanter, M. S. "Oxygen and nitrogen interstitial ordering in hcp Ti, Zr, and Hf: An ab initio study". In: *Physical Review B* 82.13 (2010), p. 134110. DOI: 10.1103/PhysRevB.82.134110.

[186] Sanchez, J. M., Stark, J. P., and Moruzzi, V. L. "First-principles calculation of the Ag-Cu phase diagram". In: *Physical Review B* 44.11 (1991), p. 5411. DOI: 10.1103/PhysRevB.44.5411.

[187] Asta, M., McCormack, R., and De Fontaine, D. "Theoretical study of alloy phase stability in the Cd-Mg system". In: *Physical Review B* 48.2 (1993), p. 748. DOI: 10.1103/PhysRevB.48.748.

[188] Colinet, C., Eymery, J., Pasturel, A., Paxton, A. T., and Van Schilfgaarde, M. "A first-principles phase stability study on the Au-Ni system". In: *Journal of Physics: Condensed Matter* 6.6 (1994), p. L47. DOI: 10.1088/0953-8984/6/6/003.

[189] Matlakhova, L. A., Matlakhov, A. N., Monteiro, S. N., Fedotov, S. G., and Goncharenko, B. A. "Properties and structural characteristics of Ti–Nb–Al alloys". In: *Materials Science and Engineering: A* 393.1-2 (2005), pp. 320–326. DOI: 10.1016/j.msea.2004.11.021.

[190] Van De Walle, A., Tiwary, P., De Jong, M., Olmsted, D. L., Asta, M., Dick, A., Shin, D., Wang, Y., Chen, L. Q., and Liu, Z. K. "Efficient stochastic generation of special quasirandom structures". In: *Calphad* 42 (2013), pp. 13–18. DOI: 10.1016/j.calphad.2013.06.006.

[191] Gunda, N. S. H. and Van Der Ven, A. “First-principles insights on phase stability of titanium interstitial alloys”. In: *Physical Review Materials* 2.8 (2018), p. 083602. DOI: 10.1103/PhysRevMaterials.2.083602.

[192] Nemla, F. and Cherrad, D. “First principles study of structural, elastic, electronic, and optical properties of the cubic perovskites AVO_3 (A= Ca and La)”. In: *Emergent Materials* 5.1 (2022), pp. 175–186. DOI: 10.1007/s42247-022-00369-9.

[193] Brumme, T., Calandra, M., and Mauri, F. “First-principles theory of field-effect doping in transition-metal dichalcogenides: Structural properties, electronic structure, Hall coefficient, and electrical conductivity”. In: *Physical Review B* 91.15 (2015), p. 155436. DOI: 10.1103/PhysRevB.91.155436.

[194] Peres, N. M. R., Guinea, F., and Castro Neto, A. H. “Electronic properties of disordered two-dimensional carbon”. In: *Physical Review B* 73.12 (2006), p. 125411. DOI: 10.1103/PhysRevB.73.125411.

[195] Zunger, A., Wei, S. H., Ferreira, L. G., and Bernard, J. E. “Special quasirandom structures”. In: *Physical Review Letters* 65.3 (1990), p. 353. DOI: 10.1103/PhysRevLett.65.353.

[196] Wei, S. H., Ferreira, L. G., Bernard, J. E., and Zunger, A. “Electronic properties of random alloys: Special quasirandom structures”. In: *Physical Review B* 42.15 (1990), p. 9622. DOI: 10.1103/PhysRevB.42.9622.

[197] Li, K. M. and Fu, C. C. “Ground-state properties and lattice-vibration effects of disordered Fe-Ni systems for phase stability predictions”. In: *Physical Review Materials* 4.2 (2020), p. 023606. DOI: 10.1103/PhysRevMaterials.4.023606.

[198] Biroli, G. “In search of the perfect glass”. In: *Nature Physics* 10.8 (2014), pp. 555–556. DOI: 10.1038/nphys3054.

[199] Zhang, S. Z., Cui, H., Li, M. M., Yu, H., Vitos, L., Yang, R., and Hu, Q. M. "First-principles study of phase stability and elastic properties of binary Ti-xTM (TM= V, Cr, Nb, Mo) and ternary Ti-15TM-yAl alloys". In: *Materials & Design* 110 (2016), pp. 80–89. DOI: 10.1016/j.matdes.2016.07.120.

[200] Kumar, K. C. H., Wollants, P., and Delaey, L. "Thermodynamic calculation of Nb-Ti-V phase diagram". In: *Calphad* 18.1 (1994), pp. 71–79. DOI: 10.1016/0364-5916(94)90008-6.

[201] Wang, J. S., Xiao, W. L., Ren, L., Fu, Y., and Ma, C. L. "The roles of oxygen content on microstructural transformation, mechanical properties and corrosion resistance of Ti-Nb-based biomedical alloys with different β stabilities". In: *Materials Characterization* 176 (2021), p. 111122. DOI: 10.1016/j.matchar.2021.111122.

[202] Kadkhodaei, S. and Van De Walle, A. "Software tools for thermodynamic calculation of mechanically unstable phases from first-principles data". In: *Computer Physics Communications* 246 (2020), p. 106712. DOI: 10.1016/j.cpc.2019.01.008.

[203] Hafner, J. "Ab-initio simulations of materials using VASP: Density-functional theory and beyond". In: *Journal of Computational Chemistry* 29.13 (2008), pp. 2044–2078. DOI: 10.1002/jcc.21057.

[204] Wolverton, C. and Zunger, A. "First-principles prediction of vacancy order-disorder and intercalation battery voltages in Li_xCoO_2". In: *Physical Review Letters* 81.3 (1998), p. 606. DOI: 10.1103/PhysRevLett.81.606.

[205] Han, N., Zhang, W., Guo, W., Pan, H., Jiang, B., Xing, L. B., Tian, H., Wang, G. X., Zhang, X., and Fransaer, J. "Designing oxide catalysts for oxygen electrocatalysis: insights from mechanism to application". In: *Nano-Micro Letters* 15.1 (2023), p. 185. DOI: 10.1007/s40820-023-01152-z.

[206] Kim, Y., Choi, E., Kim, S., and Byon, H. R. "Layered transition metal oxides (LTMO) for oxygen evolution reactions and aqueous Li-ion batteries". In: *Chemical Science* 14.39 (2023), pp. 10644–10663. DOI: 10.1039/D3SC03220E.

[207] Wang, H. X., Zhang, K. H. L., Hofmann, J. P., and Oropeza, F. E. "The electronic structure of transition metal oxides for oxygen evolution reaction". In: *Journal of Materials Chemistry A* 9.35 (2021), pp. 19465–19488. DOI: 10.1039/D1TA03732C.

[208] Zhao, P. J., Zheng, J. M., Guo, P., Jiang, Z. Y., Cao, L. K., and Wan, Y. "Electronic and magnetic properties of Re-doped single-layer MoS_2: A DFT study". In: *Computational Materials Science* 128 (2017), pp. 287–293. DOI: 10.1016/j.commatsci.2016.11.030.

[209] Wang, D., Jiao, Y., Shi, W., Pu, B. W., Ning, F. H., Yi, J., Ren, Y., Yu, J., Li, Y. J., and Wang, H. X. "Fundamentals and advances of ligand field theory in understanding structure-electrochemical property relationship of intercalation-type electrode materials for rechargeable batteries". In: *Progress in Materials Science* 133 (2023), p. 101055. DOI: 10.1016/j.pmatsci.2022.101055.

[210] Gillespie, R. J., Popelier, P. L., Gillespie, R. J., and Popelier, P. L. a. *Chemical bonding and molecular geometry: from Lewis to electron densities*. Oxford University Press New York, 2001.

[211] Callister, W. D. and Rethwisch, D. G. *Materials science and engineering: an introduction*. Wiley New York, 1999.

[212] Bach, D., Schneider, R., Gerthsen, D., Verbeeck, J., and Sigle, W. "EELS of niobium and stoichiometric niobium-oxide phases—Part I: Plasmon and near-edges fine structure". In: *Microscopy and Microanalysis* 15.6 (2009), pp. 505–523. DOI: 10.1017/S143192760999105X.

[213] Nico, C., Monteiro, T., and Graça, M. P. F. "Niobium oxides and niobates physical properties: Review and prospects". In: *Progress in Materials Science* 80 (2016), pp. 1–37. DOI: 10.1016/j.pmatsci.2016.02.001.

[214] Hampl, M. and Schmid-Fetzer, R. "Thermodynamic description of the Ti–O system". In: *International Journal of Materials Research* 106.5 (2015), pp. 439–453. DOI: 10.3139/146.111210.

[215] Drebushchak, V. A. "Thermal expansion of solids: review on theories". In: *Journal of Thermal Analysis and Calorimetry* 142.2 (2020), pp. 1097–1113. DOI: 10.1007/s10973-020-09370-y.

[216] Wei, B., Sun, Q. Y., Li, C., and Hong, J. W. "Phonon anharmonicity: a pertinent review of recent progress and perspective". In: *Science China Physics, Mechanics & Astronomy* 64.11 (2021), p. 117001. DOI: 10.1007/s11433-021-1748-7.

[217] Hofmeister, A. M., Criss, E. M., and Criss, R. E. "Thermodynamic relationships for perfectly elastic solids undergoing steady-state heat flow". In: *Materials* 15.7 (2022), p. 2638. DOI: 10.3390/ma15072638.

[218] Trelles, J. P. "Nonequilibrium phenomena in (quasi-) thermal plasma flows". In: *Plasma Chemistry and Plasma Processing* 40.3 (2020), pp. 727–748. DOI: 10.1007/s11090-019-10046-1.

[219] Ceder, G., Garbulsky, G. D., Avis, D., and Fukuda, K. "Ground states of a ternary fcc lattice model with nearest-and next-nearest-neighbor interactions". In: *Physical Review B* 49.1 (1994), p. 1. DOI: 10.1103/PhysRevB.49.1.

[220] Tang, L. Y., Fan, J. K., Kou, H. C., Tang, B., and Li, J. S. "Effect of oxygen variation on high cycle fatigue behavior of Ti-6Al-4V titanium alloy". In: *Materials* 13.17 (2020), p. 3858. DOI: 10.3390/ma13173858.

[221] Luo, S. D., Song, T. T., Lu, S. L., Liu, B. Z., Tian, J., and Qian, M. "High oxygen-content titanium and titanium alloys made from powder". In: *Journal of Alloys and Compounds* 836 (2020), p. 155526. DOI: 10.1016/j.jallcom.2020.155526.

[222] Wang, H. L., Lai, D. K. Z., Song, C. H., Zhao, Y. L., Cheng, J., Bönisch, M., and Sun, Z. Z. "Zero thermal expansion and high Young's modulus in Ti-Nb achieved by concurrent α'' iso and ω precipitation". In: *Scripta Materialia* 232 (2023), p. 115477. DOI: 10.1016/j.scriptamat.2023.115477.

[223] Alam, A., Chouhan, R. K., and Mookerjee, A. "Phonon modes and vibrational entropy of disordered alloys with short-range order: A first-principles calculation". In: *Physical Review B* 83.5 (2011), p. 054201. DOI: 10.1103/PhysRevB.83.054201.

[224] Chen, R. Q., Ma, G. B., and Guo, H. "Six-dimensional quantum calculations of highly excited vibrational energy levels of hydrogen peroxide and its deuterated isotopomers". In: *The Journal of Chemical Physics* 114.11 (2001), pp. 4763–4774. DOI: 10.1063/1.1348274.

[225] Conte, R., Aieta, C., Botti, G., Cazzaniga, M., Gandolfi, M., Lanzi, C., Mandelli, G., Moscato, D., and Ceotto, M. "Anharmonicity and quantum nuclear effects in theoretical vibrational spectroscopy: a molecular tale of two cities". In: *Theoretical Chemistry Accounts* 142.5 (2023), p. 53. DOI: 10.1007/s00214-023-02993-y.